Structural, Magnetic and Electronic Properties of Surface alloys and Interfaces: A First Principles Study

A Thesis

Submitted For the Degree of

DOCTOR OF PHILOSOPHY

in the Faculty of Science

by

Madhura Marathe

THEORETICAL SCIENCES UNIT
JAWAHARLAL NEHRU CENTRE FOR ADVANCED SCIENTIFIC RESEARCH
Bangalore – 560 064

JULY 2013

To my father

DECLARATION

I hereby declare that the matter embodied in the thesis entitled "**Structural, Magnetic and Electronic Properties of Surface alloys and Interfaces: A First Principles Study**" is the result of investigations carried out by me at the Theoretical Sciences Unit, Jawaharlal Nehru Centre for Advanced Scientific Research, Bangalore, India under the supervision of Prof. Shobhana Narasimhan and that it has not been submitted elsewhere for the award of any degree or diploma.

In keeping with the general practice in reporting scientific observations, due acknowledgement has been made whenever the work described is based on the findings of other investigators.

Madhura Marathe

CERTIFICATE

I hereby certify that the matter embodied in this thesis entitled "**Structural, Magnetic and Electronic Properties of Surface alloys and Interfaces: A First Principles Study**" has been carried out by Ms. Madhura Marathe at the Theoretical Sciences Unit, Jawaharlal Nehru Centre for Advanced Scientific Research, Bangalore, India under my supervision and that it has not been submitted elsewhere for the award of any degree or diploma.

Prof. Shobhana Narasimhan
(Research Supervisor)

Acknowledgment

I would first like to thank my Ph. D. advisor Prof. Shobhana Narasimhan for all her academic and non-academic help. She not only suggested me various problems I have worked on, and but also discussed about how to tackle each problem from different angles. She extensively worked with me on my presentation and writing skills which were almost non-existent before. I should also mention all the cakes, cookies and books which I was able to enjoy because of her.

I would like to thank my experimental collaborators Sylvie Rousset, Vincent Repain, Yann Girard, Jérôme Lagoute, and Shruti Mehendale at Laboratoire Matériaux et Phénomènes Quantiques, Université Paris Diderot-Paris 7, Paris. It was really a good experience to discuss with them as it gave an insight from actual experimental point of view. I would also like to thank my another collaborator Alejandro Diaz-Ortiz at Max-Planck Institute for Metal Research for teaching me the cluster expansion method, and allowing me to use his code. I would like to thank Prof. M. S. Narasimhan and Dr. Satyavani Vemparala for many fruitful discussions.

I would also like to thank Prof. Umesh Waghmare, Prof. Srikanth Sastry, Prof. Swapan Pati, Prof. Chandan Dasgupta, Prof. G. U. Kulkarni, Dr. N. S. Vidyadhiraja, Dr. Subir Das, and Prof. S. Ranganathan for all the things they have taught me through their courses. I would also like to thank all my school and college teachers, and a special thanks to Prof. Kanhere and Dr. Dey from Pune university.

I would like to thank all present and past labmates – Prasenjit, Jaita, Mighfar, Brandon, Nisha, Debosruti, Kanchan, Sananda, Lakshmi, Vasudevan, and Bulumoni. I also thank all my friends and colleagues whose names are not mentioned here.

I would like to acknowledge funding from the Indo-French grant from CEFIPRA which made it possible for me to work with Sylvie and others in Paris.

I would like to acknowledge the computational facilities at CCMS, JNCASR and Ershaad, Amit, and Bharati for the technical support. I would

also like to acknowledge the computational facilities at the Texas Advanced Computing center of the university of Texas at Austin.

I would like to thank all the administrative and academic staff at JNCASR especially Mr. Jayachandra, Dr. Princy and Mrs. Sukanya, and also Chandrayyah canteen and hostel mess staff.

Last but not the least, I would like to thank my family and Kshitij for their support and patience.

List of Publications

Included in thesis

1. "Study of formation of thin film alloys of Fe-Au on Mo(110) surface: a DFT + cluster expansion study", M. Marathe, S. Narasimhan and A. Diaz-Ortiz, submitted.

2. "Spin-polarized Surface States on Fe-deposited Au(111) surface: a theoretical study", M. Marathe, J. Lagoute, V. Repain, S. Rousset and S. Narasimhan, Surf. Sci. **606**, 950 (2012).

3. "Prediction of Reconstruction in Heteroepitaxial Systems using the Frenkel-Kontorova Model", S. Mehendale, M. Marathe, Y. Girard, V. Repain, C. Chacon, J. Lagoute, S. Rousset and S. Narasimhan, Phys. Rev. B **84**, 195458 (2011).

4. "Electronic properties of Fe clusters on a Au(111) surface", A. Delga, J. Lagoute, V. Repain, C. Chacon, Y. Girard, M. Marathe, S. Narasimhan and S. Rousset, Phys. Rev. B **84**, 035416 (2011).

5. "Ordered Surface Alloy of Bulk-immiscible Components Stabilized by Magnetism", S. Mehendale, Y. Girard, V. Repain, C. Chacon, J. Lagoute, S. Rousset, M. Marathe and S. Narasimhan, Phys. Rev. Lett. **105**, 056101 (2010).

6. "Mixing and Magnetic Properties of Surface Alloys: The Role of the Substrate", M. Marathe, M. Imam and S. Narasimhan, Appl. Surf. Sci. **256**, 449 (2009).

7. "Elastic and Chemical Contributions to the Stability of Magnetic Surface alloys on Ru(0001)", M. Marathe, M. Imam and S. Narasimhan, Phys. Rev. B **79**, 085413 (2009).

Not included in thesis

- "Electronic properties of thiophene molecules on Fe/Au(111)", M. Marathe and S. Narasimhan, manuscript in preparation.
- "*Ab initio* study of formation of $Ni_xN_{(1-x)}$ surface alloys on Ru(0001)", M. Marathe and S. Narasimhan, manuscript in preparation.
- "Ni_xPt_{1-x}/Rh(111): A Stable Surface Alloy with Enhanced Magnetic Moments", M. Imam, M. Marathe and S. Narasimhan, Solid State Comm. **149**, 559 (2009).
- "Competition between Elastic and Chemical Effects in the Intermixing of Co and Ag on Rh(111)", M. Imam, M. Marathe and S. Narasimhan, J. Chem. Sci. **120**, 621 (2008).
- "$Si_xC_{1-x}O_2$ Alloys: A possible route to stabilize carbon-based silica-like solids?", A. Aravindh, *et al.*, Solid State Comm. **144**, 273 (2007).

List of Abbreviations

E_f	Fermi energy
M	"Magnetic" element
N	"Non-magnetic" element
μ_B	Bohr Magneton
m_e	Mass of a free electron
1D	One-dimensional
2D	Two-dimensional
AFM	Antiferromagnetic
bcc	Body Centered Cubic
BZ	Brillouin Zone
CE	Cluster expansion
CN	Coordination Number
CV	Cross validation
DFT	Density Functional Theory
DM	Deposited Monolayers
DOS	Density of States

ECI Effective cluster interactions

ECN Effective Coordination Number

eV electron volt

fcc Face Centered Cubic

FK Frenkel-Kontorova

FM Ferromagnetic

FSM Free-standing Monolayers

GGA Generalized Gradient Approximation

GS Ground state

hcp Hexagonal Closed Packed

HF Hellmann-Feynman

HK Hohenberg-Kohn

IBZ Irreducible Brillouin Zone

KS Kohn-Sham

LDA Local Density Approximation

LDOS Local Density of States

LEED Low-energy electron Diffraction

LRO Long-range order

meV milli-electron volt

ML Monolayer

NN Nearest-Neighbor

NSP Non-spin Polarized

PDOS Projected Density of States

PP Pseudopotentials

QE Quantum-ESPRESSO

QMD Quenched Molecular Dynamics

QM Quantum mechanical

RKKY Ruderman-Kittel-Kasuya-Yoshida

Ry Rydberg

SBZ Surface Brillouin Zone

SP Spin Polarized

STM Scanning Tunneling Microscope

STS Scanning Tunneling Spectroscope

XC Exchange-Correlation

List of Figures

List of Tables

Contents

Chapter 1

Introduction

The broad aim of this thesis is to study different classes of two-dimensional (2D) materials using first-principles methods. Surfaces and 2D systems are interesting for a large number of reasons. Atoms at the surface have reduced coordination with respect to the bulk, which is responsible for several unusual phenomena observed only at the surface. Some of these include structural relaxations and/or reconstructions, mixing of bulk-immiscible metals, enhanced chemical reactivity, high magnetic anisotropy and exotic magnetic phases such as spin spirals. In this work, I have mainly focused on metallic surface alloys and interfaces, with a common theme being magnetic materials. We would like to understand various interactions which are dominant at surfaces and interfaces, and how the interplay between them can lead to interesting structural, magnetic and electronic properties. Some of the interactions which are dealt with include elastic, chemical, and magnetic interactions. This study has allowed us not only to gain insight into the relative importance of these interactions, but also to use our understanding to

formulate design principles. Using these principles as a guideline, we have, e.g., designed a novel surface alloy. In most of my projects, I have worked alongside an experimental group, and have seen a great synergy between my theoretical studies and experimental investigations.

I have primarily used density functional theory (DFT) calculations for my studies. Using DFT, one can calculate the total energy of the system, which can be used to determine the stability of various phases, and to calculate quantities such as the formation energy and the adsorption energy. Also we can obtain (approximate) wavefunctions and (exact) charge densities which can be used to determine quantities such as charge transfer and hybridization. However, DFT calculations become computationally very expensive as the number of atoms in the system increases, and hence such calculations are restricted to system sizes of the order of a few hundreds of atoms. Therefore, in addition, I have also used the cluster expansion (CE) technique, which is an Ising-like lattice model and uses the configurational dependence of various physical quantities. One can calculate model parameters by fitting to the data from DFT, and then use the calculated CE Hamiltonian for larger unit cells, or even to get high temperature properties. We have also used a model, known as the Frenkel-Kontorova (FK) model, to study surface reconstructions. The combination of such different techniques has proved essential in our study to probe diverse phenomena occurring at the surface. In Chapter 2, I have discussed the theoretical background – density functional theory and the cluster expansion technique – while the FK model has been discussed in Chapter 6.

When a surface is created, periodicity along one direction of the crystal

is broken, and atoms at the surface will have reduced coordination than in the bulk. This gives rise to various phenomena such as relaxation or reconstruction of the surface layer, enhanced magnetic moments, and surfaces states in the electronic band structure. In our study, we have considered an interface between two different metals such that one metal is deposited on another metal to form a thin film. These type of systems are known as heteroepitaxial systems. In heteroepitaxial systems, the metal surface used for deposition is called the substrate, and can either be considered as merely providing a periodic potential for the growth, or as actively interacting with the deposited metal. The surface structure is primarily determined by two quantities – the surface energy (the energy required to create the surface) and the surface stress (stress arising from the reduced coordination). The reduction of the surface stress can occur in many ways such as surface reconstruction, dislocation formation, and alloying.

It has been known for a long time that alloying between two metals can lead to enhanced properties. However, not all pairs of metals form alloys in their bulk phases – the main restriction comes from elastic strain due to atomic-size mismatch (the first Hume-Rothery rule). In recent years, it has been shown that some pairs of metals which do not form alloys in the bulk can mix at the surface; these alloys are called "surface alloys". The formation of bimetallic alloys at the surface is interesting for many applications such as catalysis [1], magnetic storage [2], and fuel cell technology [3]. In the first part of the thesis, we have studied surface alloy systems in which a pair of metals – with one magnetic and one non-magnetic constituent – is deposited on the surface of a third metal. We have shown a schematic diagram of this

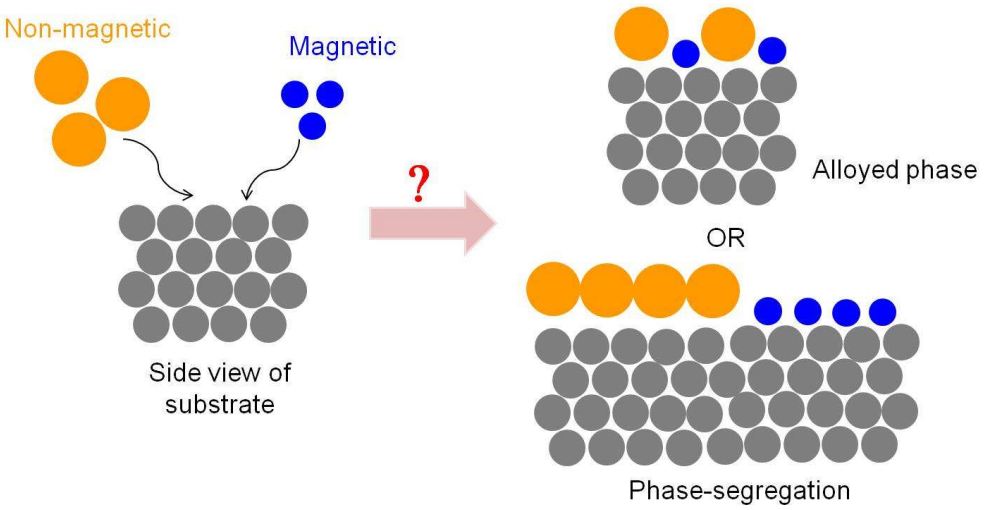

Figure 1.1: *Schematic diagram introducing a main theme for the surface alloy work: if two metals (orange and blue spheres) are deposited on a substrate (gray spheres), then there are primarily two possibilities – mixing of the two overlayer metals, or a phase-segregated form. In the first part of the thesis (Chapters 3 – 5), we have looked at such systems and have studied which of these two possibilities is energetically more favored, which interactions are dominant, and whether there are any trends which will help to predict the properties of these types of systems.*

phenomenon in Fig. 1.1. For these types of systems, we are interested in the structure of the overlayer, and whether the two constituents will prefer to mix at the surface, or would instead phase-segregate. The next three chapters of this thesis (Chapters 3 – 5) deal with surface alloy systems.

In Chapter 3, we have studied the structural and magnetic properties of surface alloys of the type $M_xN_{(1-x)}$/Ru(0001), where M is a magnetic metal (Fe or Co), and N is a non-magnetic metal (Pt, Ag, Au, Cd, or Pb). Most of these pairs of metals are immiscible in their bulk phases, and we would like to know whether they mix on the surface; if yes, then which interactions are responsible for mixing, and whether there are rules or trends which can be explored for the further investigation of similar systems. We have separated

out elastic and chemical interactions to study the relative importance of each, because hitherto it was believed that the reduction of elastic stress is primarily responsible for mixing at the surface. We have also examined how magnetic interactions affect overall stability. Based on our analysis, we have suggested promising candidate alloy systems for further experimental investigation.

In Chapter 4, we have studied, in detail, one of our "predicted" surface alloy systems – Fe-Au/Ru(0001) – which was investigated by our experimental collaborators – the group of Prof. S. Rousset. Their experiments show that there is indeed an atomic-level mixing for this system, as predicted by our calculations; it was also observed that Au-rich phases show long-range order having a $\sqrt{3} \times \sqrt{3}$ surface unit cell, but Fe-rich phases show only short range order. The main aim of this chapter is to understand these experimental findings. In the previous chapter, we have considered a large number of systems, but only a few configurations; in contrast, in this chapter we study many configurations for one particular system. This approach allows us to compare our results with experiments over a large concentration range. and to explain the dissimilar trends observed in experiments for Fe-rich and Au-rich phases.

In Chapter 5, we have considered the effect of changing the substrate for a Fe-Au overlayer, by replacing the Ru(0001) substrate by a Mo(110) substrate. The Mo(110) surface is anisotropic, which might affect elastic interactions in the Fe-Au overlayer. In some experiments, it has been observed that there is atomic-level mixing for Fe-Au nanostructures on Mo(110), but no long-range order. Our aim is to understand why there is no long range order for

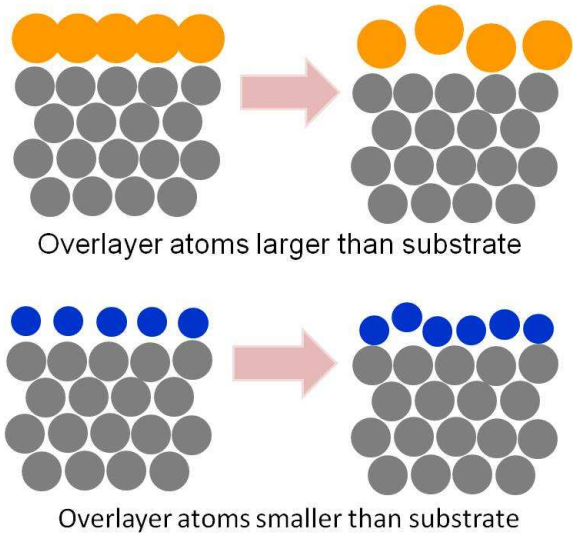

Figure 1.2: *Schematic diagram introducing surface reconstruction: for heteroepitaxial systems, the surface stress can either be compressive or tensile leading to different types of surface reconstructions. These reconstructed systems typically have large unit cells, and cannot be handled by DFT calculations.*

this system. For this study, we have combined two techniques: DFT and CE. This allows us to search for the ground states in large systems (we have considered up to 20 atoms per surface unit cell).

In the next part of the thesis, we will again work with heteroepitaxial systems, but only considering single-component overlayers. For the surface alloy work, we have assumed that both the alloy and the phase-segregated single-component overlayers are pseudomorphic with the substrate. It is essential to examine whether this is a valid assumption. For the mixed alloy pseudomorphic systems, where the mixing has lowered the surface stress, and hence the tendency towards reconstruction, this is probably a good approximation. However, for single-component pseudomorphic monolayers on a Ru(0001) substrate, the surface stress can be large enough to trigger reconstruction. Thus we have studied this possibility for the single-component layers on a

substrate, as shown in Fig. 1.2. The study of surface reconstruction itself is often a great challenge because of the large unit cells of the reconstructed surfaces, and various competing interactions present at the surface. The controlling of surface reconstruction has potential applications in self-assembled nanostructures [4] and molecular assemblies [5]. Here we have studied an interface for possible reconstruction; we have assumed that the role of the substrate is restricted to providing an external periodic potential, and that structural changes mainly occur in the deposited overlayer.

In Chapter 6, we have studied the possibility of reconstruction for heteroepitaxial systems of the type O/Ru(0001), where O is an overlayer species, using the Frenkel-Kontorova model. The reconstructed surfaces may have very large unit cells and thus a complete DFT study is not feasible for these. The FK model is a simple classical model which takes into account the different competing interactions at the surface, i.e., the cost of compressing or stretching intralayer bonds in the overlayer, the cost of losing registry with the substrate, and the cost of obtaining additional atoms from a reservoir or dumping them into a sink. We have used two approaches – a mapping to the one-dimensional (1D) FK model, which we have extended to the case of heteroepitaxial systems, and a complete numerical solution of the 2D FK model using quenched molecular dynamics, which allows us to validate our extension of the 1D model. The latter approach also provides additional information such as the period of the reconstruction. We compare the two approaches with each other and to experimental results, when these are available. We have also examined the possibility of tuning the periodicity of reconstruction, which is useful for applications where the reconstruction is used as a

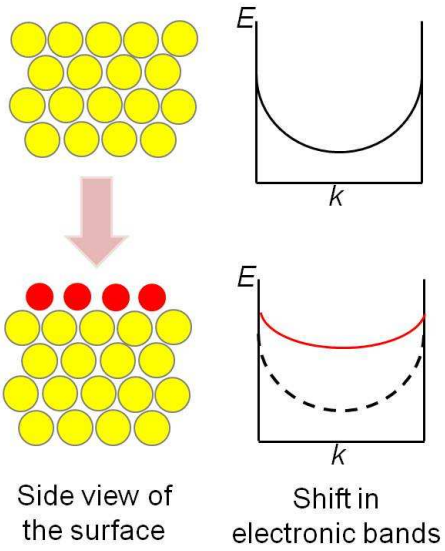

Figure 1.3: *Schematic diagram showing a change in the electronic band structure at the interface: in the top panel, we have shown the side view of a substrate (yellow spheres) along with an electronic band dispersion, that is, energy E as a function of wave vector* $\mathbf{k}$*. In the bottom panel, a thin film of another metal (red spheres) has been deposited on the substrate, and as a result the band structure of the clean substrate (dashed line) is altered to a new value shown by the red curve.*

template for the growth of self-organized nanostructures.

Next, we have studied in great detail how the interface will affect the electronic properties of the substrate. The schematic diagram corresponding to this is shown in Fig. 1.3. In Chapter 7, we have studied the electronic properties of Fe/Au(111), mainly concentrating on the effect of Fe deposition on the Shockley surface state on the Au(111) surface. We have calculated the band structure, focusing primarily on the surface state dispersion, and analyzed the nature and origin of these states using the projected density of states and charge density analysis. We have compared our results with the experimental data. We have also considered the effect of different stacking possibilities on the electronic properties.

Finally in the last Chapter, we have summarized the main findings and conclusions of this thesis.

There are also four appendices describing – (A) derivation of the formula for surface stress (used in Chapter 3); (B) discussion of the formula to generate distinct structures (used in Chapters 4 and 5); (C) list of configurations used for Fe-Au/Ru(0001); and (D) list of configurations used for the DFT study of Fe-Au/Mo(110).

Chapter 2

Methodological Background

2.1 Introduction

In this chapter, I will discuss the theoretical framework which I have used to study the properties of materials in my thesis. I have mainly used standard density functional theory (DFT), which allows us to calculate the ground state properties at zero temperature. I have also used the cluster expansion method, which combines statistical mechanics with quantum mechanical methods such as DFT; this allows us to go beyond some of the known limitations of DFT. A brief discussion of both these methods follows.

2.2 Density Functional Theory

In quantum mechanics, the complete information about any system can be obtained by solving the non-relativistic Schrödinger equation. For any material, the Hamiltonian is given by:

$$\hat{H} = -\frac{\hbar^2}{2m_e}\sum_i \nabla_i^2 - \sum_I \frac{\hbar^2}{2M_I}\nabla_I^2 + \sum_{i,I}\frac{Z_I e^2}{|\mathbf{r}_i - \mathbf{R}_I|} + \frac{1}{2}\sum_{i\neq j}\frac{e^2}{|\mathbf{r}_i - \mathbf{r}_j|} + \frac{1}{2}\sum_{I\neq J}\frac{Z_I Z_J e^2}{|\mathbf{R}_I - \mathbf{R}_J|}, \tag{2.1}$$

where m_e and e denote the mass and charge of a free electron respectively; M_I and Z_I denote the mass and the charge of a nucleus I respectively; $\mathbf{r}_i$ and $\mathbf{R}_I$ denote the position of the i^{th} electron and I^{th} nucleus respectively; and $\hbar$ is the Planck's constant divided by 2π. The sums are taken over the total number of electrons and/or ions in the system. In this equation, the first two terms give the kinetic energy of electrons and ions respectively, and the last three terms include Coulomb interactions between electrons and nuclei, electrons and electrons, and nuclei and nuclei respectively. Then, by using the Born-Oppenheiemer approximation [6], one can separate electronic and nuclear degrees of freedom. There is no analytical solution for this equation, and even numerical solutions are restricted by the computational cost required.

The density functional theory (DFT) maps such a many-body interacting system onto an effective one-body system with the electronic density as the basic variable, rather than the many-body wavefunction. The DFT formalism

has arisen from the Hohenberg-Kohn theorems and the subsequent Kohn-Sham equations, which we have briefly described below.

2.2.1 Hohenberg-Kohn Theorems

The Hohenberg-Kohn (HK) theorems introduced in 1964 [7] form the basis of density functional theory. There are two theorems which are given by [8]:

- Theorem 1 – "For any system of interacting particles in an external potential $V_{ext}(\mathbf{r})$, the potential $V_{ext}(\mathbf{r})$ is determined uniquely, except for a constant, by the ground state particle density $n_0(\mathbf{r})$."

- Theorem 2 – "*A universal function* for the energy $E[n]$ in terms of the density $n(r)$ can be defined, valid for any external potential $V_{ext}(\mathbf{r})$. For any particular $V_{ext}(\mathbf{r})$, the exact ground state energy of the system is the global minimum value of this functional, and the density $n(\mathbf{r})$ that minimizes the functional is the exact ground state density $n_0(\mathbf{r})$."

2.2.2 Kohn-Sham Equations

The real applicability of the HK theorems and the wide use of DFT for many condensed matter systems was only possible after the formulation of the Kohn-Sham (KS) equations. These equations map an interacting many-body system onto non-interacting electrons which experience an effective potential due to all the other electrons. The Kohn-Sham equations are given by:

$$\left[\frac{-\hbar^2}{2m_e}\nabla_i^2 + V_{eff}(\mathbf{r})\right]\psi_i(\mathbf{r}) = \epsilon_i\psi_i(\mathbf{r}), \tag{2.2}$$

where the effective potential is:

$$V_{eff}(\mathbf{r}) = V_I(\mathbf{r}) + V_H(\mathbf{r}) + V_{xc}(\mathbf{r}). \tag{2.3}$$

Here ψ_i is the wavefunction of electronic state i, ϵ_i is the i^{th} Kohn-Sham eigenvalue, $V_I(\mathbf{r})$ is the total ionic potential, and $V_H(\mathbf{r})$ is the Hartree potential of the electrons, given by

$$V_H(\mathbf{r}) = e^2 \int \frac{n(\mathbf{r}')}{|\mathbf{r} - \mathbf{r}'|} \mathrm{d}\mathbf{r}', \tag{2.4}$$

and $V_{xc}(\mathbf{r})$ is the exchange-correlation (XC) potential given by the functional derivative:

$$V_{xc}(\mathbf{r}) = \frac{\delta E_{xc}[n(\mathbf{r})]}{\delta n(\mathbf{r})}, \tag{2.5}$$

where $E_{xc}[n(\mathbf{r})]$ is the exchange-correlation interaction between electrons. The exchange interaction results from the Pauli exclusion principle which forbids two electrons of the same spin having the same state which leads to repulsion between them, and the correlation is the effect of many-body interactions in the system. Here the charge density $n(\mathbf{r})$ is defined as:

$$n(\mathbf{r}) = \sum_i \psi_i^*(\mathbf{r})\psi_i(\mathbf{r}). \tag{2.6}$$

The wavefunctions $\psi_i(\mathbf{r})$ are orthonormal to each other. Note that here we have not explicitly considered spin degrees of freedom; the description of spin-polarized DFT is given in Section 2.2.9.

The ground state energy of the system of electrons with ions at positions $\mathbf{R}_I$ can be obtained by solving the KS equations. These equations need to be solved self-consistently, because the calculated eigenfunctions on the right hand side of Eq. (2.2) are needed to determine the charge density of the electrons, which is needed to compute the exchange-correlation and Hartree potential terms on the left hand side. A flow-chart demonstrating this self-consistent loop is shown in Fig. 2.1. Note that the Kohn-Sham energy eigenvalues and eigenfunctions are not the "actual" single-particle electron eigenenergies and eigenfunctions, but the eigenvalues and eigenfunctions of a fictitious one-particle system. Therefore, if used to calculate quantities of interest, these must be interpreted with caution.

2.2.3 Exchange-correlation Functionals

The exact form of the exchange-correlation interaction is not known, which leads to one of the main approximations required to use DFT for practical purposes. One of the simplest approximations for the exchange-correlation functional is the "local density approximation" (LDA), in which it is assumed that the XC functional depends only on the density at the position $\mathbf{r}$. In this approximation, the XC functional is given by:

$$E_{xc}^{LDA} = \int \epsilon_{xc}(\mathbf{r}) n(\mathbf{r}) \mathrm{d}\mathbf{r},$$

$$\text{where} \qquad \epsilon_{xc}(\mathbf{r}) = \epsilon_{xc}^{hom}[n(\mathbf{r})]. \tag{2.7}$$

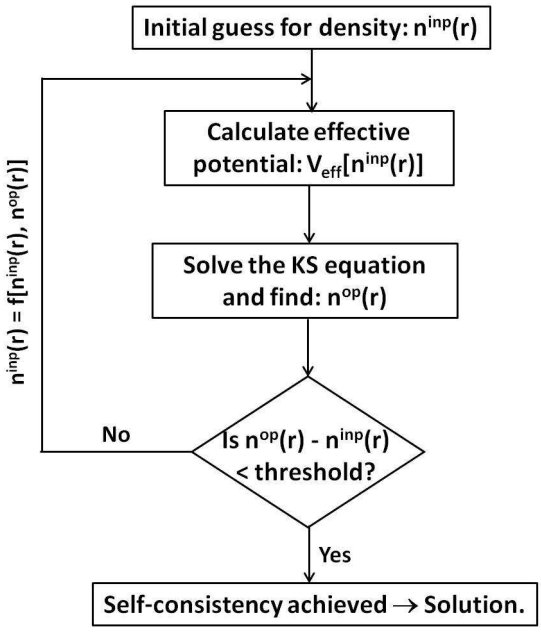

Figure 2.1: *Flow chart for self-consistent solution of the Kohn-Sham equations: One starts with an initial guess for the charge density, $n^{inp}(\mathbf{r})$. Using this charge density, the effective potential is calculated. Then solving the Kohn-Sham equations, the output charge density $n^{op}(\mathbf{r})$ is obtained. Self-consistency is achieved when the difference between the input and output charge densities is less than the predefined threshold value; if not, then a new density is constructed by a combination of the initial and new charge densities and the loop is started again.*

Here $\epsilon_{xc}^{hom}[n(\mathbf{r})]$ is the exchange-correlation energy of the homogeneous electron gas having density $n(\mathbf{r})$. This has been calculated by Ceperley and Alder [9] using quantum Monte Carlo simulations, and has been parametrized by Perdew and Zunger [10]. This approximation may seem rather drastic, and would seem to be applicable to only those systems in which the electronic density varies slowly. However it is known to work well for many systems.

One can improve the accuracy by including a term which considers gradients of the density. There is no unique way to include gradients, and several different forms for gradient corrections have been suggested – these are collectively known as "generalized gradient approximations" (GGAs). Some of

the more frequently used forms are the Perdew-Burke-Ernzerhof form [11] and the Perdew-Wang form [12]. In these approximations, the XC functional is given by:

$$E_{xc}^{GGA} = \int \epsilon_{xc}[n(\mathbf{r}), \nabla n(\mathbf{r})]n(\mathbf{r})\mathrm{d}\mathbf{r}. \tag{2.8}$$

Here ϵ_{xc} depends not only on the electronic density, but also on gradients of the density.

The LDA is known to usually overbind and hence typically results in lattice constants, for bulk materials that are too small, whereas the GGA usually corrects this effect. However, the GGA is known to often underbind, which results in larger lattice constants. Some properties such as magnetic moments, are usually better estimated using the GGA.

2.2.4 Basis Sets

To solve the KS equations, the wavefunctions ψ_i's are expanded using a suitable basis set $\{\phi_j(\mathbf{r})\}$:

$$\psi_i(\mathbf{r}) = \sum_j c_j \phi_j(\mathbf{r}). \tag{2.9}$$

Commonly used basis sets include plane wave basis sets, localized basis sets, e.g., atomic orbitals, etc. In our study, we have used a plane-wave basis set which is briefly introduced below.

The periodicity of crystal structures enables one to reduce the problem of calculation for the infinite crystal to calculation for a small unit cell which is repeated throughout space. The crystal potential satisfies the condition:

$V(\mathbf{r}) = V(\mathbf{r} + \mathbf{R})$, where $\mathbf{R}$ are the lattice vectors. Using the periodicity and Bloch's theorem, the electronic wavefunctions can be written as a sum of plane waves:

$$\psi_{i,\mathbf{k}}(\mathbf{r}) = \sum_{\mathbf{G}} c_{i,\mathbf{k}+\mathbf{G}} e^{i(\mathbf{k}+\mathbf{G}).\mathbf{r}}, \tag{2.10}$$

where $\mathbf{G}$ are the reciprocal lattice vectors, and $\mathbf{k}$ are the wavevectors. To get an exact expansion, an infinite number of plane waves $e^{i(\mathbf{k}+\mathbf{G}).\mathbf{r}}$ are necessary in the expansion. However, the truncation of basis set is possible, because usually plane waves having smaller kinetic energy $\frac{\hbar^2}{2m}|\mathbf{k}+\mathbf{G}|^2$ contribute more than the those with larger kinetic energy values. Therefore, one can define a kinetic energy cut-off $E_{cut} = \frac{\hbar^2}{2m}|\mathbf{k}+\mathbf{G}|^2_{cut}$ such that all the plane waves having kinetic energy below this cut-off value, are included in the expansion, that is, for a given $\mathbf{k}$, all the plane waves up to length $|\mathbf{k}+\mathbf{G}|_{cut}$ are included. The error in total energy arising from the truncation can be reduced by increasing cut-off energy.

2.2.5 Pseudopotential Approximation

This is another approximation that is sometimes used to reduce the computational cost; it is usually used when a plane wave basis is employed. This uses the well-known fact that many of the physical and chemical properties are primarily dependent on the valence electrons, and less (or not) affected by the core electrons. Recall that the core electrons are tightly bound, that is, highly localized in nature, and the wavefunctions of valence electrons have many oscillations in the core region. These two facts together would necessitate a large plane-wave basis set to perform all-electron calculations. In

the pseudopotential (PP) approximation [13,14], these problems are circumvented by replacing the strong ionic potential by a weaker "pseudo" potential which acts on "pseudo" wavefunctions of only the valence electrons. Effectively the core electrons are removed, and their effect is accounted in the "pseudo" potential of the ions. Also the oscillations of valence electrons in the core region are removed; however it is ensured that the "pseudo" wavefunctions match with the "actual" valence wavefunctions beyond a certain distance from the nucleus, known as the cut-off radius. A good PP should have smoothness and transferability properties. The transferability of the PP implies that the same PP could be used in several different chemical and structural environments. The use of the PP drastically reduces the required E_{cut} for the plane wave basis.

In addition, if the PP is constructed such that the integrated charge densities, i.e., the integral of the squared amplitudes of wavefunctions, of the real and pseudo wavefunctions are identical in both the core and the valence regions, then it is known as a norm-conserving PP [15–17]. When the norm-conserving criterion is relaxed, that is, the charge densities of the real and pseudo wavefunctions are not identical, then a much softer PP (i.e., requiring a much lower E_{cut}) can be constructed. This is done, e.g., in ultrasoft pseudopotentials [18] which further reduce the computational time by using an even smoother core region. However, this reduces the charge density in the core region from its actual value; and hence it is required to take an extra care to ensure that this does not result in significant errors. In this thesis, we have used the ultrasoft pseudopotentials for all the studied systems.

2.2.6 k-point Sampling and Smearing Technique

Various physical quantities, such as the total energy and the density of states, are calculated by integrating over all the wavevectors in the first Brillouin zone (BZ). However there is an infinite number of wavevectors in the BZ, which will lead to infinite computational time. Therefore, for practical calculations, the summation is performed over a finite number of k-points instead of integration; e.g., in computing the density $n(\mathbf{r})$, the approximation is as follows -

$$n(\mathbf{r}) = \frac{V}{(2\pi)^3} \int n_k(\mathbf{r}) \mathrm{d}\mathbf{k} \approx \sum_{\{\mathbf{k}\} \in IBZ} n_k(\mathbf{r}) \omega_{\mathbf{k}}, \tag{2.11}$$

where V is the unit cell volume, and $\omega_{\mathbf{k}}$ is the weight associated with each k-point, and

$$n_{\mathbf{k}}(\mathbf{r}) = \sum_i \psi^*_{i,\mathbf{k}}(\mathbf{r}) \psi_{i,\mathbf{k}}(\mathbf{r}). \tag{2.12}$$

Here $\mathbf{k}$ indicates discrete k-points in the irreducible Brillouin zone (IBZ), and the sum is taken over occupied states i. There are various ways to select the k-points in the BZ to do these sums, such as taking a uniform k-mesh, as suggested by Monkhorst and Pack [19], or special points, such as suggested Chadi and Cohen [20]. The discretization of k-points would lead to small errors in the calculation, however one can reduce the errors by considering a larger number of k-points.

For metallic systems, one does not sum over entire bands, but only up to the Fermi level. For any band i, the total occupation is the weighted sum

over the IBZ of occupancies $f_i(\mathbf{k})$ at each k-point, and is given by:

$$\bar{f}_i = \sum_{\{\mathbf{k}\} \in IBZ} \omega_{\mathbf{k}} f_i(\mathbf{k}) \theta_i(E_i(\mathbf{k}) - E_f), \tag{2.13}$$

where $\theta_i(E_i(\mathbf{k} - E_f)$ is the step function which ensures that the occupation is one (zero) for the levels lying below (above) the Fermi level E_f. However, such a sharp step function requires a very fine sampling in reciprocal space (i.e., a large number of k-points) to be resolved adequately. Since this is expensive, one can carry out "smearing", where the sharp step function is instead replaced by a smooth function $F_i(E_i(\mathbf{k}))$ so that the total occupation is written as:

$$\bar{f}_i = \sum_{\{\mathbf{k}\} \in IBZ} \omega_{\mathbf{k}} f_i(\mathbf{k}) F_i(E_i(\mathbf{k})), \tag{2.14}$$

which allows for partial occupation around E_f. The smearing allows us to use fewer k-points than otherwise required to correctly account for a sharp discontinuity at E_f, and also corrects the convergence problems arising from level crossings.

Unlike semiconductors and insulators, metals do not have a band gap near the Fermi level, and some bands may only be partially occupied. Therefore, one can neglect the unoccupied high energy states in semiconductors and insulators, but these levels need to be considered for metallic systems. As number of bands included in the calculation increases, the computational cost also increases.

There are several ways in which smearing can be applied such as Gaussian smearing [21], Methfessel-Paxton smearing [22] and Marzari-Vanderbilt

smearing [23]. In this thesis, we have used Methfessel-Paxton smearing.

2.2.7 Force calculation: Hellmann-Feynman Theorem

To calculate the optimized geometries of systems such as surfaces, molecules, etc., one needs to calculate and minimize the forces on each atom in the system. We have used the Hellmann-Feynman (HF) theorem [24] to calculate the forces. The force on ion I is equal to the negative of the derivative of the total energy with respect the ionic position $\mathbf{R}_I$, and is calculated using:

$$\begin{aligned}
F_I &= -\frac{\partial \langle E(\mathbf{R}_I)\rangle}{\partial \mathbf{R}_I} \\
&= -\frac{\partial}{\partial \mathbf{R}_I}\Big\langle \psi(\mathbf{R})|H|\psi(\mathbf{R})\Big\rangle \\
&= -\Big\langle \frac{\partial\psi}{\partial \mathbf{R}_I}|H|\psi\Big\rangle - \Big\langle \psi|\frac{\partial H}{\partial \mathbf{R}_I}|\psi\Big\rangle - \Big\langle \psi|H|\frac{\partial\psi}{\partial \mathbf{R}_I}\Big\rangle \\
&= -\Big\langle \psi|\frac{\partial H}{\partial \mathbf{R}_I}|\psi\Big\rangle - E\left[\langle \frac{\partial\psi}{\partial \mathbf{R}_I}|\psi\rangle - \langle\psi|\frac{\partial\psi}{\partial \mathbf{R}_I}\rangle\right] \\
&= -\Big\langle \psi|\frac{\partial H}{\partial \mathbf{R}_I}|\psi\Big\rangle - E\left[\frac{\partial}{\partial \mathbf{R}_I}\langle\psi|\psi\rangle\right] \\
&= -\Big\langle \psi|\frac{\partial H}{\partial \mathbf{R}_I}|\psi\Big\rangle, \qquad \text{since } \langle\psi|\psi\rangle = 1.
\end{aligned} \tag{2.15}$$

Here $\psi(\mathbf{R})$ is the electronic eigenfunction of Hamiltonian H. The HF theorem is advantageous because it says that the force can be computed from a DFT calculation at one configuration alone, rather than from having to compute the total energy at a set of configurations and then computing derivative.

The HF theorem is based on the assumption that the basis set is complete. In actual calculations, the basis set is usually truncated, which leads to an

additional force called the Pulay force [25, 26]. This problem is not present when the basis set is position-independent, such as the plane wave basis set. This is one of the major advantages of using this basis set. We have obtained optimized geometries of the surface by minimizing forces on the surface atoms.

2.2.8 Stress Calculation

The stress tensor $\sigma_{\alpha\beta}$ is defined as the derivative of the total energy E_{tot} with respect to the strain tensor $\epsilon_{\alpha\beta}$:

$$\sigma_{\alpha\beta} = -\frac{1}{V}\frac{\partial E_{tot}}{\partial \epsilon_{\alpha\beta}}, \tag{2.16}$$

where α and β are Cartesian indices. using the HF theorem, Nielsen and Martin [27] showed that the stress can be written as:

$$\sigma_{\alpha\beta} = -\frac{1}{V}\left\langle \psi|\frac{\partial H}{\partial \epsilon_{\alpha\beta}}|\psi \right\rangle. \tag{2.17}$$

Similar to the force calculations, the truncated basis set can lead to errors in the calculated stress values. Therefore the stress calculations usually require a higher energy cut-off E_{cut} for plane waves than that would be required for total energy convergence to reduce errors.

2.2.9 Spin Polarized DFT

Till now I have described the DFT formalism which does not include a dependence of the energy on electron spin. To study magnetic systems, it is

necessary to consider spin polarized charge densities. One can define charge densities for spin up and spin down electrons using -

$$n^{\uparrow}(\mathbf{r}) = \sum_i |\psi_i^{\uparrow}(\mathbf{r})|^2 \qquad \text{and} \tag{2.18}$$

$$n^{\downarrow}(\mathbf{r}) = \sum_i |\psi_i^{\downarrow}(\mathbf{r})|^2. \tag{2.19}$$

Here $\psi_i^{\uparrow}(\mathbf{r})$ and $\psi_i^{\downarrow}(\mathbf{r})$ are the wavefunctions for spin up and down electrons respectively. The total electronic density is then given by $n(\mathbf{r}) = n^{\uparrow}(\mathbf{r}) + n^{\downarrow}(\mathbf{r})$, and the magnetization is given by $m(\mathbf{r}) = n^{\uparrow}(\mathbf{r}) - n^{\downarrow}(\mathbf{r})$. Now the KS equations can be written in terms of the spin polarized charge density and the magnetization, as follows:

$$\left[\frac{-\hbar^2}{2m_e}\nabla_i^2 + V_{eff}^{\uparrow\downarrow}(\mathbf{r})\right]\psi_i^{\uparrow\downarrow}(\mathbf{r}) = \epsilon_i^{\uparrow\downarrow}\psi_i^{\uparrow\downarrow}(\mathbf{r}), \tag{2.20}$$

where the effective potential is given by:

$$V_{eff}(\mathbf{r}) = V_I(\mathbf{r}) + V_H(\mathbf{r}) + V_{xc}^{\uparrow\downarrow}(\mathbf{r}). \tag{2.21}$$

Here, only the XC potential depends on the electron spin and is given by:

$$V_{xc}(\mathbf{r}) = \frac{\delta E_{xc}[n(\mathbf{r}), m(\mathbf{r})]}{\delta n(\mathbf{r})}. \tag{2.22}$$

These equations can be solved in a similar fashion to the non spin-polarized DFT with approximations for the XC functional.

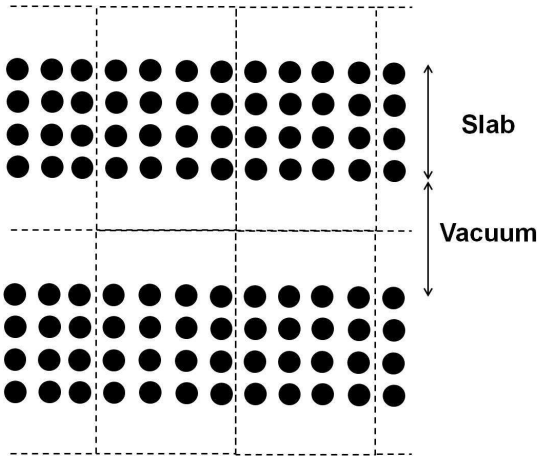

Figure 2.2: *Schematic representation of a supercell to model a surface: the supercell shown with dashed lines, is repeated in three directions to create artificial periodicity.*

2.2.10 Modeling Aperiodic Systems

In this thesis, we have studied surfaces which are not periodic in the direction perpendicular to the surface. One cannot apply Bloch's theorem to aperiodic systems, and would then need a continuous plane wave basis set instead of a discrete basis set. To model such systems within periodic boundary conditions, an "artificial" supercell is constructed. For example, to study surfaces, the surface is modeled by a crystal slab containing a number of atomic layers separated by a vacuum region (see Fig. 2.2), and the supercell is repeated in all three directions. In the supercell approach, it is extremely important that there is no spurious interaction between periodic images which will affect the properties of the system under study. One therefore has to test for convergence with respect to the size of the supercell.

2.2.11 Post-processing Techniques Used

Apart from calculating the total energies, we can use eigenvalues and eigenfunctions to calculate several other quantities such as the projected density of states (PDOS), charge densities, and simulated scanning tunneling microscopy (STM) images. The projected density of states is the projection of the eigenfunctions of the system onto atomic orbitals to get local properties such as atomic magnetic moments. The spin polarized projected density of states for the l, m^{th} orbital of the n^{th} atom is calculated as:

$$\rho_{l,m}^{(n)\uparrow\downarrow}(E) = \sum_i |\langle \phi_{l,m}^{(n)} | \psi_i^{\uparrow\downarrow} \rangle|^2 \delta(E - \epsilon_i^{\uparrow\downarrow}), \tag{2.23}$$

where $\phi_{l,m}^{(n)}$ are the atomic orbitals for the n^{th} atom, and $\psi_i^{\uparrow\downarrow}$ and $\epsilon_i^{\uparrow\downarrow}$ are the Kohn-Sham wavefunctions and eigenvalues for spin up and down, respectively, for the i^{th} state. These can be then integrated to yield atomic moments. The projected moment on the n^{th} atom is given by:

$$M_n = \sum_{l,m} \int_0^{E_f} [\rho_{l,m}^{(n)\uparrow}(E) - \rho_{l,m}^{(n)\downarrow}(E)] \mathrm{d}E. \tag{2.24}$$

The simulated STM images are obtained by calculating the local density of states at the Fermi level, which is based on the theory of tunneling between the surface and a model tip, given by Tersoff and Hamann [28]. We can directly compare the simulated images with the experimental STM images.

2.2.12 Implementation of DFT

In this thesis, we have used the PWscf code implemented in the Quantum-ESPRESSO package [29] to perform DFT calculations. It is an open source code using a plane wave basis and pseudopotentials.

2.3 Cluster Expansion Method

2.3.1 Introduction

For first principles calculations, as the system size increases, the computational expense involved increases rapidly. For example, for substitutional binary alloys with N lattice sites, there are 2^N different configurations possible. Thus, even for $N \sim 20$, the number of possibilities becomes more than a million. Thus, the ground state (GS) search for such systems using a purely quantum mechanical (QM) approach becomes a formidable task. Also, as most density functional theory (DFT) calculations are done using periodic boundary conditions, studying disordered configurations is not feasible. There are a few approaches which are used to overcome this shortcoming, such as the use of simplified electronic Hamiltonians, e.g., tight binding model [30, 31], effective pair potentials [32, 33], etc., or guessing several possible structures either by prior experience or experimental observations, and then using QM tools for calculating alloy stability versus composition phase diagrams. However, in the former approach, the accuracy is lower than in QM methods, and the method is not applicable to all systems; while in the latter approach, finding the correct GS depends on how good the initial guess

is or whether experimental data is available. To overcome these limitations, there exists a method, called the cluster expansion method, which combines quantum mechanical calculations with statistical mechanics.

The cluster expansion (CE) technique [34, 35], which is based on the configurational dependence of the energy, can be used to find the ground state structures or to study disordered phases. It involves parametrizing the energy of an alloy in terms of its configurations, as is done in an Ising model. Once we have obtained reliable parameters for a particular system, the simplified model allows us much faster calculation of, e.g., temperature-composition phase diagrams, by using statistical mechanics tools such as Monte Carlo simulations [36]. The advantages of this technique are: (a) it requires as an input first principles calculations of only a few ordered structures for which there exist reliable methods such as density functional theory; thus, the CE method can be applied to insulating, semiconducting and metallic alloy systems [37], (b) it is applicable not only for energies, but also for any property which depends on configurations of the system, such as bond lengths [38], volumes [39] and band gaps [40, 41], and (c) it has been shown that the cluster expansions effectively reduce noise in the input data [42–44]. In the next section, the cluster expansion technique has been discussed in detail.

2.3.2 Framework of the Technique

The cluster expansion technique is a lattice model based technique, similar to the Ising model. Within its framework, a configuration σ is defined for

a binary alloy A-B by specifying the occupation for each lattice site by an atom A or B:

$$\sigma \equiv \{\hat{S}_i\}, \qquad i = 1, 2, \cdots, N, \tag{2.25}$$

where N is the number of lattice sites in the system. The occupation variable is defined as,

$$\begin{aligned} \hat{S}_i &= +1 \qquad \text{if site } i \text{ occupied by an atom } B \\ &= -1 \qquad \text{if site } i \text{ occupied by an atom } A. \end{aligned} \tag{2.26}$$

Then the energy in terms of clusters of lattice points can be written as [34,35]:

$$E_{CE}(\sigma) = J_0 + \sum_i J_i \hat{S}_i(\sigma) + \sum_{j<i} J_{ij} \hat{S}_i(\sigma)\hat{S}_j(\sigma) + \sum_{k<j<i} J_{ijk} \hat{S}_i(\sigma)\hat{S}_j(\sigma)\hat{S}_k(\sigma) + \cdots, \tag{2.27}$$

for a configuration σ. Here, the configurational dependence comes only through occupation variables, as the interaction energies J's are independent of the configuration σ. Each summation in this equation corresponds to a sum over different clusters, for example, the first summation is over all the point clusters (that is, each lattice point on the lattice), the second is over all the two-body clusters (that is, pairs of lattice sites), the third over all the three-body clusters, and so on. Alternatively, one can write Eq. (2.27) as:

$$E_{CE}(\sigma) = \sum_\alpha m_\alpha J_\alpha \phi_\alpha, \tag{2.28}$$

where α is a cluster which has l lattice points, and the sum is taken over all the symmetry-inequivalent clusters α. The interaction terms J_α are termed

as effective cluster interactions (ECI). For a given cluster α, ϕ_α denotes the average of occupation variables taken for m_α symmetry-equivalent clusters β, which can be written as:

$$\begin{aligned}\phi_\alpha &= \langle \prod_{l \in \beta} \sigma_l \rangle \\ &= \frac{1}{m_\alpha} \sum_{\beta} \sigma_1 \sigma_2 \cdots \sigma_l. \end{aligned} \tag{2.29}$$

ϕ_α is also known as a many-body or multipoint correlation function for the cluster α.

One needs to find the values of all J's so as to determine the energy of any arbitrary configuration σ. This requires the calculation of 2^N interaction energies to describe the energies of 2^N configurations. The equation can be written in a matrix form, and the exact solution is possible if the matrix of occupation variables is non-singular. It has been proved that this description of configurational energy is exact because the cluster functions form a complete basis set of configuration functions [34]. However, the determination of 2^N interaction terms will be as difficult as the calculation of energies for 2^N configurations. The usefulness of this technique comes from the fact that, in general, one can truncate this series to a small number of terms, as it converges rapidly for most systems. This can be understood intuitively, as the farther two sites are, the less is the interaction between them. However, there are no rules on how many and which ECI terms need to be included in the solution, so as to get a converged solution. In the past, the truncation of the series was done by a trial and error approach so as to get good agreement

with experimental results.

2.3.3 Determination of ECIs

There exist several methods which can be used to obtain values of ECIs; some of these are briefly described in this section. Fitting to the experimental phase diagram is one of the earlier techniques used to evaluate the J's [45,46]. However, the availability of data will restrict the number of terms used in the fitting and this approach cannot be used to explore systems which have not been studied experimentally.

Instead, one of the simplest methods that can be used is a structure inversion method [47]. In this method, a truncated form of Eq. (2.28):

$$E_{CE}(\sigma) = \sum_{\alpha=1}^{n_c} m_\alpha J_\alpha \langle \prod_{l \in \beta} \sigma_l \rangle, \tag{2.30}$$

is fitted by using the *ab initio* energies for a small number of ordered structures. Here the infinite sum in Eq. (2.28) has been truncated to instead include only n_c cluster figures. The fitting can be done in one of two ways: either by using the same number of ordered structures as the number of ECIs [47], or by using more alloy configurations than the number of ECIs [39]. In the latter case, least-square fitting is used to get a solution set of ECIs which gives a more stable solution, where the least square fit error is given by,

$$\delta_{fit}^2 = \frac{1}{n_s} \sum_{\sigma} w_\sigma [E_{AI}(\sigma) - E_{CE}^{n_c}(\sigma)]^2. \tag{2.31}$$

Here the error is calculated for a set of n_s configurations whose energies are

evaluated both by the *ab initio* and cluster expansions, denoted respectively by subscripts AI and CE. The *ab initio* energy for a configuration σ of an alloy $A_xB_{(1-x)}$, is given by the formation energy of the alloy defined by,

$$E_{AI}(\sigma) = E(\sigma) - xE(A) - (1-x)E(B), \tag{2.32}$$

where $E(\sigma)$ is the energy for a configuration σ, whereas $E(A)$ and $E(B)$ are the energies for pure A and B solids. The number of clusters used for fitting n_c is less than or equal to the number of structures n_s. The special case where $n_s = n_c$ is the original structure inversion method. The constants w_σ are weights associated with each configuration σ, which can be used to emphasize more important structures such as ground state structures. Furthermore, an additional modification to include the effect of relative stabilities of different structures has been suggested to improve predictability [48]. The structure inversion method can take into account the effect of atomic relaxations on the alloy energy by allowing geometry relaxations in the *ab initio* calculations [49]. Usually around 30-40 ordered structures are sufficient to give a good converged CE solution. However, if there are long-range elastic effects present in the system, these will result in a slow convergence, and then it might be required to use a much larger database of ordered structures to get the J's.

2.3.4 Cross Validation Method

This method was proposed to address the question of how to decide a good truncation point while fitting with a limited number of structures [50–52].

Inclusion of too few clusters may lead to a non-converged solution and hence incorrect CE-calculated energies, and too many terms can lead to overfitting of the data, reducing its predictive power for the configurations not included in the fit. The criterion of the least mean-squared error used in the structure inversion method will not be sufficient for the problem of overfitting. To overcome this problem, a method of cross validation (CV) [53] from statistics is used, which can estimate the prediction power of the CE [50]. In this method, the set of input data (that is a set of ordered alloy configurations) is divided into two subsets – one subset is used to fit Eq. (2.30) and determine an optimal cluster set, and then this solution is used to calculate the energies of the configurations belonging to the second subset $\{p\}$. Thus this allows a direct comparison of the "predicted" values with the *ab initio* energies.

Here the strategy followed is to exclude, say, n_{ex} configurations from the original data set, then find a solution cluster set using the remaining $(n_s - n_{ex})$ structures. Now use this cluster set, say, $\{n_o\}$, to predict the energies of n_{ex} excluded configurations, and compare the predicted energies with the *ab initio* energy. The predictive power can be gauged by calculating the prediction error or the cross validation score, defined as:

$$\delta^2_{CV} = \frac{1}{n_{ex}} \sum_{\{p\}} w_p \Big(E_{AI}(p) - E^{\{n_o\}}_{CE}(p) \Big)^2, \tag{2.33}$$

where the sum is taken over all the configurations $\{p\}$ which were excluded from the original data, and $E^{\{n_o\}}_{CE}$ are the CE-calculated energies obtained using the optimal solution $\{n_o\}$. This is usually called the "leave-n_{ex} out" technique. The optimal cluster set is the one which minimizes both the

fitting and prediction errors. To get this solution, we start with a large pool of clusters and then calculate the least-square fitting error and the CV score using the leave-n_{ex} out scheme. Then one or more clusters are removed from the initial pool, such that the increase in the errors is minimum. The removal of clusters and the calculation of errors with the new reduced cluster pool is repeated several times, so as to get a small cluster set; removal of even a single cluster from this set may result in a large increase in the errors. A large increase in the error indicates that the cluster figures in this small set are dominant and cannot be excluded. To ensure that the initial choice of clusters in the pool does not affect the solution, in the work in this thesis, we have started with about five to ten different pools.

We have used the cross validation method to determine the optimal expansions for the enthalpy of mixing of Fe-Au/Mo(110) in Chapter 5. It is implemented in the variational cluster expansion (VCX) code; see Refs. [43,44].

Chapter 3

Structural and Magnetic Properties of Surface Alloys: M_xN_{1-x}/Ru(0001)

3.1 Introduction

3.1.1 Alloys

Alloys are defined as a solid solution of two or more metals, or at least a homogeneous mixture containing a metal as its major component. They have been used through many centuries for their enhanced properties compared to any of their constituent elements.

Alloys can be classified into two different types based upon the structural arrangement: A first type is substitutional alloys, in which the constituent metals are of similar "size". These are formed by substituting the atoms of

one component into the other. For example, brass is an alloy made up of copper and zinc. The formation of a solid solution in bulk substitutional alloys is governed by some empirical rules known as the Hume-Rothery rules [54] which can be stated as follows:

1. Atomic size factor rule: If the difference in size of the elements is greater than $\pm 15\%$, lattice distortions can restrict the formation of a solid solution.

2. The electronegativity rule: If the electronegativities (ionization energies) of the two elements are close, the formation of a solid solution is favored.

3. Valency rule: A metal will dissolve another metal of greater valency much more than a metal of lower valency.

4. Crystal structure rule: If the two elements have the same crystal structure there could be formation of a solid solution.

A second type of alloy is an interstitial alloy, in which atoms of one of the constituent elements are significantly smaller than the other, and hence occupy the interstitial voids in the crystal structure of the bigger atoms. For example, carbon atoms sit in the interstitial sites of iron to form steel.

In the early days, before the full understanding of microscopic crystal structure or detailed composition of alloys was achieved, alloys were mainly used for their enhanced mechanical properties. Since the modern era of metallurgy started, alloys have also been designed for their thermal and magnetic

properties. For example, FeNi alloys known as invars have almost zero coefficient of thermal expansion over a wide range temperature; these were invented in 1896. Heusler alloys such as Cu_2MnAl, studied for the first time in 1903 [55], are ferromagnetic even though the constituent elements are not. This is a result of a double-exchange mechanism between neighboring magnetic ions, e.g., Mn atoms.

3.1.2 Surfaces

The study of surfaces is important for applications such as catalysis and magnetic storage. At the surface, periodicity is broken along the direction perpendicular to the surface, and the coordination number of the atoms at the surface is less than that of bulk atoms. As a consequence, the atomic and electronic structure at the surface can be drastically different from that in the bulk. If atoms on the surface minimize their energy only by changing the interatomic distance between layers while retaining the bulk-terminated structure, it is known as 'surface relaxation'. On the other hand, if atoms are displaced from their bulk-truncated positions so as to change the surface unit cell, it is known as 'surface reconstruction'. While studying structural properties of surfaces, two important physical quantities are the surface energy and the surface stress. These quantities largely drive relaxation and reconstruction.

There are different experimental techniques which can provide information about the atomic positions in the surface layers and the composition at the surface. Some of the most commonly used techniques are low-energy

electron diffraction (LEED), electron microscopy such as transmission electron microscopy or scanning electron microscopy, scanning probe microscopy such as scanning tunneling microscopy (STM) which can provide atomic resolution, ion scattering, photoelectron diffraction, atom probe field ion microscope, etc. A brief summary of these techniques has been given, e.g., by Bardi [56]. The increased sensitivity of such structure-determining probes has helped to study the atomic arrangements at surfaces, and thus to understand surface properties better.

3.1.3 Magnetism in Low-dimensional Systems

Most isolated atoms have a net magnetic moment due to the spin and orbital angular momenta of the electrons. However in the bulk solid form, only a few elements, such as iron, retain a net magnetic moment. This reduced magnetic moment is attributed to the interatomic exchange interaction and non-central crystal-field quenching [57].

In general, a reduced dimensionality is found to enhance the magnetic moment of the system. This can be seen, for example, in two-dimensional (2D) thin films, one-dimensional (1D) linear chains and zero-dimensional nanoclusters. This observation can be rationalized by the Stoner argument [58]. The Stoner model for ferromagnetism shows that itinerant electrons can have a net magnetic moment if it is energetically favorable for electrons to occupy one of the spin directions. This is decided by two competing energies: the exchange interaction between the electrons favors ferromagnetism, while on the other hand, preferentially occupying only one spin direction costs kinetic

and potential energy. However, if the density of states (DOS) at the Fermi level is large, then filling of higher-energy states will not cost as much energy as is gained by the exchange interaction. In low dimensional systems, atoms have a reduced coordination number, which leads to narrower and higher peaks in the DOS, and hence increases the tendency towards magnetism.

One manifestation of this tendency is an increase in the magnetic moment at lowered dimensions for ferromagnetic elements. For example, Apsel *et al.* in 1996 [59] did experiments on Ni clusters containing 5 to 740 atoms. They showed that while a Ni_5 cluster has a magnetic moment of 1.81 μ_B per atom, this decreases to the bulk value (= 0.61 μ_B) as the cluster size is increased. This dependence of magnetic moment on cluster size is a highly non-monotonic function, which depends on the geometry and shape of the cluster and its surface area. Similar observations for Fe, Co and Ni clusters have been made [60, 61] using both experimental techniques and theoretical models.

Another manifestation of this tendency leads to induced moments on the clusters or surfaces of $4d$ transition metals which are non-magnetic in the bulk [62–67]. Using first-principles *ab initio* calculations, it has been shown that $4d$ transition metals such as Ru, Rh and Pd are close to fulfilling the Stoner criterion in the bulk [68], which explains this phenomenon when their coordination is reduced. Also small Pt clusters have been shown to have non-zero magnetic moments using both theoretical calculations and experimental techniques [69–71].

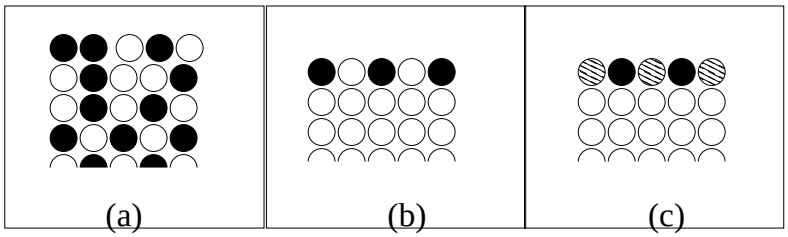

Figure 3.1: *(a) Side view of an alloy surface which has layer-dependent composition near the surface of bulk alloy. (b) and (c) Side views of surface alloys showing two types of surface alloys; in the first one, deposited atoms substitute some of the atoms in the top layer of a substrate to form an alloy restricted to the surface and in the second one, two different metals deposited on a substrate (consisting of a third metal) mix atomically on the surface, but do not diffuse into the bulk substrate.*

3.1.4 Alloys Surfaces versus Surface Alloys

An alloy surface is the surface of a bulk alloy, where the composition at the surface may be different from that in the bulk phase (see Fig. 3.1(a) for a schematic depiction) due to phase segregation [72, 73]. These have long been studied and are interesting for their catalytic properties, since reaction selectivity and rates depend upon composition. However, a more recent field of study is surface alloys, where mixing between constituents is restricted to a few surface layers only (see Figs. 3.1(b) and (c)). Such surface alloys display a rich phenomenology of structural and magnetic phase transitions as a function of coverage. Another interesting feature observed is that metals which are immiscible in the bulk can mix atomically at the surface. These surface alloys have been suggested to be stabilized by strain due to atomic-size mismatch [74]. These issues are discussed in detail in the next section.

3.2 Previous Work on Surface Alloys

In recent years, there have been a large number of studies on the structural, electronic and magnetic properties of metallic thin films on a metal substrate. This field is gaining more attention due to the observed catalytic, electronic and magnetic properties of thin films. The nucleation and growth mode of a metal A on another metal B is, in general, a function of temperature and the total coverage of A. In earlier studies, the growth morphology of metal-on-metal heteroepitaxial systems was predicted from thermodynamical equilibrium considerations, that is, comparing the surface energies (γ_A and γ_B) of the two metals and the interface energy (γ_i) [75]. If $\gamma_i \leq 0$, then the two metals will mix to lower their energy. If $\gamma_A + \gamma_i < \gamma_B$, there will be layer-by-layer growth, otherwise there is island formation. The different growth modes of A on B are usually classified into three categories [76] as shown schematically in Fig. 3.2. Even though this approach neglects details of atomic structure, it is still useful as a starting point to understand growth morphology and intermixing. To understand formation of complex structures, one has to consider strain energy (misfit between the lattice parameters of the two metals), mobility of overlayer atoms on the surface, and possible reconstruction of the overlayer and/or substrate at the interface.

There have been reports that two metals which are immiscible in the bulk due to a large atomic-size mismatch, can form stable 2D surface alloys e.g., Au on Ni(110) [77]. For such systems, using a simple model containing only strain energy, Tersoff in 1995 [74], showed that surface-confined mixing is, in general, expected in systems dominated by atomic-size mismatch. The

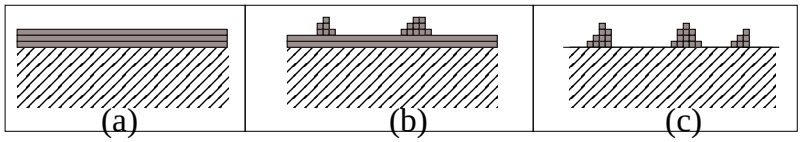

Figure 3.2: *Different growth modes of deposition of a metal A on another metal B: (a) Frank–van der Merwe growth mode in which metal A completely wets the surface of B to give layer-by-layer growth; (b) Stranski–Krastanov growth mode in which an incomplete wetting results in island formation after the layer-by-layer growth for a few monolayers and (c) Volmer–Weber growth mode consists of formation of islands with no wetting of the surface.*

same atomic-size mismatch leads to immiscibility in the bulk, as explained in Sec. 3.1.1 above. These systems are referred to as strain-stabilized surface alloys.

Another type of strain-stabilized alloy (see Fig. 3.1(c)) has also been considered. These can be termed as tertiary surface alloys, in which, two bulk-immiscible metals A and B are deposited on a substrate S, and A and B mix to form a 2D alloy on the surface. The reduction of strain has been suggested as the driving mechanism for alloy formation by Stevens and Hwang for the system consisting of an Ag-Cu monolayer on Ru(0001) [78], experimentally first observed by Schick *et al.* [79, 80]. For such systems, e.g., Pd-Au on Ru(0001) [81] and Pb-Sn on Rh(111) [82], the strain induced by the substrate plays an important role in the surface alloying mechanism. In general, it has been suggested that the strain energy can be minimized by mixing of two overlayer metals, if the bulk nearest neighbor (NN) distance of one of the overlayer metals is greater than that of the substrate and that for the other overlayer metal is less than that of the substrate. However, in some cases, co-deposition of two metals on the third metal can lead to a spontaneous organization of patterns having alternating domains of individual

metals [83, 84]; these also may be desirable for certain applications.

With recent improvements in experimental techniques, it is possible to control the growth rate and temperature with greater accuracy, and a number of new phases have been observed in such systems. For example, the Ag/Cu(100) system was first studied by Palmberg and Rhodin [85] in 1968 using LEED, and was identified to have a c(10×2) pattern upon deposition of 1 ML (monolayer) of Ag. The observed diffraction pattern was explained by proposing that the silver atoms form a close-packed, hexagonal Ag(111)-like overlayer structure on the Cu(100) substrate which has a square symmetry. This pseudo-hexagonal structure was confirmed as the lowest energy configuration after further experimental studies using angle-resolved photoemission [86,87], and electron-energy-loss spectroscopy [88], and theoretically using a tight-binding molecular-dynamics scheme [89]. The intermixing of Ag with the Cu(100) surface had been ruled out, until Sprunger *et al.* in 1996 [90] showed, using variable-temperature STM, that though below 250 K earlier conclusions held true, above 300 K, a substitutional Ag-Cu alloy forms. Such examples underline the requirement of careful study of structural properties and the energetics which drive these structures.

Of particular relevance to our study is the work on the system of submonolayer films of Co-Ag/Ru(0001) [91–94]. All the three elements are immiscible in the bulk with each other due to a large size mismatch. The substrate, Ru, has a bulk NN distance greater than that of bulk Co and smaller than that of bulk Ag by about 7% and 8% respectively. As already discussed, stress due to atomic-size mismatch between the film and substrate can influence film structure. In such multi-component films, there exist two stress relief

mechanisms: (i) formation of dislocations, which occurs above certain critical thickness of film, and (ii) alloy formation. Thayer *et al.* [92, 94] have observed a number of distinct types of phases in this system: the first is an alloy phase with lower stress and higher commensurability than in pseudomorphic single-component films; a second phase consists of a pure Ag phase with dislocations, and the third phase has a coexistence of the first two phases. The Co-rich submonolayer exhibits an alloy-like structure, but Ag in this alloy is not atomically dispersed and forms irregular droplets. For compositions containing more than 40% Ag, the film decomposes into two distinct phases, an alloy phase similar to the irregular droplet structure and a pure Ag phase with a misfit dislocation structure.

For this system, researchers had expected an atomistically mixed alloy formation based on the argument by Tersoff [74]. The argument was that a surface with average NN spacing approximately equal to the NN spacing of the substrate will reduce the strain significantly. However the experimental observations do not accord with this argument. To explain this, they have suggested the chemical interaction as a competing driving force for structure formation, since the chemical interaction in the system favors Co-Co and Ag-Ag bonds rather than Co-Ag bonds [94]. Comparing 2D Frenkel-Kontorova model calculations with the strain measurements from STM images, they have also estimated the strain relaxation energy [93, 94]. These observations lead to questions such as (i) is there a criterion based on atomic size that will predict whether or not a surface alloy will form? (ii) what is the relative importance of elastic and chemical interactions?

Furthermore, magnetic properties of thin films are gaining huge attention

because of their applications in magnetic storage devices. A number of phenomena observed at the surface such as localized electronic states, magnetic moment enhancement, perpendicular magneto-crystalline anisotropy [95, 96] and complex magnetic ordering [97] are not only of basic physical interest, but have practical applications too. Experiments performed on systems consisting of thin magnetic films on a non-magnetic substrate demonstrate that the magnetism can affect the structure and stability of surfaces [98]. Also the reverse is true, i.e., the presence of the surface affects magnetic properties such as magnetic ordering and moments. Some examples of systems in which these effects have been observed are Fe/Cu(100) [99], Mn/Ag(001) [100], Mn/Cu(100) [101] and Mn/Cu(111) [102].

Using *ab initio* calculations, one can separate the contributions of strain, surface energies and magnetization on the growth and geometry of the films and so get greater insight into the interrelations between these quantities. For example, Blügel *et al.* [101] have shown, using the full-potential augmented plane-wave method, that for the Mn layer on Cu(100), buckling of Mn atoms occurs due to a magnetic ground state, and is totally absent in the non-magnetic state. This buckling of the overlayer has also been confirmed by LEED experiments.

3.3 Systems under Study

In this work, we have studied the formation of binary surface alloys ($M_xN_{(1-x)}$) on a substrate, S (the Ru(0001) surface), where M is an element which is

(Å)	Pt	Au	Ag	Cd	Pb
Fe	2.63	2.69	2.69	2.73	2.99
Co	2.64	2.70	2.70	2.75	3.01

Table 3.1: *Average of NN spacings of M and N in their bulk structures: Compare these numbers with a_s NN distance of Ru in bulk = 2.70 Å. All the values used in this table are experimental values, taken from Ref. [103]*

ferromagnetic in the bulk (Fe or Co) and N denotes an element that is non-magnetic in the bulk (Pt, Au, Ag, Cd or Pb). Here, x is the fraction of "magnetic" element. The selection of non-magnetic element was based on the atomic-size mismatch between the S, M and N. In their bulk structures, both the magnetic elements have a NN spacing less than that of Ru (approximately 7-8%), thus non-magnetic elements all having a NN spacing greater than that of Ru are selected. The non-magnetic elements are selected so as to have a large variation in size: the NN distance of Pt is 3% more than that of Ru, whereas this difference for Pb is almost 30%. This large variation in size should enable us to recognize size-dependent trends in the alloy formation, if there are any. We have computed the averages of bulk NN spacing of M and N, given in Table 3.1. When we compare these values with the Ru NN spacing in the bulk (a_s = 2.70 Å), we note that the nearest match is for alloys with Ag and Au, while Pb alloys seem to be the worst choice. We note here that out of the ten systems studied here two of the systems have been studied previously: Co-Ag/Ru(0001) [91–94] and Fe-Ag/Ru(0001) [84].

In the systems we are studying, the atomic-size mismatch between the substrate element and the overlayer element is rather large, which leads to the question of whether the pseudomorphic geometry of a monolayer is stable

against reconstruction. In earlier experiments, it has been shown that a single monolayer of Fe [104], Co [105] and Pt [106] on the Ru(0001) surface does not reconstruct, whereas that of Au [107] and Ag [78, 107, 108] reconstructs; there is no experimental data available for Cd and Pb deposition on the Ru(0001) surface. In this chapter, we have not considered the possibility of reconstructions or dislocations. We have assumed a pseudomorphic single overlayer in which the atoms are allowed to occupy one of the two possible hollow sites as explained below. This issue will be discussed further later.

In crystallography, there are two possible closed-packed structures, face-centered cubic (fcc) and hexagonal closed-packed (hcp). The atomic arrangement in the two differs only in atomic plane stacking, as shown in Fig. 3.3. Out of the different crystallographic surfaces for these closed-packed structures, the (111) surface of fcc and the (0001) surface of hcp are the closed-packed surfaces. In heteroepitaxy on the closed-packed surfaces, it is energetically favorable for the deposited atoms to occupy one of the hollow sites and hence atoms in the surface layer can either sit vertically above atoms in the third layer to give $\cdots ABA$ stacking at the surface (called the hcp site) or can occupy the other set of hollow sites to give $\cdots ABC$ stacking at the surface (called the fcc site).

To enable us to get different alloy compositions, we need to consider a larger unit cell than the (1×1) cell for the surface. We have used a (2×2) surface unit cell which has four atoms per layer. This particular unit cell allows us to study five different compositions as shown in Fig. 3.4. For the unit cell we have considered, each composition permits us to consider only one non-equivalent configuration.

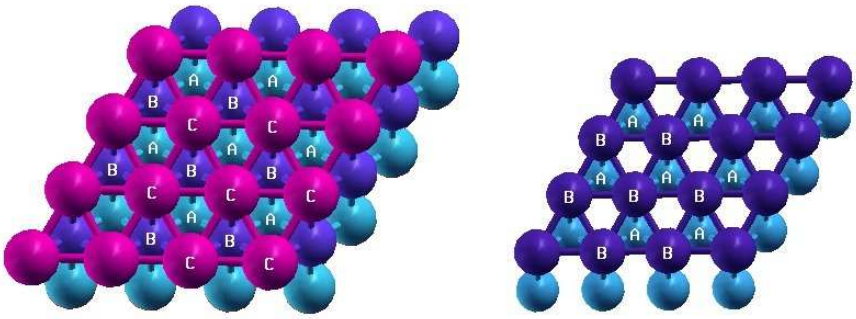

Figure 3.3: *Closed-packed structures: Atoms in each plane A (light blue), B (dark blue) and C (magenta) form a closed-packed layer in 2D where each atom is surrounded by six other atoms in the plane. Note the hexagonal symmetry in a plane. The stacking of the type $ABCABC\cdots$ (left) leads to the fcc structure, while $ABABAB\cdots$ kind of stacking (right) gives the hcp structure.*

3.4 Computational Details

The calculations are done using *ab initio* spin-polarized (SP) density functional theory (DFT) with the PWscf package of the Quantum-ESPRESSO distribution [29]. However, in order to gauge the effects of magnetism on alloying, we have also done some non-spin-polarized (NSP) calculations. A plane-wave basis set is used with a kinetic energy cutoff of 20 Ry and a charge-density cutoff of 160 Ry. Convergence with respect to the basis size and the k-point grid has been carefully verified for the bulk structures of all the elements. A (4×4) Monkhorst-Pack mesh of k-points [19] is used for Brillouin zone integrations for the (2×2) surface unit cell.

Ultrasoft pseudopotentials [18] are used to describe the interaction between ions and valence electrons. For the exchange correlation functional, a Generalized Gradient Approximation (GGA) of the Perdew-Burke-Ernzerhof form [11] is used. As all the systems are metallic, the Methfessel-Paxton smearing technique [22] is used with a smearing width equal to 0.05 Ry.

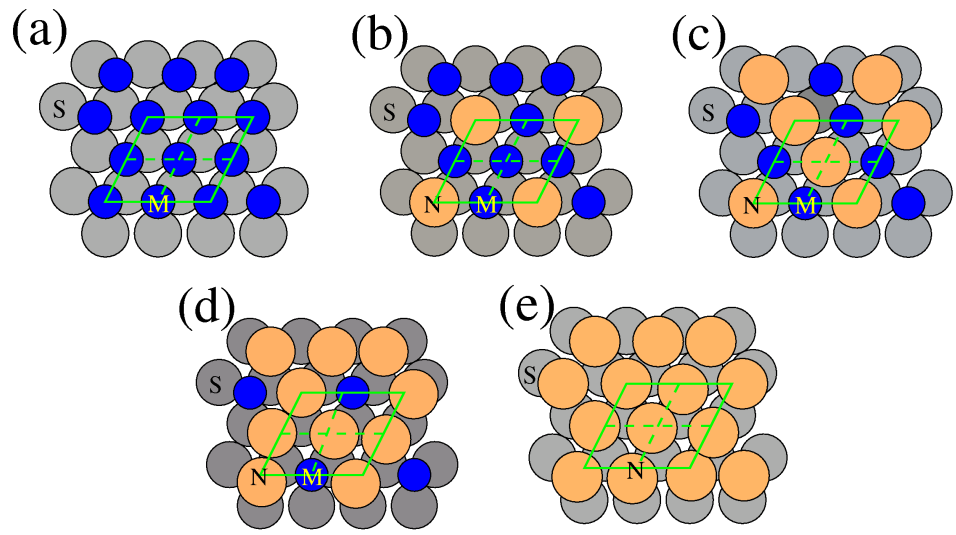

Figure 3.4: *Top view of the system studied : x = 1.00, 0.75, 0.50, 0.25 and 0.00 (from top left) with 2×2 surface unit cell shown (green solid line). The S denotes the substrate atoms (gray) and M and N denote magnetic (blue) and non-magnetic (orange) elements.*

We have used a supercell approach to study the surface within periodic boundary conditions. We have performed convergence tests with respect to the number of atomic and vacuum layers to ensure there is no spurious interaction between two surfaces via the "bulk" or the "vacuum". Based on these convergence tests, we use six Ru layers to model the substrate and seven vacuum layers (approximately 17.38 Å). For energetics calculations, we have deposited an alloy overlayer on only one side of the substrate; whereas to get the variation of the surface stress of M or N on S with in-plane distance we have used symmetric slabs. To get the lowest energy structure, we have allowed the overlayer alloy and the three topmost layers of Ru to relax. To obtain the relaxed structures, Hellmann-Feynman forces are used.

This formalism gives us the total energy and magnetization for the whole system. To extract atomically resolved properties, there exists a technique

known as the 'projected density of states' (PDOS) method. In this method, the contribution of each atom is separated out by projecting wavefunctions of the whole system onto the atomic wavefunctions. It gives the density of states (DOS) for all the atomic orbitals separately and for the spin-polarized calculations, spin-up and spin-down DOS are computed separately. Using this method, we have obtained the magnetization for each atom and the DOS at the Fermi level for the total system, as well as for each atom. This helps us to understand effects such as the enhancement of magnetic moment of the magnetic atoms, induced moments on the non-magnetic overlayer atoms and the substrate atoms, and magnetic ordering if present, in detail.

3.5 Results and Discussion

3.5.1 Bulk Calculations

We have first performed calculations for the bulk structures of the substrate element (Ru), magnetic elements (M = Fe and Co) and non-magnetic elements (N = Ag, Au, Cd, Pb, and Pt). For fcc and body-centered cubic (bcc) structures, there is only one parameter (lattice constant, a) to be optimized, but in the hcp structures, one needs to optimize both a and c/a where $c/2$ is the interplanar distance along the [0001] direction. Here we have optimized only a for all structures and used the experimental value of c/a for the hcp structures. The experimental values of c/a [103] used here for Ru, Co and Cd are 1.584, 1.622 and 1.886 respectively. The calculated values of the nearest neighbor (NN) spacing, a_{calc}, for all the bulk elements are listed in Table 3.2

	Element	Structure	a_{bulk}^{calc}(Å)	a_{expt}(Å)	Δa_0%
1	Ru	hcp	2.74	2.70	1.48
2	Fe	bcc	2.47	2.48	-0.40
3	Co	hcp	2.49	2.51	-0.80
4	Pt	fcc	2.83	2.77	2.12
5	Au	fcc	2.93	2.89	1.45
6	Ag	fcc	2.95	2.89	1.92
7	Cd	hcp	3.04	2.98	1.94
8	Pb	fcc	3.56	3.50	1.73

Table 3.2: *The calculated and experimental nearest neighbor spacing in the bulk structure of all the elements under study.* Δa_0 *is the percentage difference in calculated and experimental values.*

below, compared with the experimental values a_{expt} [103]. The errors in NN distances are seen to be small.

The calculated total magnetic moments for bulk Fe and Co are 2.36 and 1.71 μ_B per atom respectively, whereas the experimental values [109] for these are 2.22 and 1.72 μ_B, which are comparable with the calculated values. The calculated values of lattice constants for all elements (except for Cd), and the magnetic moments for the magnetic elements match well with previously reported values [110–115]; the agreement is reasonable considering some of the known shortcomings of different theoretical approaches such as underbinding of GGA. For the bulk cadmium, we were not able to find any previous calculations.

We have calculated the total NSP-DOS for each of the metals considered here in their bulk structures, which is plotted, in the vicinity of the Fermi energy in Fig. 3.5. Note that, the elements which are ferromagnetic in the bulk, i.e. Fe and Co, have higher DOS at the Fermi level than any other elements. Also Pt and Ru, which are shown to get magnetized in the reduced

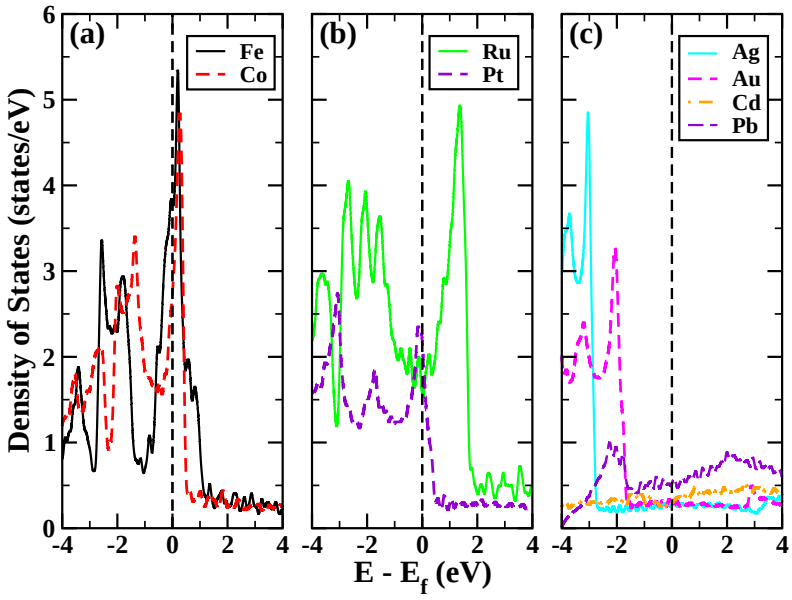

Figure 3.5: *Non-spin polarized density of states in the bulk for (a) Fe and Co, (b) Ru and Pt, and (c) Ag, Au, Cd and Pb in their bulk structure is plotted in the vicinity of the Fermi energy. The DOS at the Fermi level for magnetic elements is the highest among all the metals and among non-magnetic elements, Pt has the highest DOS at the Fermi energy.*

dimensions (as explained in the introduction), have significant DOS at the Fermi level; whereas non-magnetic elements other than Pt have negligible DOS at the Fermi level. This is in accordance with the Stoner argument for ferromagnetism.

3.5.2 Clean Ru(0001) Surface

Before deposition of different elements, we have studied the clean Ru(0001) surface, using a slab having six layers of Ru atoms, out of which the top three layers are allowed to relax. The distance between two adjacent layers

in bulk ruthenium, d_{bulk}, is 2.17 Å, but when allowed to relax, the distance between the topmost layer and the adjacent layer, d_{12}, becomes 2.11 Å, that is the topmost layer undergoes an inward relaxation with respect to the bulk by 2.76%. Also the other two layers adjacent to the topmost layer, which are allowed to relax, relax to distances $d_{23} = d_{34} = 2.18$ Å, undergoing an outward relaxation of 0.46%. The calculated surface energy is 1.13 eV per surface atom, which compares well with earlier reported values [116, 117].

It has been shown that small Ru clusters get magnetized [63, 65–67] due to reduced coordination; however, we have verified that the ground state for Ru(0001) surface remains non-magnetic.

3.5.3 Monolayers of M and N on Ru(0001) Surfaces

For a single-element monolayer ($x = 0.00$ for N/Ru(0001) and $x = 1.00$ for M/Ru(0001)), all the "magnetic" elements M prefer to occupy overlayer hcp sites rather than fcc sites; whereas except for Pt, we find that all the "non-magnetic" elements N prefer to occupy fcc sites. The values of the energy difference between the two stacking sites are given in column two of Table 3.3. In the same table, the third column gives the nearest neighbor interatomic bond length between the overlayer atoms and the Ru atoms in the top layer. The next three columns in the table contain the interplanar distances d_{ij} between layers i and j with the overlayer labelled as "1". Note that, as expected, d_{12} for the monolayer of M (or N) is smaller (or greater) than the interplanar distance of 2.17 Å for the Ru bulk. From the d_{23} values, we find that the topmost Ru layer always relaxes inward ($\sim$ 1-3%) with a

M/N	δE	Bond length S-M/N	d_{12}	d_{23}	d_{34}	σ^{surf}
Fe	-55.9	2.62	2.08	2.15	2.17	-0.139
Co	-88.1	2.56	2.01	2.15	2.17	-0.397
Pt	-3.8	2.79	2.30	2.12	2.18	0.138
Au	7.3	2.95	2.49	2.10	2.18	0.425
Ag	4.9	2.92	2.45	2.11	2.18	0.372
Cd	2.3	2.97	2.51	2.12	2.17	0.135
Pb	1.8	3.00	2.55	2.13	2.17	2.213

Table 3.3: *For monolayers of M or N on Ru(0001), $\delta E(= E_{slab}(hcp) - E_{slab}(fcc))$ is the difference between total energies of the slab when the overlayer occupies hcp and fcc sites, in units of meV per surface atom; d_{ij} is the interplanar distance between layers i and j with layer '1' being the overlayer (all distances are in Å); σ^{surf} is the surface stress for a monolayer of M or N on S in units of $eV/Å^2$.*

value depending on the overlayer element, whereas the second Ru layer shows either no relaxation or a slight outward relaxation. In the last column of the table, the calculated surface stress in units of eV/Å^2 is given; the surface stress calculations are explained in Sec. 3.6.2.

The magnetic moments on the Fe and Co monolayers when put on the Ru surface are found to be 2.93 and 1.78 μ_B per magnetic atom respectively; these values correspond to the local moments (that is, the induced moments on Ru are not included) calculated using PDOS. For both Fe and Co, the moments are higher than in the bulk (given in Sec. 3.5.1) as expected from the Stoner argument.Though Pt clusters are shown to have non-zero magnetic moment [118], we find that there is no magnetic moment induced on the Pt/Ru(0001) system.

The monolayers of magnetic elements induce magnetic moments on adjacent Ru layers. This induced magnetic moment shows a decaying oscillatory nature, as shown in Fig. 3.6, in which we have plotted the induced moment

on Ru layers as a function of the distance from the overlayer. This oscillatory nature is similar to the Ruderman-Kittel-Kasuya-Yoshida (RKKY) interactions [119] which exist in the system consisting of magnetic impurities in a non-magnetic element. Note that the Co monolayer has induced a ferromagnetic moment on the first Ru layer with magnitude 0.18 μ_B, whereas the Fe monolayer induces an antiferromagnetic moment on it, having a very low magnitude $\sim$ 0.06 μ_B. However for Fe/Ru(0001), the second layer of Ru has a larger induced moment ($\sim$ 0.1 μ_B) than the first layer, unlike the Co case, again with the antiferromagnetic (AFM) coupling to the Fe layer as was observed by Hardrat, *et al.*, [120]. We can fit data points with a simple oscillatory function [97] of the form:

$$\mu(z) = \mu_0 \frac{sin(2qz + \phi)}{(2qz)^2}, \tag{3.1}$$

where μ is the induced magnetic moment on an atom at a distance z from the magnetic atom, and q and ϕ are a wavevector and phase which are determined by fitting. The fits for each M/Ru(0001) system are shown with lines in Fig. 3.6. However, we note that this fit need not be unique, one can obtain a rather good fit with other sets of parameters as has been pointed by previous authors [97].

3.5.4 Alloy Monolayers (M_xN_{1-x}) on Ru(0001)

For all surface alloy configurations considered here, we find that the overlayer atoms prefer to be at hcp sites over the fcc sites with an energy difference of the order of 5-75 meV per surface atom. The alloy layers exhibit buckling

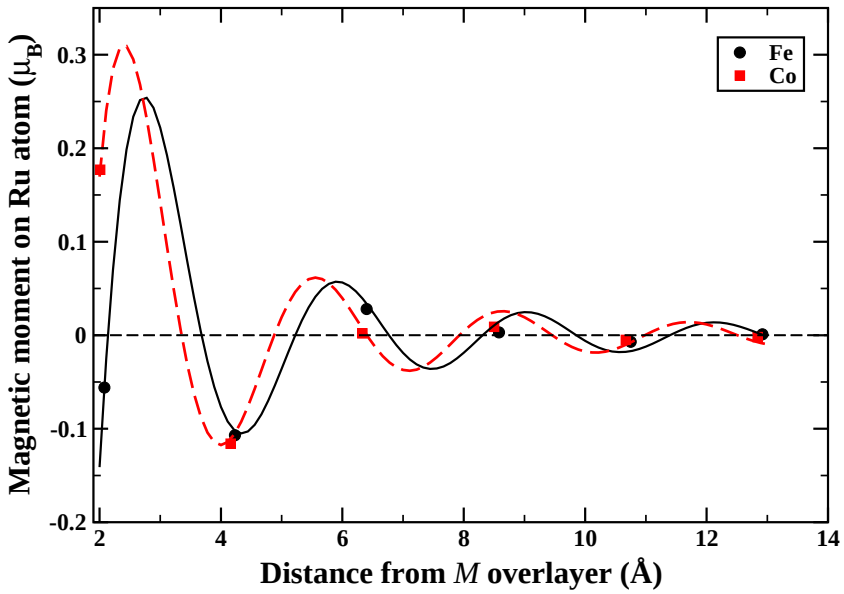

Figure 3.6: *Induced magnetic moments on Ru layers: The variation of magnetic moments induced on Ru layers by overlayers of magnetic elements as a function of the distance from the overlayer is shown for Fe (circles) and Co (squares). We have fitted the ab initio data with a simple oscillatory function of the form given in Eq.* (3.1)*; the fits are shown with solid (Fe) and dashed (Co) lines.*

upon permitting geometric relaxations; an example is shown in Fig. 3.7. The buckling follows the trend expected from the atomic-size mismatch. Thus, Pt alloys do not show any visible buckling, whereas Pb alloys show the maximum buckling among the N's considered.

In order to gauge the stability of the surface alloys, we have calculated the formation energy, ΔH, of an alloy relative to the phase-segregated monolayers of M and N on Ru(0001), which we define as:

$$\Delta H = E_{slab}(M_x N_{1-x}/S) - xE_{slab}(M/S) - (1-x)E_{slab}(N/S), \qquad (3.2)$$

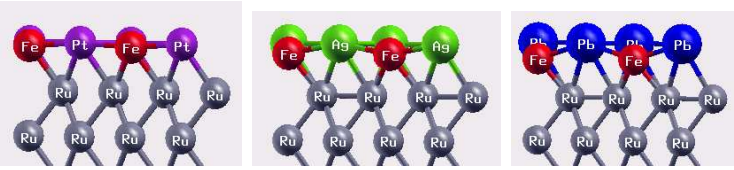

Figure 3.7: *Relaxed geometries for (a) Fe-Pt, (b) Fe-Ag and (c) Fe-Pb with x =0.25. Here gray, red, purple, green and blue spheres represent Ru, Fe, Pt, Ag and Pb atoms, respectively. Note that the amount of buckling increases from Pt to Ag to Pb, in accordance with the increase in the atomic size of N, resulting in a larger size mismatch between Fe and N.*

where $E_{slab}(A/S)$ is the ground state energy per surface atom for a single monolayer of A on substrate, S. When ΔH is negative, the two metals prefer to mix rather than to segregate in separate islands, and hence the alloy phase is more stable than the phase-segregated one.

We have plotted SP-ΔH (shown with solid lines) as a function of composition x in Fig. 3.8. For all the pairs of elements, ΔH is negative (indicating atomically-mixed alloy configurations are stable), except for Co-Ag alloys; this is in accordance with the experimental observation of phase-segregation of Co-Ag/Ru(0001) alloy [92, 94]. One can see that for all the magnetic elements, Pb alloys are the most stable, whereas Ag alloys are the least stable. This result is not according to our expectation based on the size based selection criterion (see Sec. 3.3). Also all the curves are approximately symmetric about x=0.5; this points towards the fact that pairwise interactions are dominant. However, though both the magnetic elements have almost the same bulk lattice constant, the values of ΔH and the order of stability are not similar in the two cases. Similarly, Au and Ag which have almost the same lattice constant in the bulk display distinctly different behavior: M-Au alloys are stable, whereas Fe-Ag alloys are right at the boundary of stability, and

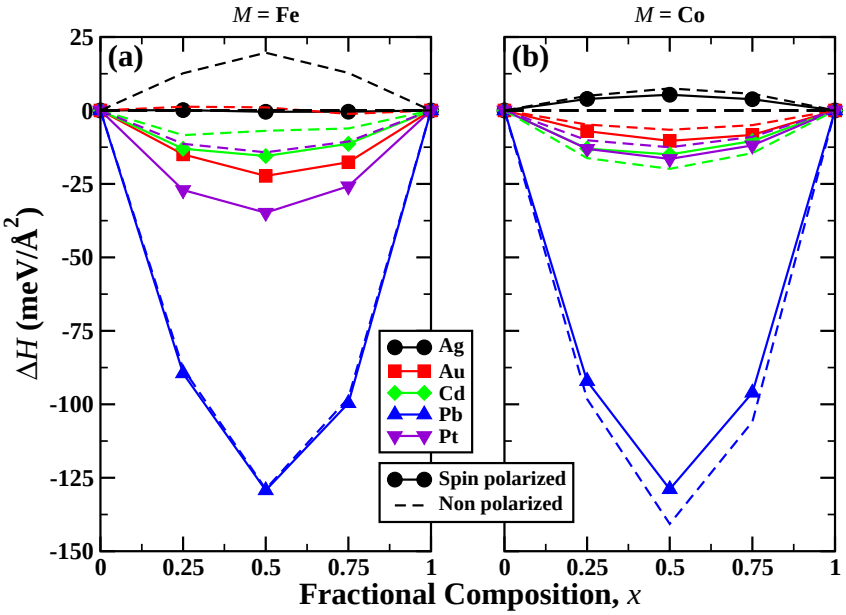

Figure 3.8: *Formation energy per unit surface area for each configuration as a function of x, the fraction of magnetic elements: It is plotted for (a) Fe and (b) Co alloyed with non-magnetic elements. The solid and dashed lines show results for spin-polarized and non-spin-polarized calculations respectively.*

Co-Ag alloys are unstable. These observations suggest that in some cases chemical interactions are more dominant than elastic interactions.

Next, to see the effect of magnetism on mixing, we have also calculated and plotted the NSP-ΔH (shown with dashed lines) in Fig. 3.8 as a function of x. For all the systems, except for Co-Cd and Co-Pb, mixing is more favorable when the systems are spin-polarized than when magnetism is suppressed, as has been found before also for the monolayers of $3d$ transition metals on the Cu(100) surface [98]. The effect of magnetism on mixing is maximum for Fe-N alloys (except for Fe-Pb alloys), followed by Co alloys. This can be understood from the fact that the magnetic moment is larger on

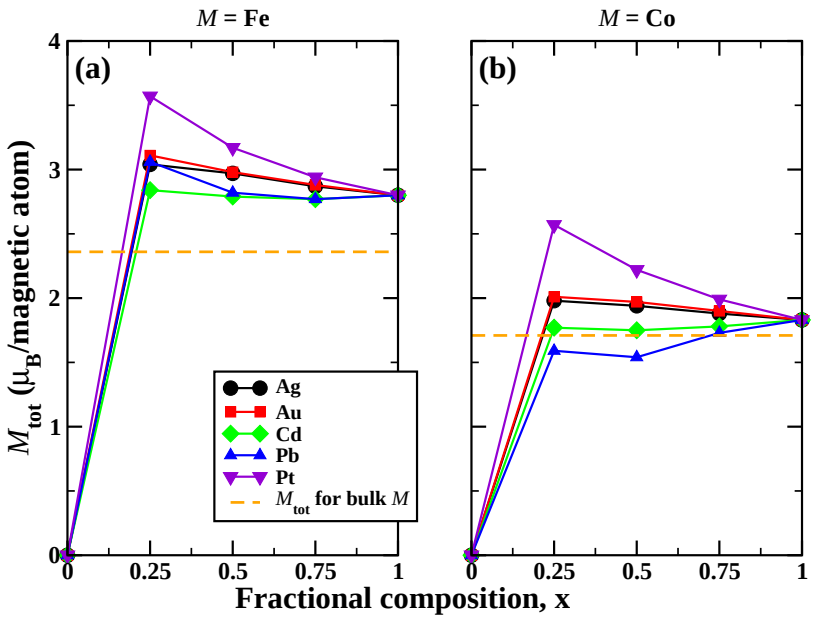

Figure 3.9: *Magnetic moment μ_B per magnetic atom of each configuration as a function of x: The results are plotted for (a) Fe and (b) Co alloys. For comparison, the magnetic moment of M in their bulk structures are shown by dashed line.*

Fe alloys than Co alloys (see Fig. 3.9).

In Fig. 3.9, we have plotted the calculated total magnetic moment, per magnetic atom, as a function of composition for each configuration. Note that these moments include induced moments on the "non-magnetic" overlayer atoms and the substrate atoms. We have plotted the bulk magnetic moment for each magnetic element as a dashed line, on the same plot, for comparison. For Fe alloys, the moments for the alloy systems are always greater than that for bulk Fe. The same is true for Co alloys, except for Co-Pb alloys. As the percentage of magnetic atoms increases, in the case of Fe alloys, M_{tot} per magnetic atom decreases; for Co alloys, M_{tot} per magnetic atom increases for

N = Cd and Pb, whereas it decreases for N = Ag, Au and Pt.

We have observed that there are induced moments on N atoms and Ru layers, and in some cases these values are quite significant. Among all the N elements considered by us, M-Pt alloys acquire the highest moments because of the highest induced moments on the Pt atoms; this is expected based on the bulk NSP-DOS shown in Fig. 3.5. For Ru layers, Co alloys result in higher induced moments than that for Fe, which was also seen for single-component M/Ru(0001) (as was shown in Fig. 3.6). The pattern of such induced moments is rather complex for all the systems, with both ferromagnetic (FM) and antiferromagnetic (AFM) alignments present. One such example has been shown in Fig. 3.10 for the $Fe_{0.50}Cd_{0.50}$/Ru(0001) configuration. This suggests that the surface alloy systems have a large number of interactions present, and understanding all the properties will need a very detailed analysis.

3.6 Analysis

We now analyze in detail the *ab initio* results for the magnetic properties and the miscibility of surface alloys. One needs to take into account the fact that both the structural and the magnetic properties depend on the surface effects as well as alloying effects.

3.6.1 Magnetic Properties

Initially we have analyzed magnetic properties of these surface alloys. According to Stoner's criterion for ferromagnetism, the higher the paramagnetic

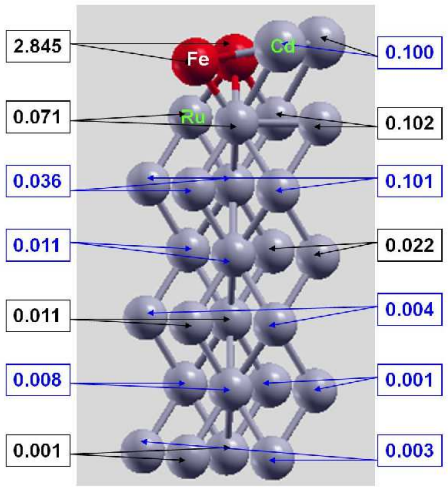

Figure 3.10: *Magnetic moments induced in $Fe_{0.50}Cd_{0.50}$/Ru(0001) system: We have shown a side view of the system $Fe_{0.50}Cd_{0.50}$/Ru(0001) along with the values of magnetic moments induced on each of the Cd and Ru atoms. The values in black (blue) indicate positive (negative) moments.*

DOS at the Fermi energy, the larger is the magnetic moment. We have plotted the total magnetic moment for the system (not per magnetic atom), versus the NSP density of states at the Fermi energy, for each configuration in Fig. 3.11. If the Stoner criterion holds true, then we should see a monotonic increase of moments as the DOS at the E_f increases. This is seen to hold in the case of all the Fe alloys (panel a), except for Fe-Pb alloys, and all Co alloys (panel b). A similar analysis could be done for local magnetic moments on atoms in overlayers calculated from the PDOS. The plot of local magnetic moments for the magnetic atoms as a function of the NSP-PDOS for that M is shown in the top panel of Fig. 3.12; while the induced moments on the non-magnetic atoms versus the NSP-PDOS for that N atom are plotted in the middle and bottom panels. In all of these plots, we observe that most of the plots are not according to our expectation based on Stoner's

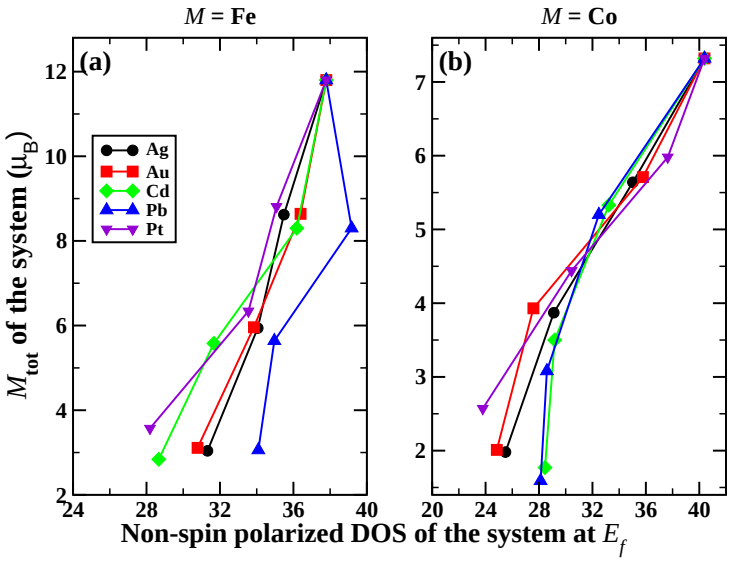

Figure 3.11: *Total magnetic moment, M_{tot} in μ_B as a function of non-spin-polarized DOS of the system at the Fermi energy, E_f. According to Stoner model, M_{tot} should increase with DOS at E_f. Note that, for the Fe-N alloys the behavior is as expected except for Pb alloy; for Co-N alloys, it is true for all alloys.*

criterion; also we see no general trend to correlate these two quantities. This suggests that the Stoner argument does not suffice to explain the magnetic properties of these surface alloys. The reason may be that the Stoner model is based on the rigid bond approximation which breaks down for a number of systems, as is known for transition metal impurities and compounds, and antiferromagnetic systems [121].

Another quantity of interest which might enable us to see the effect of the surface and alloying on individual atoms in the overlayer is the effective coordination number. In crystallography, the coordination number (CN) of any atom is defined as the number of nearest neighbors in the crystal structure. Even for atoms, not in periodic lattices, one can define an equivalent

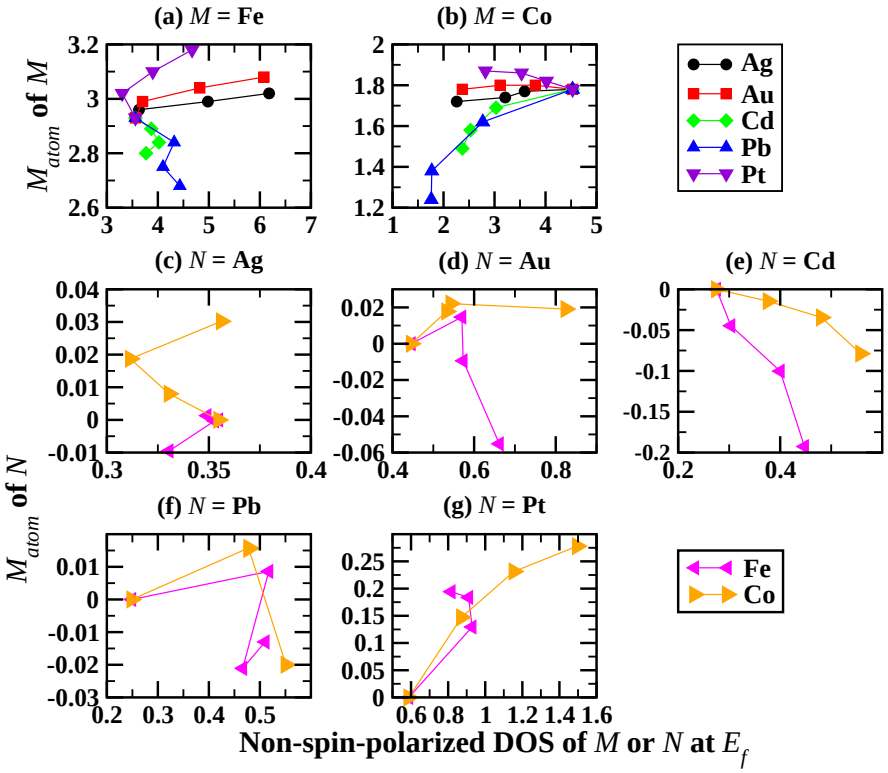

Figure 3.12: *Magnetic moment of an atom (A) in overlayer as a function of non-spin-polarized density of states at the Fermi level of A. (A = magnetic atom M in top panel and A = non-magnetic atom N in middle and bottom panels).*

measure, known as the effective coordination number (ECN) [122]; this can be done using the electronic density due to all the nearest neighbor atoms. The ECN for an atom A is defined as follows,

$$ECN(A) = \frac{\sum_{i=1}^{n} \rho(\mid \mathbf{r}_i \mid)}{\sum_{i=1}^{m} \rho_A(a)}, \tag{3.3}$$

where the sum is taken over all neighboring atoms i which are at a distance $\mid \mathbf{r}_i \mid$ from atom A, $\rho(\mid \mathbf{r}_i \mid)$ is the atomic charge density at a distance $\mid \mathbf{r}_i \mid$ from the nucleus of an isolated atom i and $\rho_A(a)$ is the atomic charge density

at a distance a from the nucleus of A. a and m are the NN spacing and the coordination number of atom A in the bulk. By this definition, for any atom in its bulk equilibrium structure, the effective coordination number will be equal to 1.0. The ECN is a measure of the electron density from surrounding atoms which is used extensively to determine local energetics in semiempirical approaches such as the embedded atom method [123, 124]. Atoms at the surface have a smaller coordination number than those in the bulk, and therefore will have ECN < 1. However, when a material is compressed then the ECN of its atoms would increase, which might be the case for N atoms in the overlayer. When the coordination number of an atom is reduced (either by changing crystal structure or by reducing the dimensionality from bulk to surface to isolated atom), the magnetic moment of the atom increases. This is in accordance with the Stoner criterion; the less the number of neighboring atoms, the sharper is the DOS at the Fermi level and the larger is the magnetic moment.

We have calculated the ECN for M and N atoms in the overlayer using the charge densities for isolated atoms. In Fig. 3.13, we have plotted the local magnetic moment of an atom M or N as a function of its effective coordination number. We observe that for all configurations, the ECN for M atoms is less than one on alloying, whereas for N atoms it is greater than 1. This implies that for N, the effect of compressing to smaller NN distances is more dominant than being at the surface. One can see that for Fe alloys (see Fig. 3.13a), the magnetic moments decrease as ECN increases as expected from Stoner's argument. but only some of the alloys of Co show this trend; and no definite trend can be inferred for induced moments on non-magnetic

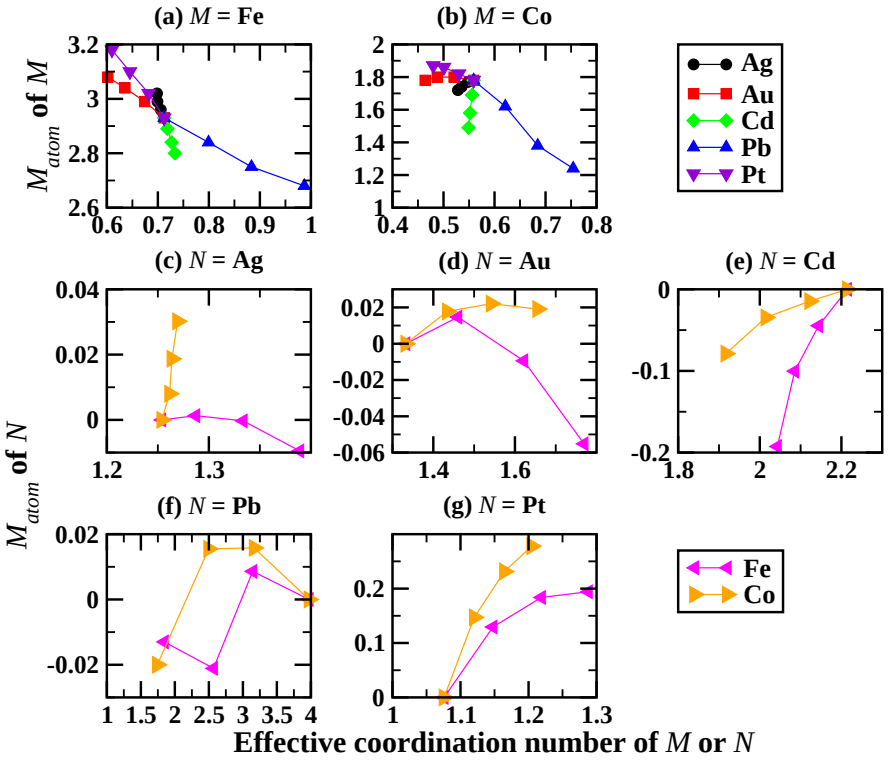

Figure 3.13: *Local magnetic moment of an atom A in the overlayer as a function of effective coordination number of A. (A = magnetic atom M in the top panel and A = non-magnetic atom N in middle and bottom panels).*

elements. This implies that the change in the coordination number cannot alone explain the observed trends for magnetic moments. Thus, we conclude that a complete understanding of the magnetic properties will require further analysis.

3.6.2 Calculation of Surface Lattice Constants

Now we will analyze in detail the miscibility trends for ΔH obtained for the surface alloys. As is described in the introduction, it is generally accepted

that there are two main contributions to the stability of such surface alloys: an elastic contribution and a chemical contribution. We would like to separate out the two contributions.

For homoepitaxial systems, the bulk truncated surface is usually under tensile stress [125], which can be released through relaxation and/or reconstruction. Therefore, the effective radius of the atoms at the surface is different from that of the bulk. For heteroepitaxial systems, there is atomic-size mismatch between the overlayer element and the substrate, which can lead to either compressive or tensile stress depending on whether the overlayer element has larger or smaller NN spacing than the substrate NN spacing. In the systems studied here, we are interested to see whether the mixing of two size-mismatched metals can lead to a stress release, and hence provide an additional mechanism for the stress release at the surface of a heteroepitaxial system.

To estimate the atomic radii of M or N atoms placed on the Ru(0001) surface, termed here as surface lattice constant (SLC), we have used two different approaches. The first approach is a very simple zeroth level approximation in which we assume a hard sphere model and estimate the SLC from the buckling of the alloy overlayer (explained previously in Sec. 3.5.4). Using relaxed structures at the $x = 0.50$ composition, we find the bond length $S-M$ $(S-N)$ and subtract from it the atomic radius of Ru (= Ru NN distance/2) which gives the atomic radius of $M(N)$. The values of SLC calculated using this method are given in Table 3.4 along with the corresponding bulk lattice constant. For Au, Ag and Cd, the effective atomic size at the surface is larger than that in the bulk and smaller for the remaining elements. However, if

Element	a_{bulk}^{calc} (Å)	a_{surf}^{strs} (Å)	a_{surf}^{buckl} (Å)
Fe	2.47	2.59	2.44
Co	2.49	2.36	2.42
Pt	2.83	2.79	2.74
Au	2.93	2.90	3.00
Ag	2.94	2.92	3.04
Cd	3.04	2.80	3.22
Pb	3.56	3.45	3.48

Table 3.4: *Comparison of surface lattice constants, a_{surf}, calculated from two different methods, with the NN spacing in the bulk.*

calculated at a different composition, then the SLC values differ from those reported here. Also these values are useful estimates, but will not enable us to separate out an elastic contribution for each configuration.

Therefore in the second method, we have used a simple understanding that the surface stress will be equal to zero if the surface atoms are at their preferred neighboring distance. To find this preferred distance, one would ideally like to compress/stretch the surface layer, while the substrate is fixed at its equilibrium distance, till the surface stress goes to zero. To achieve a small compression or expansion only in the overlayer, one needs a huge unit cell, e.g., to get 1% of expansion of the surface layer, one needs to have 100 atoms in the slab on which 99 overlayer atoms are put. This is computationally very expensive. The simpler way is to compress the whole slab with a pseudomorphic overlayer, and then subtract out the additional contribution coming from the stressed bulk slab to compute the surface stress [126]. We calculate the surface stress of an overlayer on Ru(0001) surface by subtracting the bulk stress due to the substrate from the slab stress. The expression

for surface stress (obtained by us) is given as follows,

$$\sigma^{surf} = \frac{1}{2}\left((\sigma_{xx}^{V,slab})L_z - (n_a - 2)\sigma_{xx}^{V,bulk}\frac{c}{2} + \sigma_{zz}^{V,bulk}\frac{l_{xy}^2}{3c}\right), \tag{3.4}$$

where, σ^{surf} is the surface stress at an in-plane NN bond length l_{xy} for a slab with n_a atomic layers and $\sigma_{\alpha\alpha}^{V,slab}$, and $\sigma_{\alpha\alpha}^{V,bulk}$ is the α-component of the "volume stress" of the slab and the bulk respectively at the same l_{xy}. The detailed derivation for this expression is given in Appendix A. This method of calculating the SLC is advantageous because one just needs to calculate the stress tensor at different in-plane lattice constants for both bulk and slab cells, and then subtract appropriate terms; there is also an error cancellation due to the subtraction. Using this method, we can also determine the parameters for the interaction potential between the overlayer atoms, as is shown further below. Previously used methods for the parametrization of surface interactions, included either using a jellium background [127] or fitting to the experimental data [128, 129].

Now we perform total energy calculations at different intraplanar bond lengths; the surface stress σ^{surf} as a function of l_{xy} is obtained for each single-component monolayer on Ru(0001). Note that for these calculations, we have used a symmetric slab, that is, the overlayer is deposited on both sides of the slab. As an example, our results for the variation of the surface stress with in-plane strain, for monolayer of Au and Cd on Ru(0001), are shown in Fig. 3.14; we obtain qualitatively similar curves for other elements (not shown here). The value of the SLC is given by the value of l_{xy} at which the graph cuts the x-axis. These values are tabulated in the second column

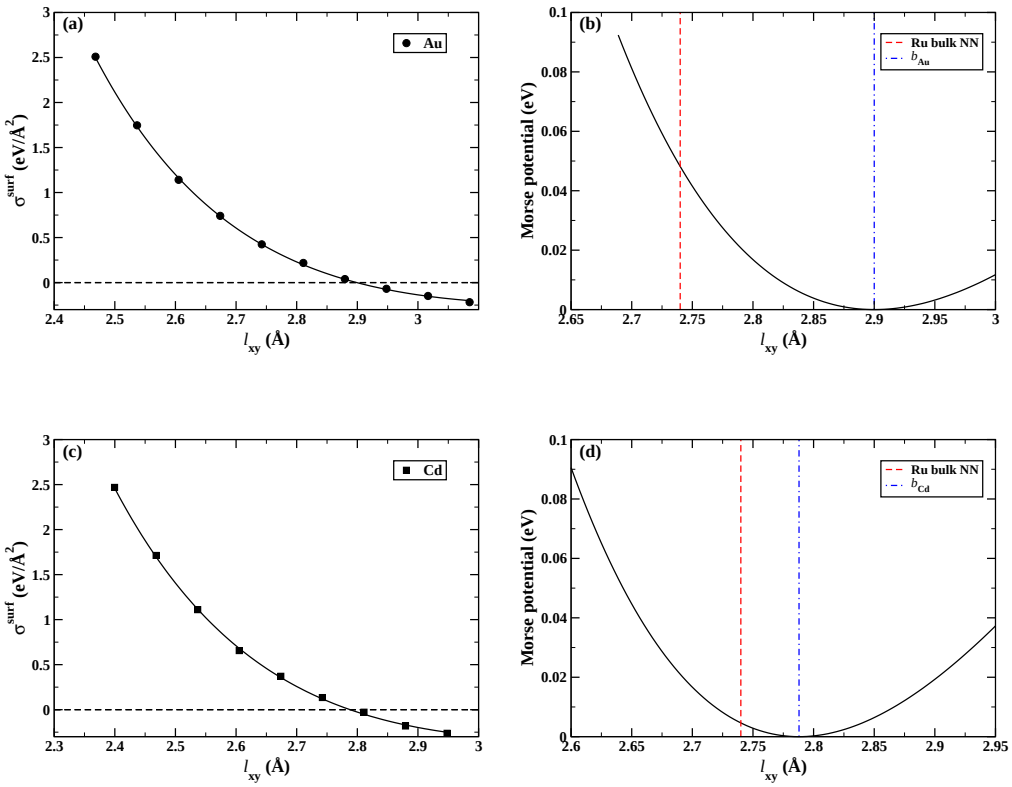

Figure 3.14: *Plot of surface stress σ^{surf} versus in-plane bond length l_{xy} for (a) Au/Ru(0001) and (c) Cd/Ru(0001): the dots represent the calculated values, whereas the solid line is a fit to data using an expression derived from the Morse potential. The Morse potential obtained from the fitted Morse parameters is shown for (b) Au and (d) Cd on Ru(0001). As expected, for Au and Cd, b is larger than the NN spacing of bulk Ru.*

of Table 3.4. Note that the values of SLC obtained from the two methods do not match.

It is also instructive to plot the surface stress for each single-component monolayer on Ru(00001) as a function of atomic-size mismatch, defined as $(a_{calc}^{bulk} - a_s)/a_s$; the plot is shown in Fig. 3.15. When a_{calc}^{bulk} is less than a_s, as in the case of M overlayers, one expects that the system will be under tensile stress, and vice-versa: when a_{calc}^{bulk} is greater than a_s, as for N overlayers, one

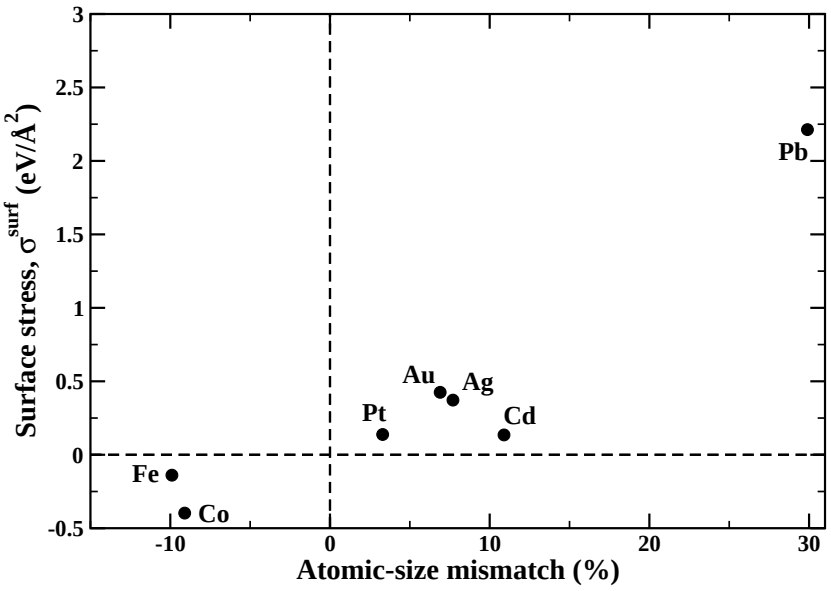

Figure 3.15: *Surface stress, σ^{surf}, for a single-component monolayer of M or N on Ru(0001), as a function of atomic-size mismatch, defined as $(a_{calc}^{bulk} - a_s)/a_s$. The positive (negative) surface stress indicates that that the overlayer is under compressive (tensile) stress.*

expects compressive surface stress for the system. We have observed that for all N/Ru(0001), the overlayer is under compressive stress, whereas both the magnetic overlayer systems – Fe and Co – are under tensile stress. These observations follow the trend expected from the atomic-size mismatch.

3.6.3 Elastic Model

We have used a model to separate out the elastic and chemical contributions to the formation energy. In this model, we have assumed that the elastic energy for each composition is given by the sum of individual bond energies.

We have assumed here that only the NN pairwise interactions are most dominant, and hence ignored further-neighbor terms. The elastic interaction for each NN bond has a typical form of potential, such as harmonic or Morse potential. The elastic energy is then written by counting the total number of bonds in the (2×2) surface unit cell. Initially, we started with a simpler harmonic potential as the approximation for NN bond potential. Then using the SLC values obtained using the surface stress method and force constants obtained by fitting σ_{surf} plots, one can separate the elastic contribution to ΔH. However, we observed that the harmonic bond approximation is not sufficient to explain many of the observed trends. Therefore, we then considered NN bonds to have a Morse potential form.

For the NN bonds, we assume that the elastic interactions have the following Morse potential form:

$$V_{ij}(r) = A_0^{ij}(1 - e^{-A_1^{ij}(r-b^{ij})})^2, \tag{3.5}$$

where r is the distance between the NN atoms i and j, b^{ij} is the equilibrium bond length, and A_0^{ij} and A_1^{ij} are the parameters associated with the depth and width of the potential well respectively. In the surface unit cell, there are three types of bonds: $M - N$, $M - M$ and $N - N$. By counting the number of bonds of each type, we can write the elastic contribution to ΔH

in terms of Morse parameters as follows,

$$\Delta H^{ela}_{x=0.25} = 6V_{MN}(a_s) - 3V_{MM}(a_s) - 3V_{NN}(a_s) \tag{3.6}$$

$$\Delta H^{ela}_{x=0.50} = 8V_{MN}(a_s) - 4V_{MM}(a_s) - 4V_{NN}(a_s) \tag{3.7}$$

$$\Delta H^{ela}_{x=0.75} = 6V_{MN}(a_s) - 3V_{MM}(a_s) - 3V_{NN}(a_s). \tag{3.8}$$

Note that Eqs. (3.6) and (3.8) are identical, that is, within our model, the elastic interactions lead to a ΔH^{ela} which is symmetric about $x = 0.50$. For bulk alloys of M and N, the second and third terms in the above equations will have zero contribution because these will be calculated at b^{MM} or b^{NN}, and not at the substrate NN spacing a_s. Thus these terms arise only due to the presence of the substrate. Consequently, the mixing rules for these types of surface alloys would be quite different from those applicable for bulk alloys.

To calculate ΔH^{ela}, we need values of the Morse parameters A_0, A_1 and b. To determine the Morse parameters, we have fitted the plots of σ^{surf} versus l_{xy} which were obtained as explained in Sec. 3.6.2. The plots are fitted with an expression derived from a Morse potential:

$$\sigma^{surf} = \frac{\sqrt{3}}{a_s}\frac{\partial V}{\partial r}, \tag{3.9}$$

i.e.,

$$\sigma^{surf} = \frac{\sqrt{3}}{a_s}\left(2A_0A_1\Big(1 - e^{-A_1(r-b)}\Big)e^{-A_1(r-b)}\right). \tag{3.10}$$

When this functional form is fitted for each of the elements M/N as shown in Fig. 3.14, we get Morse parameters for $i - i$ bonds which are tabulated in Table 3.5. The value of b^{ii} is a measure of the effective size of an atom i

M/N	A_0 (eV)	A_1 (Å^{-1})	b (Å)
Fe	0.1309	2.412	2.56
Co	0.5827	2.052	2.37
Pt	0.6744	1.817	2.79
Au	0.4341	1.797	2.90
Ag	0.3638	1.669	2.92
Cd	0.6564	1.680	2.79
Pb	0.2027	1.563	3.42

Table 3.5: *Morse parameters for $M-M$ and $N-N$ bonds: The values of Morse parameters are obtained by fitting σ^{surf} versus l_{xy} curve for each element.*

on the Ru(0001) substrate, which is termed as SLC in the previous section. Note that for all the nonmagnetic elements considered by us, b^{NN} is greater than a_s, whereas for Fe and Co, b^{MM} is smaller than a_s. Also we find that the values of b are different from a_{bulk}^{calc}. This difference results from the presence of the surface (i.e., no neighbors above) and the substrate (different neighbors below). Except for Fe/Ru(0001), for all elements, $b < a_{bulk}^{calc}$. For Fe, this probably results from the fact that in its bulk form Fe has the bcc structure with a coordination number of 8, whereas all other elements have either the fcc or hcp structures with a coordination number equal to 12. Therefore, when placed on the closed-packed Ru(0001) surface, only Fe atoms are more effectively coordinated than the rest of the overlayer elements. We do not find any simple correlation between the values of b and a_{bulk}^{calc}.

To get the corresponding parameters for $M-N$ bonds, we use mixing rules analogous to the Lorentz-Berthelot mixing rules [130]. The $M-N$ bonds are assumed to have the form $A_0^{MN} = \sqrt{A_0^{MM} A_0^{NN}}$, $A_1^{MN} = \sqrt{A_1^{MM} A_1^{NN}}$ and $b^{MN} = (b^{MM} + b^{NN})/2$. With these approximations, we have calculated the formation energies within this model. We have checked that the mixing rules

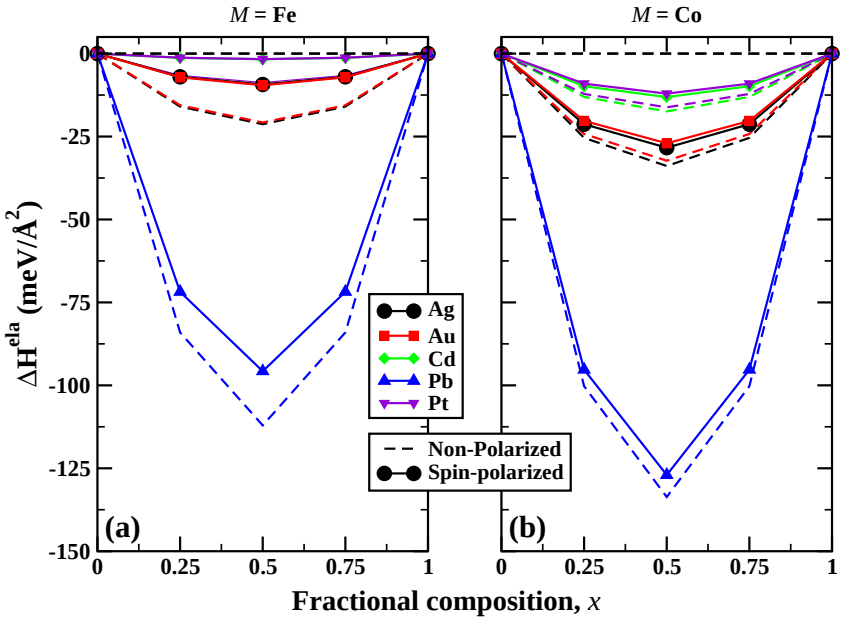

Figure 3.16: *The elastic contribution to the formation energy: ΔH^{ela} is plotted as a function of x, for (a) Fe and (b) Co, for both spin-polarized (solid lines) and non-spin-polarized (dashed lines) calculations.*

do not introduce considerable errors by comparing the surface stress values of the mixed alloy phases obtained by *ab initio* results with those calculated using the Lorentz-Berthelot mixing rules.

The results for the elastic contribution to the formation energy, calculated for spin-polarized cases, are shown in Fig. 3.16 with solid lines. For all pairs considered by us, elastic interactions always favor mixing of the two overlayer elements. which is in accordance with the predictions by Tersoff [74]. For both the magnetic elements, Pb alloys are the most stable, followed by Au and Ag alloys, whereas Pt and Cd alloys are the least stable. At first sight, this order is not expected based on the atomic-size mismatch given in Table 3.1.

However, unlike bulk alloys, for the surface alloys, the phase-segregated forms can cost a high elastic energy because of the substrate. Pseudomorphic Pb/Ru(0001) is under a high compressive stress and hence costs higher elastic energy, compared to which a mixed phase is strongly favored.

To make the above-mentioned statement clear, in Fig. 3.17, we have displayed the individual contributions to the right-hand side of Eq. (3.7). The first $(M-N)$ term is always positive, while the second $(M-M)$ and third $(N-N)$ terms are always negative. For ΔH^{ela} to be negative, the first term should be small, while the second and third terms should be large in magnitude. The first term is following the expectation from considerations of sizes for Fe-N and Co-N alloys: Ag and Au alloys are the most favored, followed by Pt and Cd, and then Pb. Note that both Cd and Pt alloys have roughly the same contributions from the first term even though in the bulk phase Cd atoms are much larger than Pt atoms; this is because Cd undergoes a relatively large contraction in size on the Ru(0001) surface, relative to the bulk. Elastic interactions favor the formation of Co-N alloys over Fe-N alloys because a Co monolayer on Ru(0001) has a significant contribution to the elastic part of the formation energy. Similarly a Pb monolayer on Ru(0001) is extremely unfavorable energetically, which leads to the high stability against phase-segregation of M-Pb alloys. However, recall that we have made the assumption that the alloys as well as phase-segregated monolayers remain pseudomorphic. For the alloys, this is probably a valid assumption, since the elastic energy is small, i.e., the stress is unlikely to be high enough to drive the overlayer to reconstruct, but, for single-component monolayers this may not be a valid assumption. Despite the significant elastic energy contained

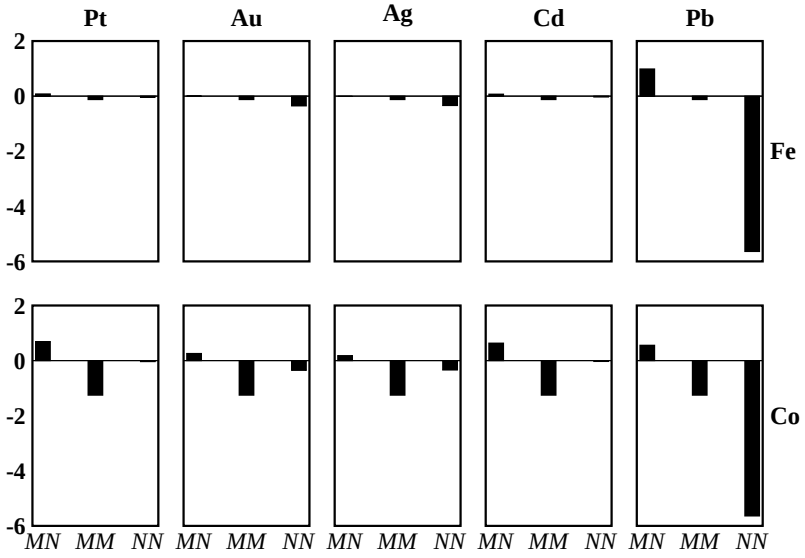

Figure 3.17: *The separate contributions from $M-N$, $M-M$ and $N-N$ bonds [from Eq. (3.7)] to ΔH^{ela} in units of $eV/Å^2$, for $x = 0.50$, for the spin polarized case are displayed. The top and bottom panels show the results for Fe and Co alloys respectively. For easier comparison, all the bar charts have been plotted on the same scale.*

in a Co/Ru(0001) monolayer, experimentally this system has been shown to grow pseudomorphically [131]. For Pb/Ru(0001), there is no experimental data describing its growth, however the very high elastic energy suggests that this system is very likely to reconstruct. Thus, the high stability we obtain for M-Pb alloys may be misleading; the stability would be lowered if the phase segregated form were to reconstruct since the third term in the elastic energy would then be decreased in magnitude. The study of possible surface reconstructions in these systems has also been done and we will discuss it in Chapter 6.

We now repeat our calculations for the elastic contribution to ΔH, for the NSP case. For this case, the values of b – the effective size on the surface – for Fe and Co, are 2.46 Å and 2.36 Å respectively. As expected, for both M, the NSP values of b are less than the SP ones (see Table 3.5). The percentage decrease is more for Fe ($\sim 4\%$) than for Co ($\sim 0.4\%$). The computed elastic contribution to the NSP ΔH is plotted in Fig. 3.16 (dashed lines). We observe that when only elastic effects are considered, spin polarization disfavors mixing for all alloys. On examining the separate contributions from $M-N$, $M-M$ and $N-N$ bonds, we find that the main reason for the reduced miscibility of SP configurations is that Fe and Co monolayers are relatively less stressed when spin polarized. The difference between the SP and NSP values is higher for Fe alloys than for Co alloys.

Finally, we have shown our results for the chemical contribution to the formation energy ΔH^{chem}, calculated for the spin-polarized case, in Fig. 3.18, with solid lines; these were obtained by subtracting out the elastic contribution (shown in Fig. 3.16) from the total formation energy computed *ab initio* (shown in Fig. 3.8). When only chemical contributions are considered, Co alloys are the least stable. The stability of Pt alloys is largely due to the favored M-Pt bonds, which accords with the formation of M-Pt alloys in the bulk. Also the Ag alloys are not stable, because Fe-Ag and Co-Ag bonds cost high chemical energy; this is in accordance with previous results [92,94]. Note that Fe-Au bonds favor mixing, while Co-Au bonds cost chemical energy, which explains the particular order of stability observed in our *ab initio* results.

Similarly we have plotted NSP-ΔH^{chem} in the same Fig. 3.18, with dashed

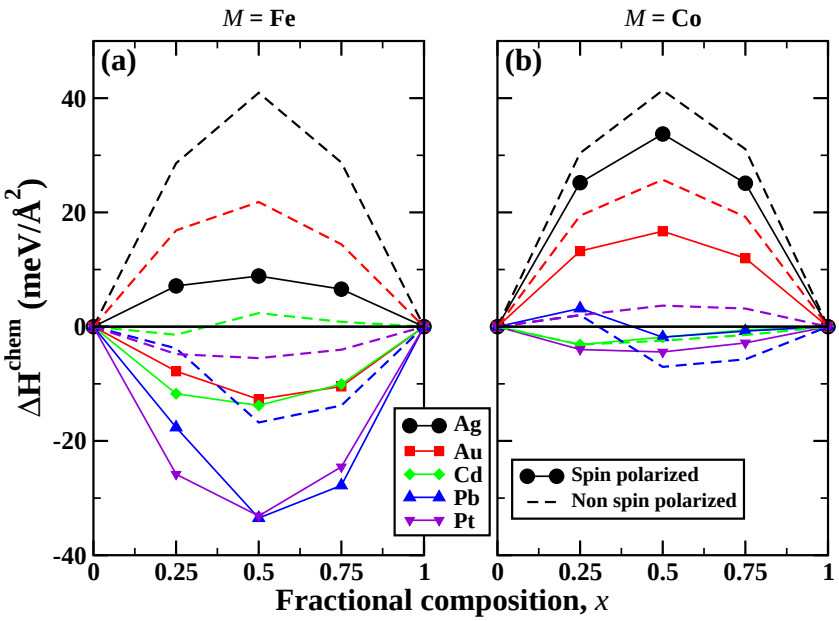

Figure 3.18: *The chemical contribution to the formation energy as a function of fractional composition, x, for (a) Fe and (b) Co surface alloys . The solid lines show results for spin polarized calculations and the dashed lines are for non-spin polarized calculations.*

lines. Note that in the absence of magnetism, the chemical interactions for Fe and Co are quite similar – this implies that magnetic moments alter the chemical interactions. The effect of magnetism is maximum in the case of Fe alloys. Spin polarization promotes mixing in all the cases except Co-Cd and Co-Pb alloys when chemical contribution terms are considered.

3.7 Summary and Conclusions

In this chapter, we have studied magnetic and structural properties of surface alloys of the type M_xN_{1-x}/Ru(0001) by performing density functional

theory calculations. We have separated out elastic contribution to understand the factors governing the energetics of these strain-stabilized alloys. For many pairs of metals, we find that the surface alloy is stable against phase-segregation, even though the constituent elements are immiscible in the bulk. We have also studied the magnetic properties of these alloys and observe that magnetic moments are enhanced for Fe and Co alloys as compared to bulk magnetic moments. The effect of magnetism on the miscibility is also studied. In general, mixing is promoted by the presence of magnetism.

We note that the general trends observed for these surface alloys are similar to those observed in the surface alloys on the Rh(111) surface [132, 133]. The NN distances for bulk Rh and Ru are almost identical (2.69 and 2.70 Å), and both the surfaces studied have a hexagonal unit cell which leads to similar values of ΔH on two substrates, however the magnetic moments are higher on the Rh(111) surface, owing to a larger paramagnetic DOS at the Fermi energy for bulk Rh than that of Ru.

The observed miscibility trends are not in accordance with a simple argument that the mean atomic size of the overlayer elements should be approximately equal to the substrate lattice spacing. From our analysis, we have observed that even though miscibility is mainly governed by the elastic interactions, chemical interactions also are important. In some cases, chemical interactions are more dominant leading to immiscibility, even if it costs elastic energy. Also for these strain-stabilized surface alloys, unlike for bulk alloys, the phase-segregated forms can cost elastic energy. Thus, there are three factors that determine possibility of mixing at the atomic level: (i) the elastic energy of the alloys, (ii) the elastic energies of the single-component

overlayers on the substrate, and (iii) chemical interactions. Additionally, all these factors can be affected by the presence of magnetism. Because of these interrelated factors, a simple criterion, analogous to the first Hume-Rothery rule for bulk alloys which is based only on the elastic energy of each constituent of an alloy, does not seem possible for such systems.

We have found that the effective size of M or N atoms on the Ru surface is not equal to their bulk size. Several pairs of M and N co-deposited on Ru(0001) surface favor atomically mixed alloy phases against the phase-segregated forms; this is primarily because the effective size of M atoms is smaller than the nearest-neighbor spacing of the substrate, while that of N atoms is larger. Of the total 10 systems which we have studied, we feel that Fe-Au, Fe-Cd and Co-Cd are promising candidates for experimental investigations. In these systems, both elastic and chemical interactions favor mixing. Though this is also true for Fe-Pt and Co-Pt alloys, these form alloys in their bulk phases. Also M-Pb alloys are found to strongly favor alloying, however our assumption of Pb forming a pseudomorphic layer on Ru(0001) may not be valid. For this reason, we do not believe that the Pb alloys are good candidates to observe atomic-level mixing.

Some of the results presented in this chapter were published by us in Ref. [132, 134].

Chapter 4

Ordered Surface Alloy of Bulk-Immiscible Fe and Au on Ru(0001)

4.1 Introduction

In the previous chapter, we had studied the formation of surface alloys from two bulk-immiscible metals on the Ru(0001) surface. After a detailed analysis of the energetics of these strain-stabilized surface alloys, we had predicted that a few of the pairs are promising candidates to observe atomic-level mixing at the surface [134]. Out of these predicted systems, we believe that Fe-Au/Ru(0001) is a perfect system to study surface alloying, because as shown in Chapter 3, both elastic and chemical interactions favor mixing for this system. Also because the effective sizes of Fe and Au atoms on the Ru(0001) surface are 2.56 and 2.90 Å respectively, therefore their average

value (= 2.73 Å) matches well with the nearest neighbor spacing of Ru (= 2.74 Å). Based on these theoretical predictions, our experimental collaborators – the group of S. Rousset, *et al.*, – have performed experiments on one of these systems, namely, $Fe_xAu_{(1-x)}$ on the Ru(0001) surface, where x is the Fe concentration. Both Fe(110) and Au(111) have smaller surface energies (= 0.98 and 0.61 eV/atom respectively) than Ru(0001) (= 1.57 eV/atom) [117] which makes it less likely that deposited atoms will diffuse into the Ru bulk.

In their bulk phases, Fe and Au are immiscible except at high temperatures, and at small concentrations. The phase separation can be clearly seen in the bulk phase diagram for the Fe-Au system shown in Fig. 4.1 [135]. However, there have been some reports which show that Au deposited on the Fe(001) surface forms a surface alloy for coverages below 0.5 ML [136]; this surface alloy was shown to have only a short-range order [137]. This kind of surface alloying leads to new ordered phases which were not observed before. A better understanding of these phases is essential because structural properties at the surface determine magnetic and transport properties.

There have been many reports on single-component Fe or Au layers deposited on the Ru(0001) surface. It has been observed in experiments that even at a single monolayer coverage, Au deposited on the Ru(0001) surface has a striped pattern of dislocations forming a herringbone pattern, and at higher coverages, it has a triangular pattern of dislocations [107]. This happens because a pseudomorphic layer would be under a large compressive stress, arising from the large atomic-size mismatch between Au and Ru. In contrast, Fe forms two-dimensional, pseudomorphic layers on the Ru(0001) surface till a critical thickness [104, 138]. For annealing temperatures > 800

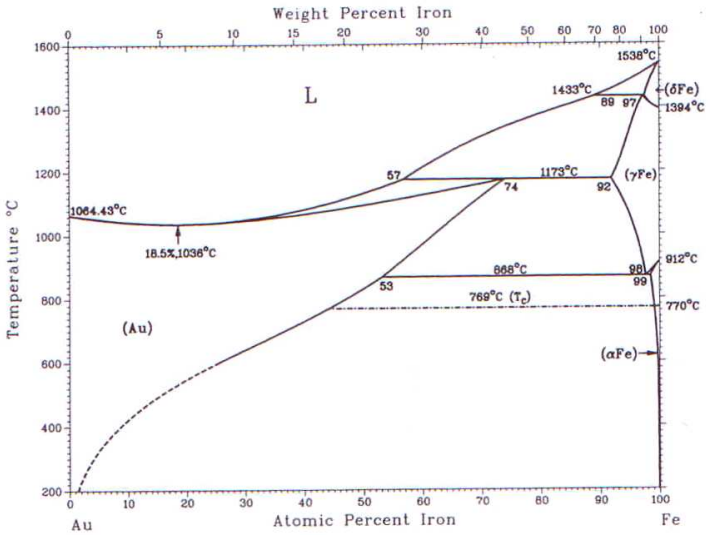

Figure 4.1: *Bulk phase diagram for the binary Fe-Au system is shown; it is taken from Ref. [135]. The strong tendency towards phase separation of the two elements can be clearly seen.*

K, Fe and Ru are observed to form an interfacial alloy [104]. The Fe/Ru(0001) system has been extensively studied for its magnetic properties because the Fe layer has a pseudo-hexagonal structure. The hexagonal closed packed phase of bulk iron is known to be stable at very high pressures [139,140], and extensive theoretical and experimental studies have observed the absence of magnetic ordering [141, 142] for this phase. In earlier experiments, the Fe/Ru(0001) system was found to have magnetic dead layers (i.e., no ferromagnetic ordering) up to 2 ML thickness [143] similar to the bulk hcp Fe; this was found to result from in-plane anti-ferromagnetic ordering by theoretical calculations [120,144]. Hardrat *et al.*, have also shown that as Fe layers have a triangular lattice, the AFM coupling leads to frustration giving rise to a more complicated spin ordering [120], which makes this system interesting to study.

When Fe and Au are co-deposited on Ru(0001), the structural properties are observed to change drastically. In experiments in the group of S. Rousset, this system shows a long-range ordered, atomically mixed pseudomorphic surface alloy at compositions where the Fe concentration is about 33%. These experiments are discussed in Section 4.2. In the present work, we have studied a large number of configurations for Fe-Au/Ru(0001), to understand various trends observed in the experiments. Note that in the work discussed in the previous chapter, we were interested in studying general trends which govern mixing properties of surface alloys, so we investigated a large number of pairs of metals but only for a few configurations, whereas now we are interested in studying one particular system at lots of different configurations. To analyze the effects of magnetism on mixing properties, we have also done non-spin polarized calculations for all the configurations. In addition, to see the effect of the presence of the substrate, we have performed calculations on free-standing monolayers of Fe-Au constrained to have the same geometry as that of the Ru(0001) surface, i.e., a triangular lattice at the NN spacing of the Ru(0001) surface.

4.2 Experimental Background

In this section, we have described experiments done on the Fe-Au/Ru(0001) system by our collaborators in the group of S. Rousset [145]. All the experiments were performed in an ultrahigh vacuum ($\sim 2 \times 10^{-10}$ mbar) where a Ru(0001) single crystal was cleaned by cycles of oxygen exposure at 1400 K

and then flashing at 1800 K. The purity of the sample was checked by performing Auger electron spectroscopy after each cycle till signals for carbon and oxygen impurities became vanishingly small; this was also confirmed by sharp diffraction spots in the low energy electron diffraction (LEED) pattern. The clean sample was observed to have large terraces ($\sim$ 200 nm wide) using scanning tunneling microscopy (STM). The alloy films were prepared by depositing one metal on the Ru single crystal and annealing the complete system, and then the same procedure was followed for the second metal. This two-step annealing is necessary to achieve larger and flatter islands, because the mobility of Fe and Au on the surface is kinetically limited, and one-step annealing after deposition of both the overlayer elements leads to smaller islands separated by patches of the bare Ru surface. The final configurations obtained did not depend on whether Fe or Au was deposited first, indicating that the equilibrium configuration has indeed been achieved. Au was deposited from an electron-beam heated Mo crucible at the rate of 0.04 ML/min, and Fe was deposited from an electron-beam heated Fe rod at the rate of 0.07 ML/min. All STM and LEED measurements were performed at room temperature.

Ru is nearly completely immiscible with both Au and Fe up to 600 K, and has a higher surface energy; therefore mixing between the overlayer and substrate is not favored. It was found that when only Au is deposited, the growth is in the layer-by-layer mode, with no diffusion into the substrate up to an annealing temperature of 750 K. On large islands of deposited gold, stacking fault lines and a herringbone-like shape were observed, in agreement with previous studies [107]. When only Fe was deposited on the

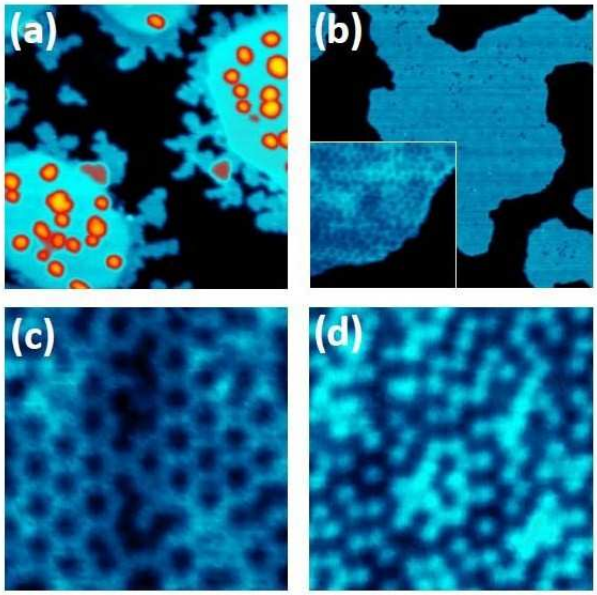

Figure 4.2: *STM images of FeAu/Ru(0001) at different compositions (figure courtesy S. Mehendale, et al.): (a) 50 × 50 nm^2 image after deposition of 0.40 ML of Au, annealed at 600 K and then followed by 0.36 ML of Fe at 300 K but not annealed. The image shows large circular islands consisting of Au atoms, and Fe atoms grow on top of these Au islands (brighter small islands) and along their perimeter (slightly darker dendritic shapes). (b) 50 × 50 nm^2 image of a 0.7 ML coverage of $Fe_{0.25}Au_{0.75}$ deposition, after annealing at 600 K. Inset shows a zoom of part of an island formed by overlayer metals, showing 7.9 × 7.9 nm^2 area. (c) An example for Au-rich phase showing 4 × 4 nm^2 area of 0.9 ML coverage of $Fe_{0.33}Au_{0.67}$ deposition, after annealing at 600 K, and (d) 4 × 4 nm^2 area of 0.7 ML coverage of $Fe_{0.55}Au_{0.45}$ deposition, after annealing at 600 K showing a representative Fe-rich phase. This figure has appeared in Ref. [146].*

surface, it grows pseudomorphically in accordance with previous results [104, 138]. There is no mixing between Fe and the substrate till the annealing temperature is higher than 700 K. As a result, the annealing temperature was restricted to 600 K for the experiments on surface alloys, so mixing between overlayer elements and Ru could be avoided; thus the substrate can be considered as only a periodic potential on which overlayer atoms sit. It was observed that the mobility had a temperature dependence, and hence also

the resultant structure – for annealing temperatures less than 500 K, both the Fe and Au atoms did not have sufficient mobility on the surface, thus the mixing mainly started at about 520 K and the phase equilibrium could be achieved only around 600 K. So there is a lower limit to the annealing temperature required.

In Fig. 4.2, STM images are shown for co-deposited Fe and Au on Ru(0001) at different concentrations. Fig. 4.2(a) shows a typical starting configuration of co-deposited 0.40 monolayer (ML) of Au and 0.36 ML of Fe before annealing. In this, Au forms large islands and Fe atoms either sit at the edges of islands (imaged slightly darker because of the size difference between the two metals) or form small islands on the Au islands. Fig. 4.2(b) shows a typical image observed after annealing at 600 K; it is obtained for a sample of 0.53 ML of Au and 0.17 ML of Fe. Note that there is a large variation in the morphology after annealing the sample. The annealed sample consists of homogeneous islands, with a slight contrast within the island due to alloying on the surface as shown in the inset. At the boundary of the island, the contrast has not changed, implying that segregation effects are negligible as compared to the enthalpy of mixing.

In Figs. 4.2(c) and (d), atomic resolution STM images are shown for Au-rich and Fe-rich phases respectively. For Au-rich phases – with Fe concentration of about 0.33 – a periodic structure having a long-range order is observed, except for some local defects. The long-range order (LRO) for these compositions is confirmed by a clear LEED diffraction pattern. However, for configurations having Fe concentrations x near 0.50, there is no LRO present, as shown in Fig. 4.2(d); only a short-range correlation between Au

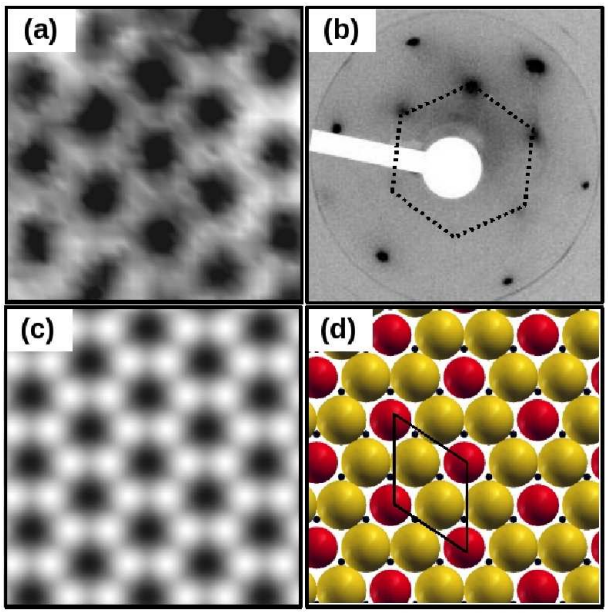

Figure 4.3: *A comparison of the experimental and the calculated results for* $(\sqrt{3}\times\sqrt{3})$ *structure of the* $Fe_{0.33}Au_{0.67}$ *alloy: (a) A high resolution 2.1×2.1* nm^2 *STM image of 0.9 ML coverage is shown, after annealing at 600 K. (b) The LEED pattern taken at 62 eV confirms the* $(\sqrt{3}\times\sqrt{3})$ *structure. Here the spots near the boundary correspond to the Ru(0001) surface and additional spots, which are rotated by 30° and located at* $1/\sqrt{3}$ *distance compared to Ru spots (connected by a hexagon) correspond to the* $(\sqrt{3}\times\sqrt{3})$ *unit cell. (c) Simulated constant height STM image taken at a height of 5.7 Å and a bias of 400 mV is shown to compare with the experimental STM image. (d) The atomistic model of the* $(\sqrt{3}\times\sqrt{3})$ *surface unit cell is shown. Black points show the positions of substrate atoms in the topmost layer, and red and yellow spheres represent Fe and Au atoms respectively.*

and Fe atoms is present, with some local order. For all other concentrations studied – Au-rich phases with $x < 0.33$, and Fe-rich phases – no LRO has been observed in STM images. Furthermore, for very high Au concentrations ($> 80\%$), it has been observed that, along with the alloy islands, clean Au islands are present, containing herringbone reconstruction lines [145]; for smaller Au concentrations, no reconstruction has been observed.

A high resolution STM image of 0.9 ML coverage of $Fe_{0.33}Au_{0.67}$ deposition is shown in Fig. 4.3(a); it shows a $(\sqrt{3}\times\sqrt{3})$ structure with perfect

order. In Fig. 4.3(b), the LEED pattern taken at 62 eV on a 0.7 ML of $Fe_{0.30}Au_{0.70}$ is shown and confirms the structure. The atomistic model for this structure is shown in the Fig. 4.3(d); this is the two-dimensional ordered phase with the smallest possible unit cell for $x = 0.33$ on a hexagonal lattice. We will discuss this in detail further below.

4.3 Computational Details

We have performed spin polarized *ab initio* density functional theory calculations using a plane-wave basis set along with ultrasoft pseudopotentials [18] as implemented in the Quantum-ESPRESSO package [29]. We have used a generalized gradient approximation of the Perdew-Burke-Ernzerhof form [11] for the exchange-correlation functional. All the parameters used for the following calculations are the same as those used in the previous chapter. The energy cut-off for wave functions is taken to be 20 Ry and the charge density cut-off is 160 Ry. We have used a supercell approach to model the surface within periodic boundary conditions. The supercell has a slab which consists of six Ru layers, one overlayer of Fe or Au or Fe-Au and a vacuum spacing of about 17.4 Å. The overlayer was deposited on only one side of the slab occupying the hcp sites, and is assumed to be pseudomorphic to the substrate. The overlayer and three adjacent Ru layers are allowed to relax using Hellmann-Feynman forces to get optimized geometries, whereas the three bottommost layers are kept fixed. We have used an (8×8) Monkhorst-Pack k-point grid [19] for the surface Brillouin zone of the smallest (1×1) unit cell for the triangular lattice; and for the larger unit cells, k-meshes proportional

to this are used. The Methfessel-Paxton smearing technique [22] is used with the smearing width equal to 0.05 Ry.

We have considered a total of 43 different configurations, which consist of all possible configurations [148] containing two, three, four, and five atoms per unit cell, and several containing six atoms per unit cell. The formula used to generate all these distinct unit cells is given in Appendix B, and a detailed description of each of the configurations studied is given in Appendix C.

4.4 Results and Discussion

We have first studied the mixing properties of all the alloy configurations by computing the formation energy ΔH as a function of Fe concentration x using Eq. (3.2) given in the previous chapter. The results for all the SP-configurations are plotted in Fig. 4.4(a). On the same figure, we have also plotted a convex hull (orange dashed line) which is defined as a set of straight lines connecting the lowest energy structures, forming a convex shape, such that all the remaining structures lie above the hull. The description of each configuration lying on the convex hull is tabulated in Table 4.1, and top views for a few selected configurations are shown in Fig. 4.3(d) and Fig. 4.5; for the remaining configurations one can refer to Appendix C.

For all the configurations considered here, we find that ΔH is negative, which indicates that mixing is favored even though Fe and Au do not mix in the bulk. We find that mixing tendencies are not symmetric about $x = 0.50$ concentration, with slightly higher $|\Delta H|$ for the Au-rich phases than the Fe-rich phases. The most stable structure is the $(\sqrt{3}\times\sqrt{3})$ structure at $x = 0.33$

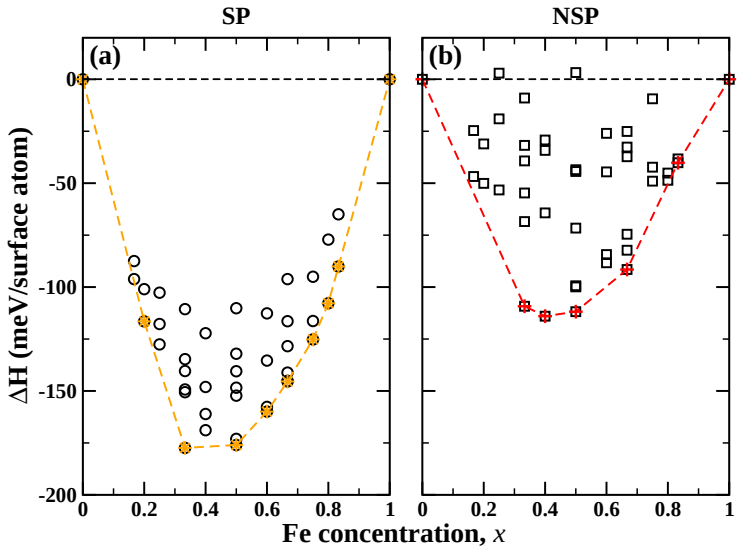

Figure 4.4: *Formation energy as a function of Fe concentration x from (a) spin-polarized and (b) non-spin polarized calculations: The convex hulls for SP and NSP calculations have been highlighted by orange stars and red plus signs respectively. For both panels, the same scale is used for easier comparison. Note that for a given configuration, the SP phase is always more favored than the corresponding NSP phase.*

(top view shown in Fig. 4.3(d)), which is the same phase as the one observed in the experiments to be the stable phase with LRO. In addition, at this composition, the difference in the ΔH values of the structure on the convex hull and the next stable structure is much larger than that for the other points on the convex hull; and also around this composition other phases have ΔH values which lie much above the convex hull unlike for other concentrations. These two observations together explain the observed LRO and the stability of this structure over a large range of compositions in the experiments. In contrast, at other values of x, there are several nearly degenerate phases lying close to the phase on the convex hull, higher in energy only by a few

meV per surface atom. For example, at $x = 0.5$, there is one more ordered alloy structure, separated by only 3 meV, near the structure on the convex hull. We have shown top views of these two configurations in Fig. 4.5(a) and (b). Note that, as was shown in Fig. 4.2(d), in the experiments, one can locally observe presence of these two phases around 50% composition which agrees well with the theoretically predicted structures. Recall that the DFT calculations are done at zero temperature, whereas the experiments are done at high temperatures. Thus such structures lying very near to the convex hull will compete in energy under experimental conditions. This explains the fact that, except near $x = 0.33$ concentration, no LRO was observed in the experiments. Furthermore, the convex hull passes through only two structures in the Au-rich region, but through five structures in the Fe-rich region. Thus for the Fe-rich phases, there are many competing phases at and around each x which will also lead to a lack of ordering at longer length scales. All of this demonstrates a remarkable agreement between the experiments and our calculations.

To further compare with the experiments, we have simulated a constant height STM image for the $Fe_{0.33}Au_{0.67}$ alloy having $(\sqrt{3} \times \sqrt{3})$ structure, which is shown in Fig. 4.3(c). The simulation is done at a bias of 400 mV and a height of 5.7 Å. From the simulated STM image, we observe that Fe atoms are imaged darker than Au atoms, in agreement with the experiments. Though in the experiments, constant current image is recorded, there is a good agreement between the experimental STM image, shown in Fig. 4.3(a), and the simulated image. This strongly supports the observed structure of the alloy.

x	Deposited SP phases	Deposited NSP phases	FSM-SP phases
0.167	-	-	-
0.20	$(\sqrt{7} \times \sqrt{3})$ Fig. C.2b	-	-
0.25	-	-	(2×2) Fig. C.3b
0.333	$(\sqrt{3} \times \sqrt{3})$ Fig. C.4b	$(6 \times 1)_1$ Fig. C.4e	-
0.40	-	$(5 \times 1)_1$ Fig. C.5a	-
0.50	$(2 \times \sqrt{3})$ Fig. C.6c	(4×1) Fig. C.6b	(2×1) Fig. C.6a
0.60	$(\sqrt{7} \times \sqrt{3})_2$ Fig. C.5d	-	-
0.667	$(\sqrt{3} \times \sqrt{3})$ Fig. C.4b	$(2\sqrt{3} \times \sqrt{3})_2$ Fig. C.4d	-
0.75	$(2 \times \sqrt{3})$ Fig. C.3c	-	(2×2) Fig. C.3b
0.80	$(\sqrt{7} \times \sqrt{3})$ Fig. C.2b	-	-
0.833	$(2\sqrt{3} \times \sqrt{3})$ Fig. C.1b	$(2\sqrt{3} \times \sqrt{3})$ Fig. C.1b	-

Table 4.1: *List of configurations which fall on the convex hulls for deposited SP, deposited NSP and FSM-SP calculations at each x: To see each alloy configuration, refer to the schematic top views of each unit cell given in Appendix C; here we have also given the corresponding figure labels.*

Upon a further examination of the energetics of the various configurations considered by us, we find that for a given x, the lowest energy structure is almost always the one that maximizes the number of heteroatomic pairs and triplets, that is, structures having isolated Fe or Au atoms surrounded by atoms of the other species are preferred. This implies an inclination towards atomic-level mixing. We will return to this point again in the further discussion below.

Next, we have performed non-spin polarized calculations (to suppress magnetism). In Fig. 4.4(b), we have plotted NSP-ΔH along with the convex hull obtained for the NSP phases (shown with red dashed line). For each configuration, the SP alloy is more favored then the NSP alloy. The miscibility is reduced considerably in the absence of magnetism which indicates

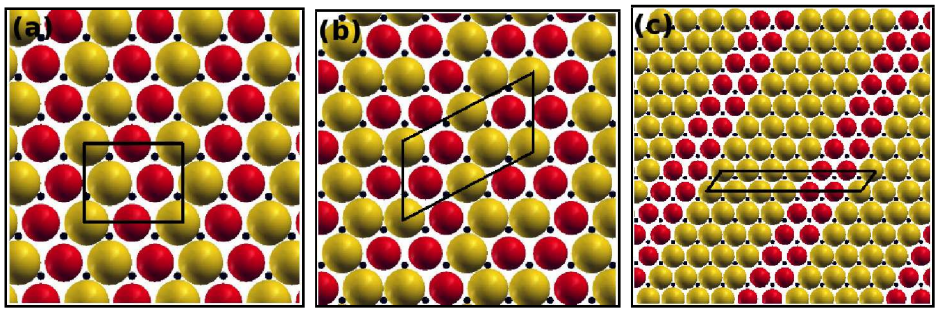

Figure 4.5: *Top views of (a)* $(2 \times \sqrt{3})$ *and (b)* $(2\sqrt{3} \times \sqrt{3})$ *structures for* x *= 0.50. Black points indicate positions of top Ru layer and red (yellow) spheres show Fe (Au) atom positions in the overlayer. The surface unit cell is shown with black lines. The first structure lies on the SP convex hull, however the second one is separated by only 3 meV per surface atom in energy from the previous one; therefore both these structures are likely to be observed in the experiments. In (c), we have shown a top view of* (6×1) *structure which is found to be the most stable structure at* $x = 0.33$ *in NSP calculations.*

the importance of magnetism in determining the stability of surface alloy phases. Also, the order of stability for structures is different for SP and NSP calculations. We note that fewer phases lie on the NSP convex hull as compared to the SP convex hull, and also as tabulated in Table 4.1, the actual structures lying on the convex hull differ from those on the SP curve. If we compare the structures on the two convex hulls, then we note that for the NSP calculations the striped structures are more favored indicating a slightly greater tendency towards phase segregation which is in contrast to the SP phases. For example, at $x = 0.33$, the most stable structure has a (6×1) unit cell (shown in Fig. 4.5(c)) which differs markedly from the $(\sqrt{3} \times \sqrt{3})$ structure favored in the case of the SP phases.

For these types of surface alloys, surface stress reduction was hitherto believed to be the driving force for the mixing of overlayer metals. To examine the validity of this assumption, for all the configurations under study, we have

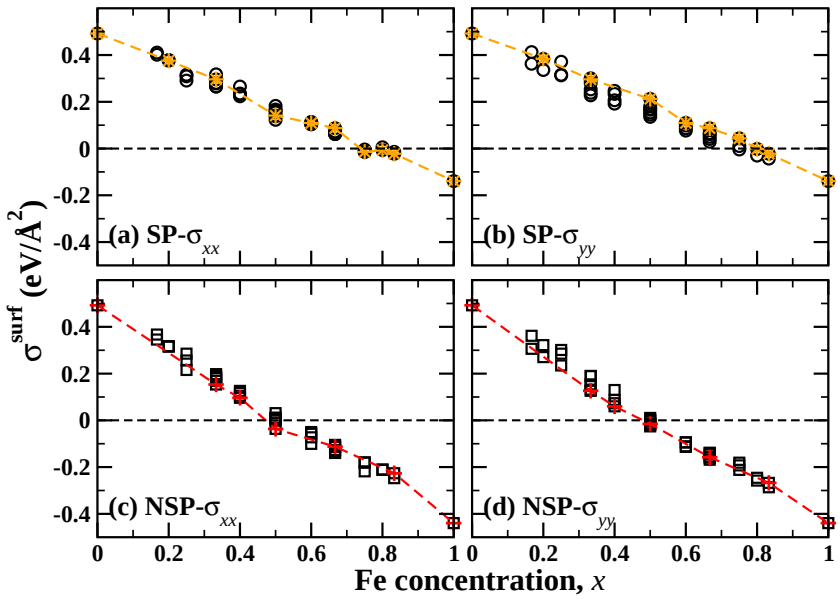

Figure 4.6: *Surface stress as a function of x for all the configurations under study: Top (bottom) panel shows results for SP (NSP) phases. The xx and yy components are plotted in left and right panels respectively. The same scale has been used for all the panels. On each panel, stress values corresponding to the structures on the convex hulls are highlighted by orange stars (for SP) or by red plus signs (for NSP). Note that for SP, σ^{surf} goes to zero at $x \sim 0.8$ indicating Fe-rich phase are more favored, however for NSP, it goes to zero at $x \sim 0.5$.*

computed the surface stress σ^{surf} as a function of x; the expression used to calculate the surface stress components has been derived in Appendix A. Note that the surface stress equation was derived for a symmetric slab, that is, a slab having an overlayer on each side, however in these calculations we have considered an asymmetric slab. Therefore one needs to subtract the stress coming from the unrelaxed Ru surface, that is, from the other side of the slab which is not allowed to relax. The surface stress of the overlayer

$\sigma^{surf}_{overlay}$ can then be written as:

$$\sigma^{surf}_{overlay} = \sigma^{surf} - \sigma^{surf}_{unrel}, \tag{4.1}$$

where σ^{surf} is the surface stress which is derived in Appendix A, σ^{surf}_{unrel} is the surface stress for the ideal, bulk-truncated Ru(0001) surface which is equal to -0.405 eV/Å^2. We now use this modified equation to compute the surface stress for these systems.

The xx and yy components of the surface stress for the SP phases are plotted in Fig. 4.6(a) and (b) respectively. On each of these plots, the points corresponding to the configurations on the convex hull (given in Fig. 4.4(a)) are highlighted by orange stars. Note that the stress is reduced on mixing, having higher magnitudes for both Fe ($x = 1.0$) and Au ($x = 0.0$) single-component monolayers. As x increases, the stress varies from compressive to tensile values, following an almost linear trend. The stress is observed to be asymmetric around $x \sim 0.5$ which results from anharmonic interatomic potentials and the differing interatomic force constants for Fe and Au. Considering only elastic terms, one would expect that Fe-rich alloy phases should be favored over Au-rich phases, because both the surface stress components go to zero at $x \sim 0.8$. However, as demonstrated above, we have found that Au-rich phases are more favored. Also at a given composition, the most stable structure does not correspond to the lowest surface stress at that composition, as can be seen from the position of the highlighted convex hull structures. From these observations, we conclude that for this particular system, stress reduction is not the dominant factor governing the mixing of

overlayer metals.

Next, we see how the surface stress is affected when magnetism is absent. We have plotted the xx and yy components of σ^{surf} obtained for NSP phases in Fig. 4.6(c) and (d) respectively. On these plots, the structures corresponding to the NSP convex hull are highlighted by red plus signs. Note that the single-component Fe/Ru(0001) layer is less stressed when magnetic; this point was discussed in the previous chapter. The overall trends such as reduction on mixing and linear variation with x are still present for NSP calculations, however the main difference is that the stress goes to zero at $x \sim 0.5$ implying that the NSP-ΔH should be more or less symmetric about $x = 0.5$. Unlike the SP-σ^{surf}, the lowest surface stress at a given x, in general, corresponds to the lowest energy structure at that x. This implies that, in the absence of magnetism, the surface stress becomes the dominant factor which governs the mixing.

In Fig. 4.7, we have plotted magnetic moments per Fe atom, as a function of x, for all the configurations considered by us. In general, the values of magnetic moments decrease as the Fe concentration increases. The structures lying on the convex hull for the SP-ΔH are shown with orange stars. Our most striking result is that we observe that the lowest energy structure is always the one with the highest magnetic moment per Fe atom. This is in accordance with our observation that the structures with "isolated" Fe atoms have lower ΔH. This underlines the importance of magnetism in stabilizing the mixed phases, which was earlier demonstrated by reduction of mixing on switching off magnetism. In our case, magnetism not only increases the mixing, but also tilts the balance towards Au-rich phases, implying that the

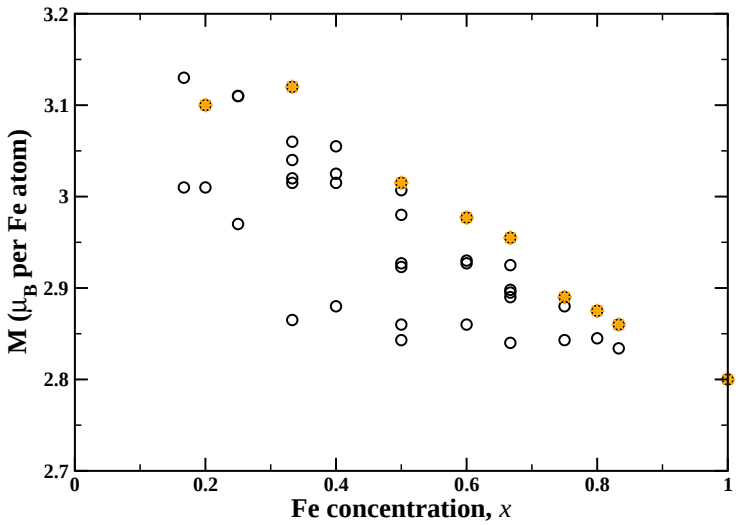

Figure 4.7: *Magnetic moment per Fe atom as a function of x for all the configurations: We have highlighted those structures which lie on the convex hull by orange stars. For each x, we see that the highest magnetic moment corresponds to the lowest energy structure.*

exchange interactions are more dominant than the elastic interactions for this system. Similar ideas have been previously discussed by S. Blügel for the binary alloy of Mn/Cu(001) [98].

4.4.1 Free-standing Monolayers

Now we discuss briefly the results for free-standing monolayers (FSM) of $Fe_xAu_{(1-x)}$ layers, which are constrained to have the same geometry as that of the Ru(0001) surface, but placed in vacuum. In this case, the layers are not allowed to relax geometrically because in the x-y plane, we want to confine the free-standing monolayers to the Ru(0001) surface lattice constant, and in the z direction, for some example systems, we did not observe any

relaxation. Even though such free-standing layers are not feasible in actual experiments, examining their properties allows us to separate out the effect of dimensionality (confining the Fe-Au layer to two-dimensions) from the substrate effects (interaction of Fe-Au layer mediated via Ru layers).

The main results for FSM configurations are summarized in Fig. 4.8. In Fig. 4.8(a), we have plotted the formation energy as a function of x. For all the configurations, ΔH is negative implying that the mixing is favored even for free-standing Fe-Au monolayers. This is in contrast to the three-dimensional Fe-Au phases which do not form alloys over the entire concentration range. Comparing the plot with the results from deposited monolayers in Fig. 4.4(a), we see that the values of ΔH are in the same range for both the cases, which implies that the mixing is more affected by confined dimensions than the presence of the substrate. However, there are fewer structures on the convex hull and the structures on the hull differ from those observed for deposited monolayers, as seen from Table 4.1. Thus the presence of the substrate influences the relative stability of various phases, but not the presence or absence of mixing itself.

Next, we have calculated the components of surface stress for the FSM phases. Note that in this case, there is no contribution from the substrate, so σ^{surf} is given by the "volume stress" multiplied by the length of the supercell along the [0001] direction. The xx and yy components of σ^{surf} are plotted in Figs. 4.8(b) and (c) respectively. Except for a pure Au monolayer, all the phases are under tensile stress. This can be understood in terms of reduced coordination of each atom which will tend to decrease the NN spacing of the FSM phases. For the Au monolayer, even though coordination is reduced, it

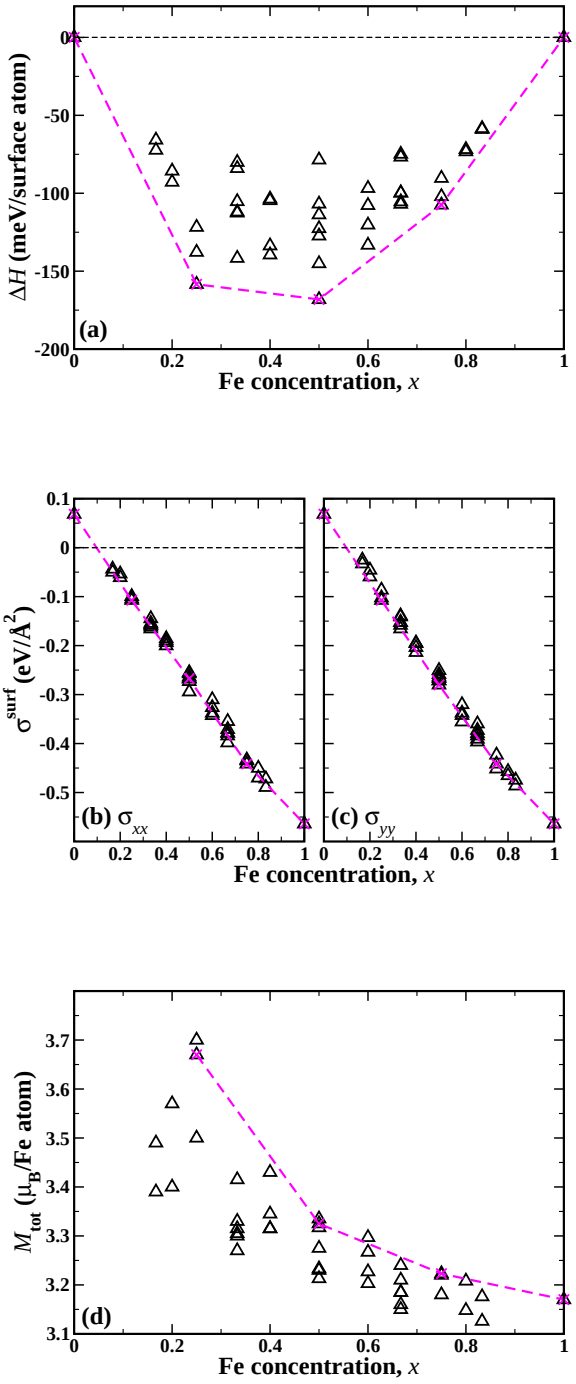

Figure 4.8: *Results for (a) the formation energy, (b) xx and (c) yy components of the surface stress and (d) the magnetic moments as a function of the Fe concentration x for SP calculations of free-standing monolayers: The convex hull structures are shown with magenta crosses. The overall trends observed for these phases are similar to the trends observed for the deposited monolayers.*

has been compressed to Ru NN distance which will lead to compressive stress. For the Fe layer, the value of surface stress has increased compared to that in the deposited monolayer case, whereas for Au, it has decreased. The reason is that Fe/Ru(0001) is already under tensile stress which increases on reduced coordination, but the Au/Ru(0001) system was under compressive stress, the tendency towards which is opposed on reduced coordination. For the free-standing monolayers, we have not observed any correspondence between the lowest energy structure and a lower stress at a given x.

Finally in Fig. 4.8(d), we have plotted the magnetic moments for all the configurations under study as a function of x. The overall trends are the same as for the deposited monolayers (see Fig. 4.7). However the values of moments are higher for FSM phases which results from the narrowing of d bands for the reduced coordination number. There is no correlation between structures with highest magnetic moments and the structures with lowest energies as was observed for deposited case. This underlines the importance of the presence of the substrate to meditate exchange interactions which leads to atomic-level mixing.

4.5 Summary and Conclusions

In this chapter, we have studied two-dimensional surface alloys of the form $Fe_xAu_{(1-x)}$ on the Ru(0001) surface, using *ab initio* calculations. We compare our results with experimental results obtained on this system using STM and LEED techniques. Even though Fe and Au are largely immiscible in the bulk phase, we have found that they form commensurate alloyed phases on

Ru(0001). We have calculated the formation energy for a large number of configurations and found that the most stable structure occurs at $x = 0.33$, with a $(\sqrt{3} \times \sqrt{3})$ structure. The same structure is observed in the experiments, having a long-range ordering, over a range of Au-rich compositions. We have calculated the surface stress and the magnetic moments for all the configurations under study. We have also performed non-spin polarized calculations on all the configurations to separate out the effects of magnetism. From comparison of the SP and NSP results, we conclude that on alloying the surface stress is reduced which favors the atomic-level mixing, however the relative stability of various phases is primarily decided by the exchange interaction. From a closer examination of the structures on the convex hull for this system, we were able to explain several trends observed in the experiments.

We have also done calculations for free-standing monolayers of $Fe_xAu_{(1-x)}$ constrained to have the geometry of the Ru(0001) surface. By comparing the results for FSM and deposited monolayers, we have concluded that the mixing is more affected by the dimensionality than the substrate, but the relative stability of individual phases at a given concentration depends largely on the presence of the substrate.

Note that for the calculations in this chapter, we have made two assumptions: the first is that the pure Fe and Au monolayers, and all the alloy overlayers are taken to be pseudomorphic to the substrate. For the Fe layer, this is known to be a correct assumption [104, 138, 147]. For alloy layers, the assumption may or may not be valid; however in the previous chapter, we have shown that the elastic contribution from Fe-Au bonds is

small (refer to Fig. 3.17 and the corresponding discussion), and therefore we believe the likelihood of reconstruction is low. For the Au layer, this assumption is known to be incorrect [107,147]; however our calculations, using the Frenkel-Kontorova model, have shown that the energy difference between reconstructed and unreconstructed surfaces is not more than a few meV per atom (see Chapter 6) [147]. The second assumption is to consider only the ferromagnetic configuration for the pure Fe layer on Ru(0001), which, however, has been theoretically shown to have non-collinear Néel state [120,144]. However, we believe these two assumptions might change the actual numerical values of various quantities, but not the observed trends or qualitative behavior.

Some of the results presented in this chapter have been published by us in Ref. [146].

Chapter 5

Effect of Substrate on the Stability of Surface Alloys: Fe_xAu_{1-x}/Mo(110)

5.1 Introduction

In the previous chapter, we have shown that a single layer of co-deposited Fe and Au forms a long-range ordered surface alloy on the Ru(0001) surface [146]. Here we would like to investigate how a change in geometry and substrate will affect the structural properties of a Fe-Au monolayer, so we have replaced Ru(0001) by the Mo(110) surface. The NN spacing values of Ru (= 2.70 Å) and Mo (= 2.73 Å) differ by about only 1%. However, the anisotropy of the Mo(110) surface might play a dominant role in determining the relative stability of various configurations. This surface was chosen because it has been studied extensively, and techniques to prepare a clean

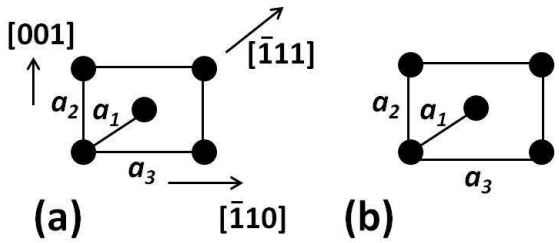

Figure 5.1: *Schematic diagram for the unit cell of (a) centered-rectangular bcc(110) surface (b) hexagonal fcc(111) surface: In (a), the centered-rectangular unit cell for the bcc(110) surface with different crystallographic directions is shown. a_i's are the distances along the various crystallographic directions; a_1 is the NN distance. In (a), $a_1 \neq a_2 \neq a_3$, but as shown in (b), for the fcc(111) surface, $a_1 = a_2 \neq a_3$.*

surface are known [149]. Similar to the case of Ru discussed in the previous chapter, the Mo(110) surface has a higher surface energy (= 1.5 eV/atom) than the Au(111) and Fe(110) surfaces (= 0.61 and 0.98 eV/atom) [117]. Further the solubility of Fe and Au in bulk Mo is very limited. These two facts indicate that diffusion of atoms of either of the overlayer species into the substrate, or alloying with the substrate, should be restricted.

The substrate molybdenum has a body-centered cubic (bcc) structure in the bulk. We are considering the (110) surface of Mo which has a centered-rectangular unit cell (schematic diagram shown in Fig. 5.1a). This surface is anisotropic along different directions, unlike the Ru(0001) surface. This implies that the atomic-size mismatch criterion which was used to estimate strain reduction should be modified to account for this. Therefore we have compared the most stable surface for each overlayer element, i.e., Fe(110) and Au(111), with the Mo(110) surface [83]. The Fe(110) surface has the same geometry (with different lattice constants) as that of the Mo(110) surface as shown in Fig. 5.1(a), and the geometry of Au(111) is shown schematically

Crystal directions	Size mismatch	
	Fe	Au
$[\bar{1}11]$ (NN direction)	-9.2	5.3
[001] (along y-axis)	-9.2	-9.0
$[\bar{1}10]$ (along x-axis)	-9.2	11.6

Table 5.1: *Atomic-size mismatch (in %) of Fe and Au with Mo, calculated by considering the anisotropy of the (110) surface: The values for bond lengths used to calculate the mismatch are experimental values taken from Ref. [103].*

in Fig. 5.1(b). The mismatch values are tabulated in Table 5.1, calculated for different crystallographic directions. For the Fe layer, the stress along different directions is identical (~ -9.0 %), owing to the fact that both the surfaces have the same geometry. However for Au, both the value and the sign of the mismatch are different along different directions. Along the [001] direction, both Fe and Au layers would be under tensile stress. Along the other two directions, the Fe layer would be under tensile stress, whereas the Au layer would be compressed, and thus along these two directions strain reduction by mixing may be expected. These mismatch values could be used as indicators to gauge whether the surface stress should be compressive or tensile along different directions.

5.2 Previous Work

A lot of work has been done to study the properties of a single-component Au or Fe monolayer deposited on the Mo(110) surface. For the Au/Mo(110) system, the growth process is temperature-dependent and the mobility of deposited atoms is limited at room temperature. For a monolayer coverage, near room temperature, there is two-dimensional layer formation (Frank–van

der Merwe growth mode), however there is no long-range order; but at high temperatures, the layer relaxes to form large islands [150, 151]. At higher coverages, the growth mode changes from Frank–van der Merwe to Stranski–Krastanov growth mode [152]. The growth is not pseudomorphic even at low coverages. No alloying with the substrate has been observed for this system.

The growth of iron on the Mo(110) surface proceeds in a number of steps depending on deposition temperatures and growth rates. Using STM and LEED measurements, pseudomorphic growth in the Frank–van der Merwe mode has been observed at room temperature, which is followed by Stranski–Krastanov mode at intermediate temperatures and alloying at high temperatures (> 600 K) [153,154]. However, there is no alloying until deposition of a single monolayer is complete, even at very high temperatures. At higher coverages, there is formation of dislocation lines to reduce the stress, but misfit dislocations are not observed for a single monolayer [154,155]. Previous calculations have shown that for Fe/Mo(110), there are magnetic moments induced on the adjacent Mo layers with antiferromagnetic (AFM) coupling [156]. Also, it has been shown that there is a strong magnetic anisotropy for 1 ML Fe on Mo(110), with in-plane easy axis along the $[1\bar{1}0]$ direction [157]. However some experimental studies observed the in-plane easy axis of magnetization pointing along the [001] direction [158]. Notably Fe nanoislands and nanowires have shown perpendicular magnetization [159–161] in contrast to thin layers. So it will be interesting to study how the magnetic properties will be affected when Fe forms an alloy with a non-magnetic element such as gold.

There have also been some reports which study Fe-Au nanostructures on

the Mo(110) surface [162, 163]. In these studies, the authors have shown that at room temperature, Au deposited on the pre-deposited Fe nanostripes on Mo(110) forms islands elongated along the [001] direction; this indicates anisotropic diffusion on the surface, unlike that on the pure Mo(110) surface. However, on annealing the sample, the formation of homogeneous FeAu alloy nanoislands was observed, along with a few double-layer islands consisting of a Fe layer covered by Au atoms. No superstructure or long-range order was observed for the alloy layer. As the coverage of Au increases, spin reorientation has been observed, from the out-of-plane magnetization of the pure Fe nanostripes on Mo(110), to in-plane magnetization [163]. These studies have given us an additional motivation to understand why there is no long-range order for FeAu/Mo(110) in contrast to FeAu/Ru(0001).

There have also been some studies of surface alloying on the Mo(110) surface by the co-deposition of two metals. For example, thin films of Fe-Ag and Co-Ag deposited on the Mo(110) surface have been characterized by STM and LEED measurements by Tober, *et al.*, [83]. In this study, the authors have observed an ordered alloy having a striped pattern with alternating rows of Fe (or Co) and Ag; these rows coincide with the [001] direction of the surface. The formation of the striped structures was explained by the stress reduction along that direction. Further theoretical investigations have also confirmed the striped structure as the most stable phase for Fe-Ag/Mo(110) [84]. These reports are relevant to our study because Ag and Au have similar sizes in their bulk phases and hence we may expect similar behavior, if elastic effects dominate. Recall that in Chapter 3, we have found that the elastic interactions for Fe-Ag/Ru(0001) and Fe-Au/Ru(0001) are

almost equal, but chemical interactions differ, and hence lead to different mixing properties. Therefore, it would be interesting to see whether various properties differ for Fe-Au/Mo(110) from those observed for Fe-Ag/Mo(110).

5.3 Computational Details

The calculations are done using spin-polarized density functional theory with a plane-wave basis set as implemented in the PWscf package of the Quantum-ESPRESSO code [29]. The kinetic-energy and charge density cut-off values are taken to be 25 and 200 Ry respectively, following rigorous convergence tests. We have used ultrasoft pseudopotentials [18]. For the exchange-correlation functional, we have used a generalized-gradient approximation of the Perdew-Wang form [12]. Brillouin zone sampling was performed using a (17×17) Monkhorst-Pack k-point grid [19] for the smallest (1×1) surface unit cell of the substrate. The system being metallic, we have used the Methefessel-Paxton smearing technique [22] with a smearing width of 0.05 Ry.

To study surface properties within periodic boundary conditions, we have used a supercell approach. The coordinate system used for constructing the supercell is such that that the surface normal, i.e., the [110] direction, is along the z-axis, and the x and y-axes are along the $[\bar{1}10]$ and [001] directions, respectively. The supercell consists of a slab of one overlayer of Fe or Au or Fe-Au deposited on 8 atomic layers of Mo, separated by vacuum of about 16 Å. We have allowed the overlayer and three adjacent layers of the substrate to relax, using Hellmann-Feynman forces. In this study, we have considered

only a pseudomorphic monolayer of alloy configurations on the substrate. The convergence of the surface energy with respect to the number of vacuum and atomic layers has also been checked (see Sec. 5.4.2).

For the DFT calculations, we have considered more than 100 different alloy configurations; a detailed description of all the configurations is given in Appendix C. All the distinct configurations possible for the surface unit cell having up to six atoms, as well as a few with seven atoms, were included. Similar to the previous case, to gauge the effect of the substrate as opposed to the dimensionality effect, we have considered two types of systems - one containing an overlayer of Fe or Au or Fe-Au deposited on the Mo(110) surface, referred as deposited monolayers (DM) and another containing only an overlayer without the substrate, but having the same geometry and lattice spacing as that of the substrate, referred to as free-standing monolayers (FSM). These FSM are constrained to two-dimensions without allowing any structural relaxations because in the x-y plane we want the free-standing layers to be confined as on the Mo surface. (In test calculations on a few systems, we found that permitting relaxations in the z-direction had no effect.) By comparing results from these two kinds of systems, we can separate the effect of the presence of the substrate from pure dimensionality effects. Here, we have mainly concentrated on the structural properties of the alloy layers.

After performing the DFT calculations, we have applied the cluster expansion technique (explained in Chapter 2) to the formation energy. To obtain an optimal number of clusters, we have here used the variational cluster expansion code [43, 44]. In this, we start with a pool of a large number of clusters, n_c (n_c is less than the total number of structures n_s), and then

reduce the number such that both the fitting and prediction errors are minimized. To do this, we have used the "leave n_{ex}-out" type of estimation, that is, to fit the cluster expansion, we use $(n_s - n_{ex})$ structures and predict the physical property of interest for the remaining n_{ex} structures. In this work, we have mainly used the "leave 1-out" method, however we also did some calculations with $n_{ex} = 5$ and 10, to ensure that the results did not change significantly. This is in agreement with the conclusions of Arnold, *et al.*, [44] who showed that for a large enough database, a leave 1-out cross validation (CV) is sufficient to select the optimal expansion from noisy databases. We have considered at least five to ten smallest l-point clusters, where $l = 1$, 2, 3, 4, 5, and 6, and also some 7-point clusters. To make sure that we have reached a stable solution, we have worked with a large number of starting pools containing different clusters. Note that the formation energies of both the single-component monolayers – Fe/Mo(110) and Au/Mo(110) – are used as reference levels, and therefore taken equal to zero. While cluster expanding this quantity, we have ensured this constraint by using a linear transformation for the constant term (J_0) and the linear term (J_1); see Eq. (2.27).

5.4 Results and Discussion: *ab initio* Studies

5.4.1 Bulk Calculations

For Mo, the bulk calculations are done using two different unit cells - a conventional bcc unit cell and a monoclinic unit cell with two atoms per unit cell which is commensurate with the (110) surface geometry. For Fe

Element	Unit cell	a_{expt} (Å)	a_{calc} (Å)
Mo	bcc	2.73	2.75
	monoclinic	2.73	2.75
Fe	bcc	2.48	2.46
Au	fcc	2.89	2.93

Table 5.2: *The experimental and the calculated values of NN spacing for the elements in their bulk crystal structure: the percentage difference in the calculated and experimental values is not more than 2% for all three elements.*

and Au, the bulk calculations are done in their respective bulk unit cells, that is bcc and face-centered cubic (fcc). The results for the NN spacing for each of the elements are tabulated in Table 5.2. There is good agreement between the calculated and the experimental values; for Fe and Au, the calculated values match well with those calculated in Chapter 3 using the PBE exchange-correlation. For Fe, spin-polarized calculations are performed. The calculated value of the magnetic moment for bulk Fe is 2.35 μ_B as compared to the experimental value of 2.22 μ_B; this also matches well with the value calculated in Chapter 3 using the PBE exchange-correlation.

5.4.2 Clean Mo(110) Surface

To ascertain that there is no interaction between the two surfaces of the slab, either through vacuum or bulk layers, we have done extensive convergence tests for the surface energy with respect to the number of atomic and vacuum layers. The surface energy is defined as:

$$E^{surf} = \frac{E^{slab} - n_a E^{bulk}}{2}, \tag{5.1}$$

E^{surf} (eV)	k-point grid	
n_v	10×10×1	15×15×1
5	1.233	1.233
6	1.232	1.232
7	1.232	1.233
8	1.232	1.233
9	-	1.233

Table 5.3: *The surface energy E^{surf} for Mo(110) is tabulated as a function of the number of vacuum layers n_v, calculated using two different k-point grids. For this convergence test, we have used a slab containing six atomic layers, and the outer two atomic layers on each side of the slab were allowed to relax.*

where E^{slab} is the total energy for a slab containing n_a atomic layers, and E^{bulk} is the total energy per atom for the bulk structure commensurate with the slab (in this case the monoclinic unit cell). For these convergence tests, we have allowed relaxations of the outer two layers of Mo on each side of the slab.

Initially keeping the number of atomic layers n_a fixed ($n_a = 6$), the calculations were done for convergence with respect to the number of vacuum layers n_v. The results for the surface energy as a function of n_v, calculated for two different k-point meshes, are tabulated in Table 5.3. For both the cases, satisfactory convergence has been achieved at $n_v = 7$, which approximately corresponds to a vacuum thickness of 15.8 Å.

Now fixing $n_v = 7$, we have varied n_a, the number of atomic layers in the slab. The surface energy as a function of n_a, calculated for several k-point meshes, is plotted in Fig. 5.2. From the plot, we can see that a dense k-point mesh (21×21) and a large number of atomic layers (12 to 14) are required to achieve a very high degree of convergence. However, using these parameters would be very demanding for the surface alloy calculations. Therefore we

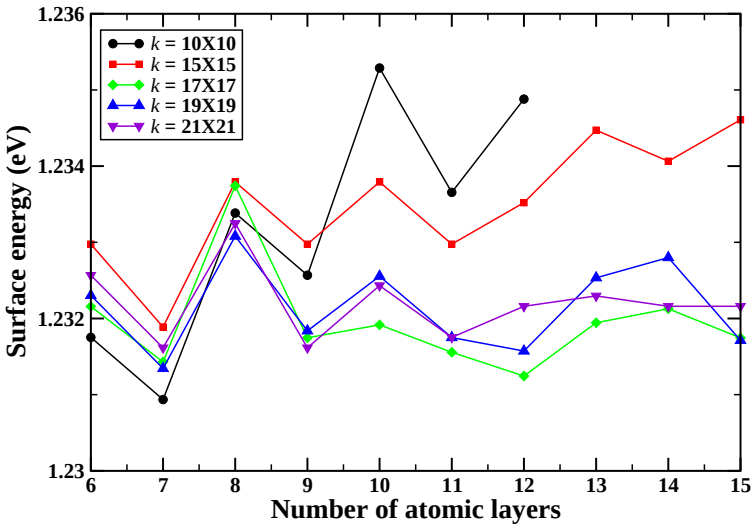

Figure 5.2: *The surface energy of the clean Mo(110) surface: The calculated surface energy of a slab of Mo(110) as a function of number of atomic layers in the slab is plotted for different k-point meshes.*

have selected intermediate but acceptable parameters, viz., a (17×17) k-point mesh and 8 atomic layers. For this particular choice, the surface energy value is equal to 1.232 eV per atom as compared to the converged surface energy 1.234 eV per surface atom which gives an error of 0.16 %. Our calculated E^{surf} value is smaller than the previously reported values which range from 1.29–1.53 eV/atom [117, 164–167].

The interlayer distance between the topmost layer and the adjacent layer, d_{12}, is 2.16 Å, as compared to the interlayer distance for bulk Mo, d_{bulk}, which is 2.25 Å. This indicates that the topmost layer relaxes towards the substrate by about -4.0%. For the next layer, the interlayer distance d_{23} is 2.26 Å, which indicates that the second layer from the surface relaxes outward by about

0.4%. These results match reasonably well with previous results [156]. The ideal bulk-truncated Mo(110) surface is under tensile stress; the calculated values of the xx and yy components of the surface stress are equal to -0.608 eV/Å^2 and -0.578 eV/Å^2 respectively. After allowing two surface layers to relax, the surface stress values are reduced from those for the bulk-truncated surface, the xx and yy components being equal to -0.423 eV/Å^2 and -0.449 eV/Å^2 respectively.

5.4.3 Single-component Monolayers on Mo(110)

Initially we have studied the properties of single-component monolayers of either Fe or Au deposited on the Mo(110) surface. For a single layer of Fe on the surface, the magnetic moment is equal to 2.72 μ_B per Fe atom, which is enhanced compared to that of bulk Fe, as was observed before [156]. The Fe monolayer induces magnetic moments on the adjacent Mo layers with AFM coupling; the moment on the adjacent layer is -0.15 μ_B and that on the next layer is -0.01 μ_B; these values are slightly higher than the ones calculated before [156]. The induced moments on the remaining layers are much smaller, as shown in Fig. 5.3.

After geometric relaxations, the interlayer distance between the Fe layer and the adjacent Mo layer becomes 2.01 Å, which is contracted by about -11.0 % relative to the bulk Mo interlayer distance; this is expected based on the atomic size mismatch between bulk Fe and Mo. On Fe deposition, the interlayer distance between two adjacent Mo layers decreases to 2.26 Å, which is expanded by 0.4% relative to the bulk; this is much less compared

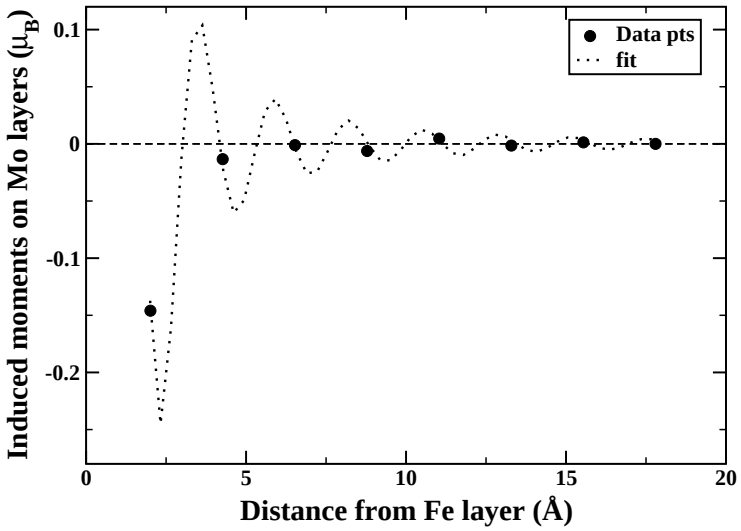

Figure 5.3: *Induced magnetic moments on Mo layers when an Fe layer is deposited on the surface: we have shown here induced magnetic moments on the Mo atoms (in μ_B) as a function of distance from the Fe layer. Black circles are actual data points and dotted line is a fit to a simple oscillatory function using Eq.* (3.1)*. This is similar to RKKY interaction.*

to the clean surface. These trends are qualitatively consistent with earlier observations [156].

For Au/Mo(110), the relaxed interlayer distance between the deposited Au layer and the adjacent Mo layer is equal to 2.39 Å, which is expanded by 6.2% with respect to the bulk Mo interlayer distance. On Au deposition, the interlayer distance between the first and the second Mo layers relaxes to 2.19 Å, which is compressed by 2.7% relative to the bulk; this is slightly less compared to the clean surface.

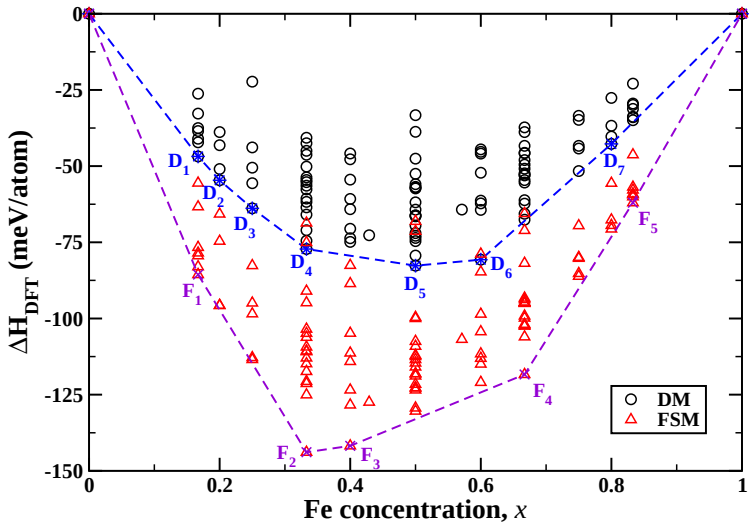

Figure 5.4: *Dependence of the formation energy ΔH_{DFT} on the Fe concentration x calculated using DFT: black circles denote ΔH for the deposited monolayers and red triangles denote that for the free-standing monolayers. The configurations lying on the convex hulls are highlighted by stars and crosses connected by dashed lines for DM and FSM respectively. Each configuration on both of the convex hulls is labeled and the top view of each is given in Fig. 5.5.*

5.4.4 Free-standing versus Deposited Alloy Monolayers

In this work, we are interested in determining whether mixing of Fe and Au in 2D is dependent on the nature of the substrate, and how much is the effect of the substrate on stability. Therefore for each configuration, we have calculated the formation energy, which is a measure of miscibility. The formation energy of an alloy is defined as follows:

$$\Delta H = E(Fe_xAu_{1-x}) - xE(Fe) - (1-x)E(Au), \tag{5.2}$$

where $E(A)$ is the total energy per atom of a monolayer (either free-standing or deposited) of A. If ΔH is negative, then the mixing of the two components is favored. We have plotted ΔH as a function of the Fe concentration x, as obtained from *ab initio* DFT calculations, for both FSM and DM in Fig. 5.4, where each point corresponds to a different configuration. The formation energy is negative for all the configurations studied for both free-standing and deposited monolayers, which implies alloying is favored whether or not the substrate is present. This observation is the same as the Fe-Au/Ru(0001) system described in the previous chapter, implying that the 2D single-layer Fe-Au alloyed phases are stable, unlike the 3D bulk Fe-Au phases. However, unlike the previous case (refer to Figs. 4.4(a) and 4.8(a)), here in the presence of the substrate the tendency towards mixing is reduced considerably, that is, for each configuration, the $|\Delta H|$ values are significantly smaller for DM than for FSM configurations. In the same plot, we have highlighted the convex hulls (stars and crosses connected by dashed lines) signifying the ground state (GS) structures for both the cases. For FSM, we see that there is a slight asymmetry around $x = 0.50$ indicating that Au-rich phases are more stable as compared to the Fe-rich phases; whereas for DM, the mixing is more-or-less symmetric about $x = 0.50$.

A closer look at the structures on the convex hull would be useful to understand trends in alloy phases (if they exist) such as whether configurations having stripes are more favored or configurations in which one of the metals (Fe or Au) likes to be surrounded by the other metal, leading to a high degree of atomic-level mixing. We have labeled each structure on the convex hull in Fig. 5.4; schematic top views for each of these configurations are shown in

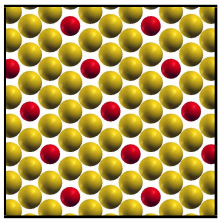

(F_1) $FeAu_5$ in the unit cell ($3 \times \sqrt{5}\alpha$)

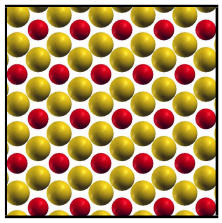

(F_2) $FeAu_2$ in the unit cell ($2\sqrt{2}\alpha \times \sqrt{5}\alpha$)

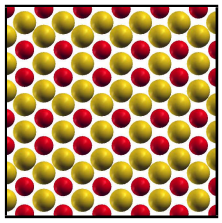

(F_3) Fe_2Au_3 in the unit cell ($2\sqrt{2}\alpha \times 3$) - configuration 1

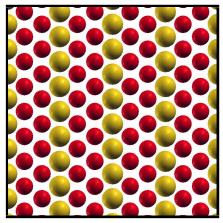

(F_4) Fe_2Au in the unit cell ($\sqrt{7}\alpha \times 2\alpha$)

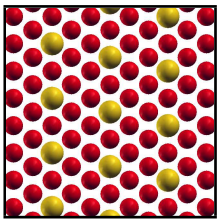

(F_5) Fe_5Au in the unit cell ($3 \times 4\alpha$)

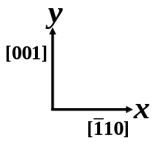

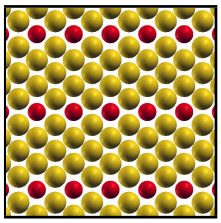

(D_1) $FeAu_5$ in the unit cell ($2\sqrt{2}\alpha \times 6\alpha$)

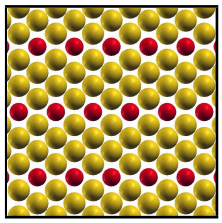

(D_2) $FeAu_4$ in the unit cell ($2\sqrt{2}\alpha \times 3$)

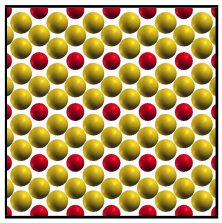

(D_3) $FeAu_3$ in the unit cell ($2\sqrt{2}\alpha \times 4\alpha$)

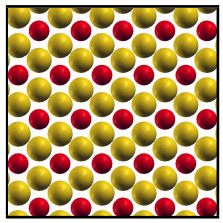

(D_4) $FeAu_2$ in the unit cell ($2\sqrt{2}\alpha \times \sqrt{5}\alpha$)

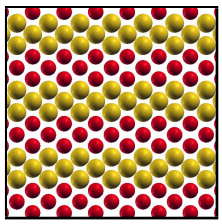

(D_5) Fe_3Au_3 in the unit cell ($2\sqrt{2}\alpha \times 6\alpha$) - configuration 1

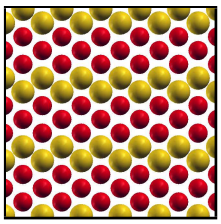

(D_6) Fe_3Au_2 in the unit cell ($2\sqrt{2}\alpha \times 3$) - configuration 2

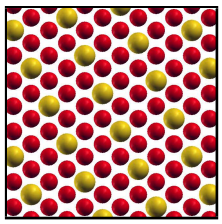

(D_7) Fe_4Au in the unit cell ($\sqrt{8} \times \sqrt{5}\alpha$)

Figure 5.5: *Schematic top view for each configuration falling on the convex hull for free-standing and deposited monolayers: Each structure is labeled by the same label as was done in Fig. 5.4. Here* $\alpha = 1/\sqrt{3}$. *Yellow spheres denote the Au atoms, and red spheres denote the Fe atoms.*

Fig. 5.5. For FSM, out of five configurations on the convex hull, four have isolated atoms of either Fe (for Au-rich phases) or Au (Fe-rich phases). the exception is the structure labeled as F_4 at $x = 0.667$, which has stripes along the [001] direction. In contrast, for the DM phases, for $x < 0.50$, each of the configurations on the convex hull has one Fe stripe separated by a varying number of Au stripes oriented along the $[\bar{1}10]$ direction. Similar striped structures are observed for D_5 and D_6 also, but the Fe stripe width has increased from one to three. The only exception to this is D_7, with has no stripes. Note that at $x = 0.33$, both the DM and FSM phases have the same structure on the convex hull, viz., $(2\sqrt{2}\alpha \times \sqrt{5}\alpha)$ unit cell where $\alpha = 1/\sqrt{3}$.

We are also interested in the magnetic properties of these alloys, so we have plotted the total magnetic moment per Fe atom as a function of x, for both DM and FSM systems in Fig. 5.6. Note that for all the configurations for either deposited or free-standing monolayers, the magnetic moment on the Fe atom is increased from its calculated bulk value which is equal to 2.35 μ_B. As x increases, the magnetic moment per Fe atom decreases. There is a significant decrease in magnetic moments when a FeAu monolayer is deposited on the substrate, which is expected from the Stoner argument. In the same plot, we have marked the configurations falling on the convex hull by stars and crosses for DM and FSM phases respectively. However, we do not see any direct correlation between the most stable structures and the magnetic moments, as was seen in the previous chapter for Fe-Au/Ru(0001), except in two cases – for FSM configurations at $x = 0.33$ and 0.4 the highest moments correspond to the most stable states.

We have performed non-spin-polarized calculations for a few deposited

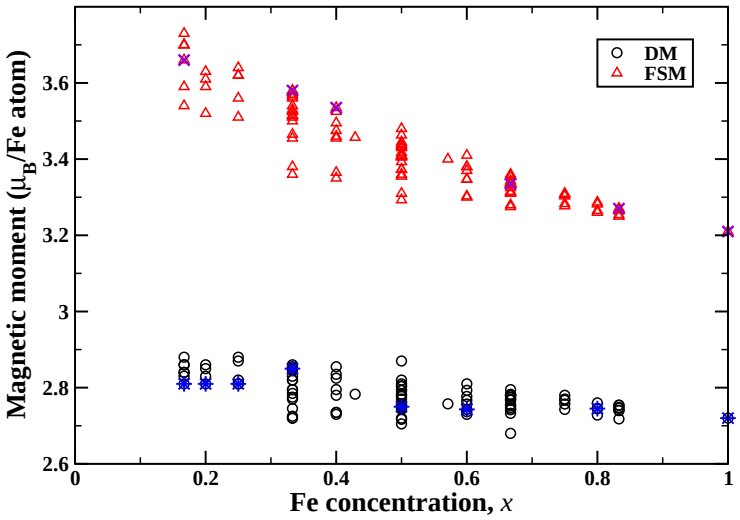

Figure 5.6: *Dependence of the magnetic moment, per Fe atom, on Fe concentration x: Circles denote moments for deposited monolayers and triangles denote those for free-standing monolayers. On deposition of FeAu layer on the substrate, there is a significant decrease in magnetic moments. For DM and FSM configurations, structures on the convex hulls are marked by stars and crosses respectively.*

configurations; for example, the formation energy values for some configurations are tabulated in Table 5.4 along with those for the SP calculations. We do not see any clear trend of reduced miscibility on turning off the magnetization, as was observed for Fe-Au/Ru(0001) (compare with Fig. 4.4). This observation along with the absence of correlation between the highest moments and the most miscible structures, imply that magnetic interactions are not the dominant interactions which drive mixing.

As explained in Chapter 3, the surface stress has been considered as the main driving force for the formation of surface alloys [74, 78]. Therefore, we have calculated surface stress σ^{surf} components for each configuration. The

Configuration	ΔH^{NSP}	ΔH^{SP}	$\Delta H^{NSP} - \Delta H^{SP}$
FeAu (2×1)	-0.069	-0.039	-0.030
FeAu $(2\sqrt{2}\alpha \times 2\alpha)$	-0.039	-0.033	-0.006
Fe_2Au (3×1)	-0.062	-0.046	-0.016
Fe_2Au $(2\sqrt{2}\alpha \times \sqrt{5}\alpha)$	-0.151	-0.053	-0.098
Fe_2Au $(\sqrt{7}\alpha \times 2\alpha)$	-0.075	-0.061	-0.014
$FeAu_2$ (3×1)	-0.060	-0.062	0.002
$FeAu_2$ $(2\sqrt{2}\alpha \times \sqrt{5}\alpha)$	-0.098	-0.077	-0.021
$FeAu_2$ $(\sqrt{7}\alpha \times 2\alpha)$	-0.076	-0.058	-0.018

Table 5.4: *We have tabulated here ΔH values (in eV/atom) of some configurations for non-spin polarized (second column) and spin polarized (third column) calculations. The last column is the difference between SP and NSP values. Note that magnitude of ΔH increases in some cases, and reduces for others after switching off the magnetization. Here $\alpha = 1/\sqrt{3}$, and description of each configuration is given in Appendix D.*

xx and yy components of the surface stress as a function of the Fe concentration x are plotted in Fig. 5.7(a) and (b) for supported and unsupported monolayers, respectively. For most of these configurations, the off-diagonal terms are very small compared to diagonal terms, and are therefore not shown here. For all the alloy configurations (either FSM or DM), the surface stress has a negative sign, indicating that the overlayers are under tensile stress. For free-standing monolayers, this is not unexpected because atoms have lower coordination than in the bulk, and hence want to reduce the NN distance between atoms. Further, for the free-standing monolayer of Fe, the stress values are almost equal, as compared to Au FSM, for which the stress value along the y-direction is larger compared to that along the x-direction.

For deposited monolayers, one might have expected that the pure Au layer on Mo(110) will be under compression in the x direction based on atomic-size mismatch for the bulk (see Table 5.1); however, this is not the case. This

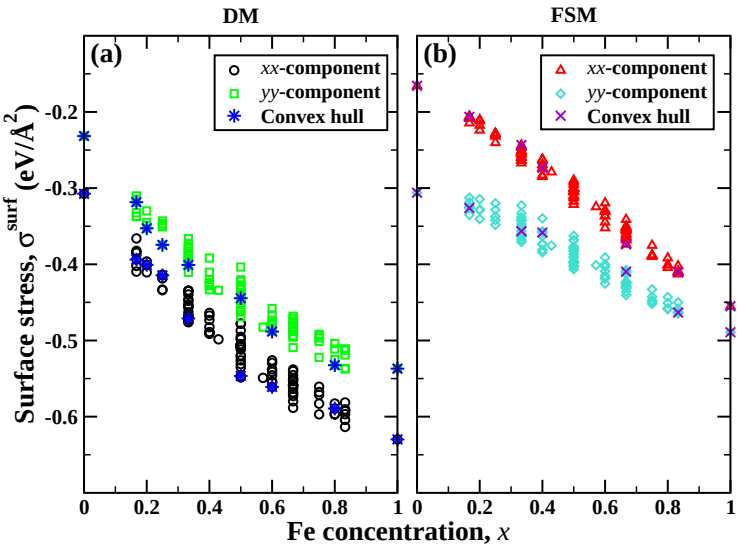

Figure 5.7: *Surface stress σ^{surf} as a function of x: The xx and yy components of the surface stress are plotted as a function of Fe concentration x for (a) DM and (b) FSM. The stress is tensile for all the configurations in both DM and FSM systems. However, the stress values for the DM are higher than those for the FSM. The stars and crosses indicate the configurations on the convex hull.*

might be attributed to the reduced coordination of Au atoms on the Mo(110) surface, which can affect the effective size on the surface, thus driving the surface stress from compressive to tensile. For all the configurations, the magnitude of xx-component of the stress is larger than the yy-component, which can be attributed to a larger atomic-size mismatch in the x-direction. For each quantity on this plot, we have marked those configurations which fall on the convex hull for DM and FSM systems using stars and crosses respectively. There seems to be no clear trend correlating a lower surface stress with a higher stability of a configuration. For this system, we observe that both Fe and Au layers on the Mo(110) surface are under tensile stress

so the mixing need not eliminate the stress. This may suggest that for this system the elastic interactions may not be a driving force for the alloy formation.

5.4.5 Comparison with FeAu/Ru(0001)

We have already referred to qualitative similarities or differences between two systems – FeAu thin films on Mo(110) and Ru(0001) – now we will quantitatively compare these two systems. We have compared both the deposited and free-standing configurations for these systems. Recall that the two substrates have very similar NN distances (larger for Mo by about 1 %), and the centered-rectangular lattice of the bcc(110) surface can be considered as a strained hexagonal lattice; therefore we expect similar results for the FSM configurations in the two geometries. In Fig. 5.8(a) and (b), we have plotted the formation energy as a function of the Fe concentration x for the DM and FSM phases respectively for both systems. For the FSM phases, the values of ΔH are comparable to each other in the two geometries, as expected. In contrast, for the DM phases, all the studied alloy configurations are more stable on Ru(0001) as compared to those on Mo(110). For example, at $x = 0.33$, the most stable structure for FeAu/Ru(0001) has ΔH equal to -177.4 meV/atom as compared to ΔH of -77.2 meV/atom calculated for the most stable structure on Mo(110). At any concentration, the difference between the formation energies of the most stable configurations for the hexagonal and centered-rectangular geometries is less than 40 meV/atom, whereas for the deposited phases, it is always more than 50 meV/atom.

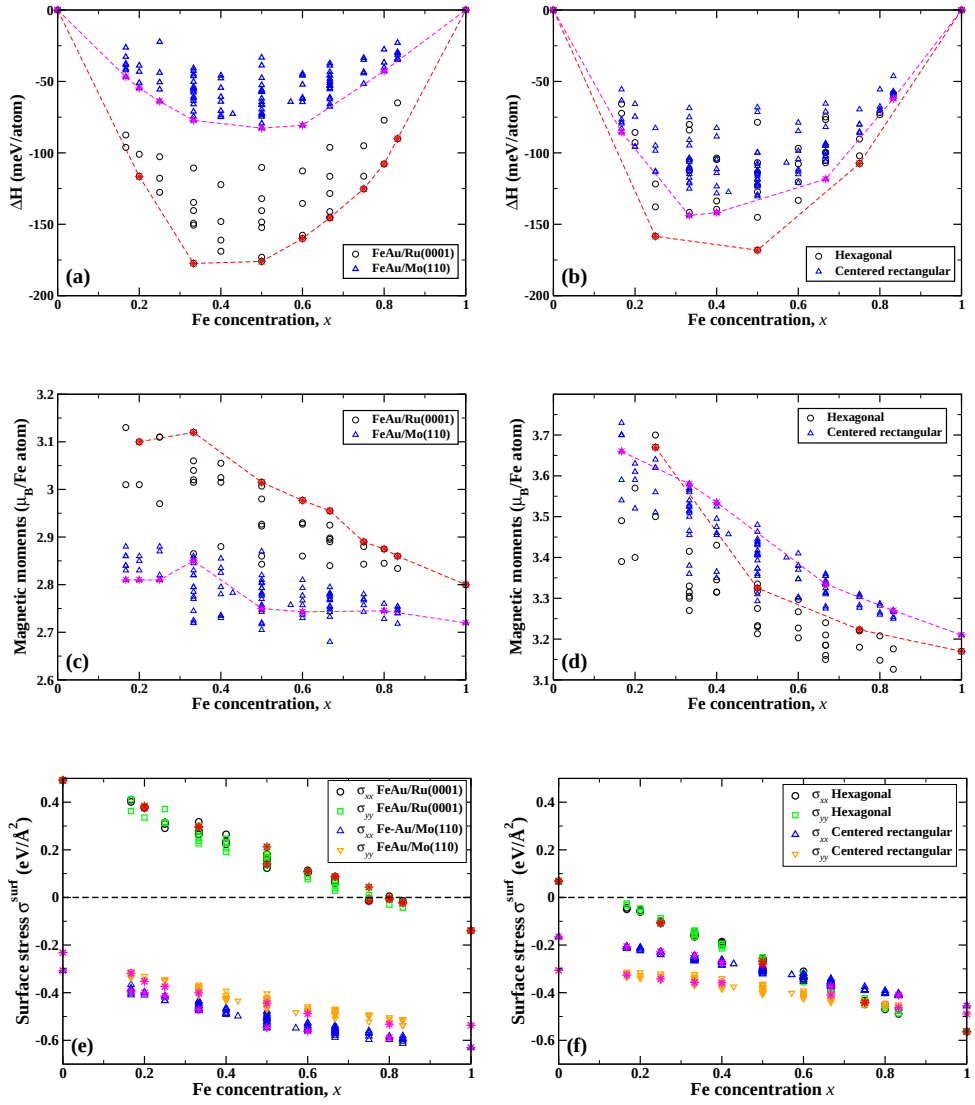

Figure 5.8: *Comparison of the formation energy, magnetic moments and surface stress components for the two substrates: we have plotted here ΔH, the magnetic moments and xx and yy components of the surface stress for 2D FeAu films deposited on the Mo(110) and Ru(0001) substrates (a, c and e) and for free-standing configurations at those two geometries (b, d and f). Circles and triangles denote results for Ru(0001) or hexagonal geometry and Mo(110) or centered-rectangular geometry respectively. For each system, we have also shown the structures on the corresponding convex hulls.*

In Fig. 5.8(c) and (d), we have plotted the magnetic moment as a function of x for DM and FSM phases respectively. For free-standing monolayers, the magnetic moments are very similar to each other irrespective of different geometries. However, for the deposited monolayers, we observe that magnetic moments are reduced when the substrate is changed from Ru to Mo; the reduction is however only slight. The reduced moments correspond to a higher stability of the alloys on the Ru(0001) surface.

In Fig. 5.8(e) and (f), we have plotted the xx and yy components of the surface stress for deposited and free-standing monolayers respectively for both systems. Note that the surface stress for FSM in the hcp geometry is smaller than that in the centered-rectangular geometry except for Fe-rich phases ($x > 0.7$). This can be explained by the slightly smaller NN distance of Ru, because free-standing monolayers would prefer smaller bond lengths owing to less number of neighbors. As expected, in the case of centered-rectangular geometry, we can clearly see an anisotropy between xx and yy components, which is not present in the hexagonal phases. For example, at $x = 0.5$, the highest stress values for hcp alloy monolayers are -0.29 eV/Å^2 and -0.27 eV/Å^2 for xx and yy components respectively, and those for centered-rectangular alloy monolayers are -0.32 eV/Å^2 and -0.41 eV/Å^2. Further, this is in correspondence with higher $|\Delta H|$ value for the hcp alloy monolayers (168.1 meV/atom) than that for alloy centered-rectangular (130.4 meV/atom).

For the DM phases, we clearly observe that the surface stress values are higher for monolayers deposited on the Mo(110) surface at most of the concentrations. This is in accordance with the slightly larger atomic-size

mismatch for both Fe and Au on the Mo(110) surface than on Ru(0001) along the x as well as y directions. As an example, consider the $x = 0.5$ case: the highest stress values for Fe-Au/Ru(0001) are 0.18 eV/Å^2 and 0.21 eV/Å^2 respectively, which are smaller in magnitude than those for Fe-Au/Mo(110), which are equal to -0.55 eV/Å^2 and -0.47 eV/Å^2. This accords well with the higher $|\Delta H|$ on the Ru(0001) surface (176.0 meV/atom) than that on the Mo(110) surface (82.67 eV/atom). We would like to note here that as we change the substrate from Ru to Mo, we have observed an increase in the surface stress, and reduction in the miscibility. This increase in σ^{surf} along with the reduced magnetic moments would explain the reduced mixing on the Mo(110) surface, as compared to Ru(0001).

Further, we have seen that on the Ru substrate structures having isolated Fe or Au atoms are preferred, whereas striped structures are preferred on the Mo(110) substrate. The anisotropy of the latter can give rise to this difference.

5.5 Results and Discussion: Cluster Expansion Studies

We have used the cluster expansion technique to search for the GS configurations for both the FSM and DM systems. To achieve this, we have cluster expanded the formation energy for each system.

First, we have started with the formation energy for the free-standing monolayers. We have shown a typical plot for the fitting and cross-validation

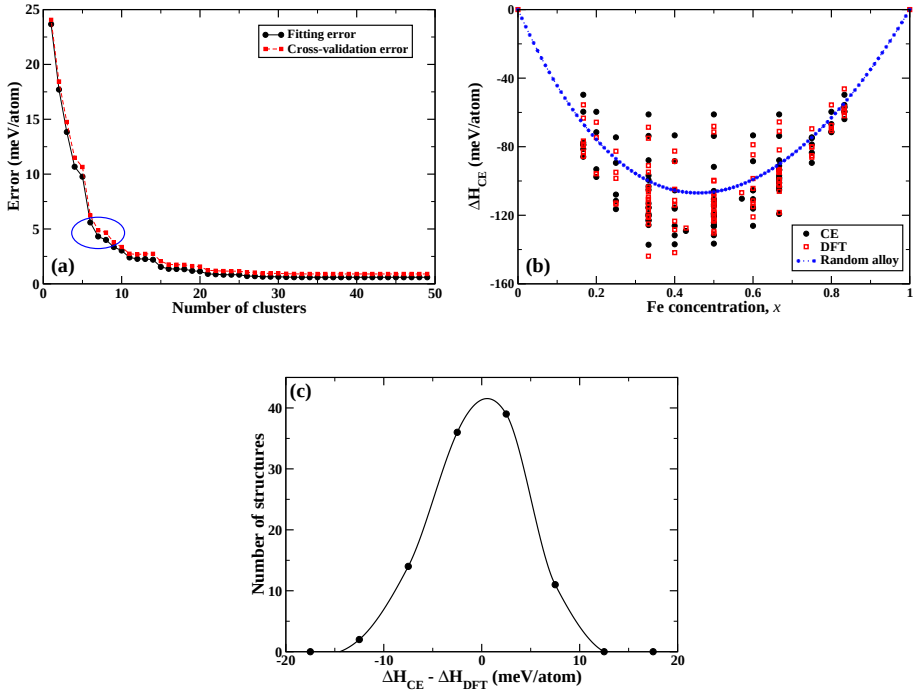

Figure 5.9: *(a) Fitting and cross-validation errors as a function of the number of clusters for FSM: We have encircled the area where we observe a large error introduced by removing just a single cluster figure around $n_c = 7$. (b) Comparison between ab initio and CE predicted ΔH for the FSM phases using a set of seven clusters: The predicted values match within 5 meV/atom for all the configurations. On the same plot, we have also plotted the formation energy values for random alloys calculated using the same cluster set. (c) The error distribution, that is, the number of structures having $(\Delta H_{CE} - \Delta H_{DFT})$ values in 5 meV/atom window is shown. Here dots correspond to the data points, while the solid line is a smooth spline fit to the data points.*

(CV) errors as a function of number of clusters n_c in the pool, in Fig. 5.9(a). The errors remain almost constant till n_c is reduced to less than 20, and a significant increase in errors is observed only when $n_c = 7$. Therefore, we have considered this to be an optimum solution, where both types of errors are still less than 5 meV/atom. Then, to determine the quality of this set, we use this solution to calculate the formation energies for all the configurations

using the effective cluster interactions (ECI) in the Hamiltonian. We have plotted the predicted ΔH along with the *ab initio* values in Fig. 5.9(b) for comparison. There is good agreement between the two sets of values. This can also be seen from the error distribution plot shown in Fig. 5.9(c); this plot shows the number of structures which have $(\Delta H_{CE} - \Delta H_{DFT})$ values in 5 meV/atom energy window. The error distribution looks more-or-less symmetric about zero error, which implies that the solution obtained would well describe the system [50]. However, there are not enough data points to gain quantitative information about the distribution. The average squared error δ between the DFT values and the CE values, defined by:

$$\delta^2 = \frac{\sum_i |\Delta H_{CE} - \Delta H_{DFT}|^2}{n_s}, \tag{5.3}$$

where ΔH_{CE} and ΔH_{DFT} are the CE calculated and the *ab initio* formation energies respectively, and the sum is taken over n_s structures, is equal to 4.52 meV/atom for this particular cluster set for FSM structures. Note that we have confirmed that the truncation of the series does not lead to significant errors, by considering a larger cluster pool as a solution, and comparing between the cluster expanded and the DFT formation energies. This optimal cluster pool required for good prediction of the data has seven cluster figures – five of which are the first five nearest-neighbor pair interactions, one three-body interaction, and one four-body interaction. These clusters are shown in Fig. 5.10, along with a bar chart showing the effective cluster interactions for each of the cluster. The most dominant term is the nearest-neighbor pair interaction with the highest value of ECI, followed by a next-NN pair

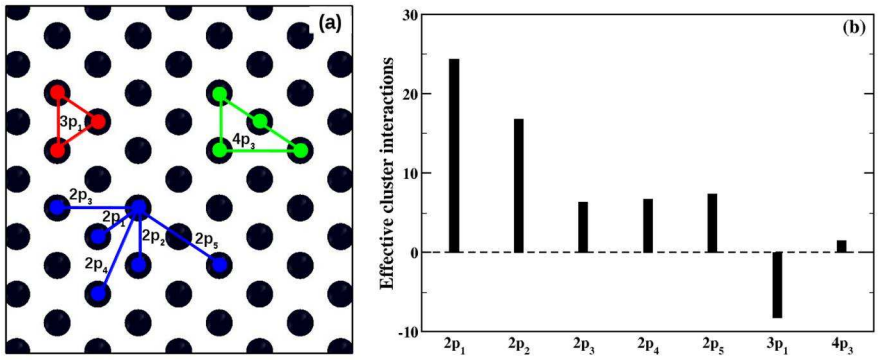

Figure 5.10: *(a) The optimal cluster set required to get a good convergence for the formation energy of free-standing monolayers containing seven cluster figures is shown here. Here each cluster figure is labelled by lP_x where l is the number of lattice points in that cluster, and x is an integer taking values 1, 2, $\cdots$ and so on, indicating increasing length of the cluster figures. For example, $2P_1$ is the two-point cluster between the shortest possible length (NN atoms). (b) The bar chart shows the effective cluster interactions (in meV/atom) corresponding to each of the clusters shown in (a).*

interaction.

In Fig. 5.9(b), along with ΔH_{CE} for the ordered configurations, we have plotted the formation energy for random alloys, shown with blue stars. Here the random alloy at each concentration x is defined by defining a cluster function by the product of averages of the occupation variable,

$$\langle \phi_\alpha \rangle_{random} = (2x-1)^{n_\alpha}, \tag{5.4}$$

where $\langle \phi_\alpha \rangle$ is the occupation variable for the cluster figure α having n_α sites. Using this and the calculated effective cluster interactions, we have calculated the formation energy for random alloys. Note that for all x, ΔH for random alloys is negative, indicating that random alloys are stable. At $x = 0.33$, where we have obtained the most stable structure, the difference between the GS and random alloy formation energies is large – about 40 meV/atom.

This suggests that ordering is more favored than the formation of random alloys.

Next, we have followed the same procedure as was used for the FSM system, to obtain a solution for cluster expansion of the formation energy of the DM phases. In Fig. 5.11(a), we have plotted the fitting and cross-validation errors for an optimal cluster pool obtained by us. Note that for the FSM phases, both the errors were almost zero for large pool sizes, whereas for the DM phases, even at large pool sizes, the errors are about 3 meV per atom. This error remains almost constant as n_c is lowered till about $n_c = 9$, and then it starts to increase as n_c is lowered further. Therefore we have considered a cluster pool containing nine clusters to predict the formation energies using the corresponding ECI values. To crosscheck this solution, we have compared the formation energies obtained from the CE Hamiltonian, with those from DFT, as shown in Fig. 5.11(b). In general, we observe a good agreement between the predicted and calculated GS structures, that is, within the CV error ($\sim$ 5 meV/atom). The average squared error δ between the DFT values and the CE values is equal to 4.12 meV/atom. In the same figure, we have also plotted ΔH for random alloys for a range of x; we see that for all x, the formation energy for random alloys is negative, and the magnitude of ΔH for random alloys is smaller than the ordered structures. In Fig. 5.11(c), we have plotted the error distribution, that is, the number of structures having $(\Delta H_{CE} - \Delta H_{DFT})$ values in 5 meV/atom energy window. As for the FSM, the error distribution is more-or-less symmetric and hence will describe the system well [50].

For the ΔH of deposited monolayers, we have found that more clusters are

required to describe interactions more accurately, with six two-body interactions, two three-body interactions and one four-body interaction term. This might be because when a Fe-Au layer is deposited on the Mo(110) surface, there will be additional interactions present, mediated through the substrate layers. The optimal cluster figures are shown in Fig. 5.12, along with the corresponding effective cluster interactions. The most dominant interaction

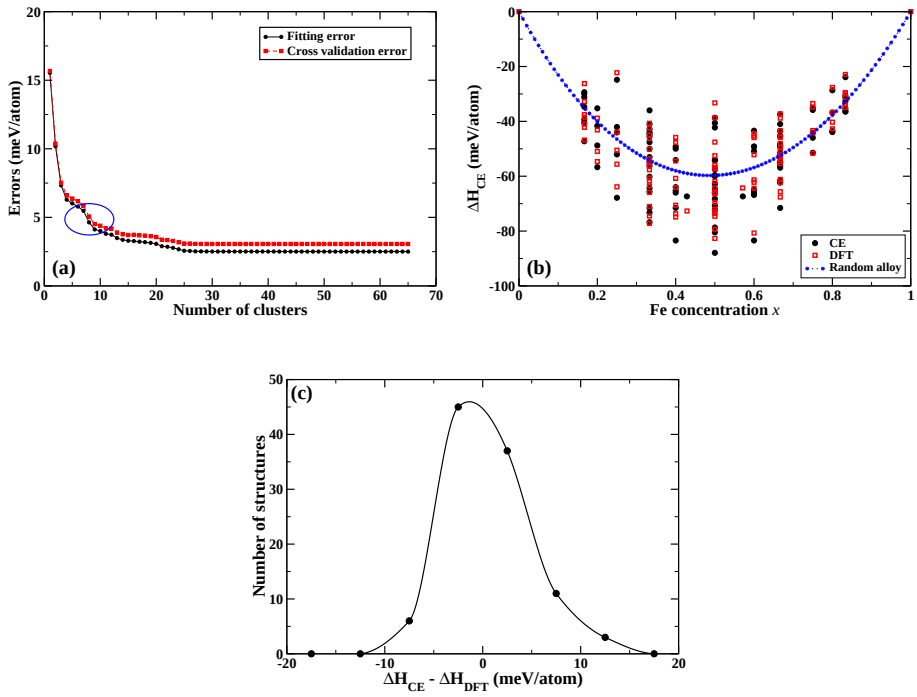

Figure 5.11: *(a) Fitting and cross-validation errors as a function of the number of clusters for DM: We have encircled the region where we see a large increase in the errors after removing just a single cluster. (b) Comparison between ab initio and CE predicted ΔH for the DM phases using a set of nine clusters: The predicted values match within 5 meV/atom for all the configurations. On the same plot, we have also plotted the formation energy values for random alloys calculated using the same cluster set. (c) The error distribution, that is, the number of structures having $(\Delta H_{CE} - \Delta H_{DFT})$ values in 5 meV/atom window is shown. Here dots correspond to the data points, while the solid line is a smooth spline fit to the data points.*

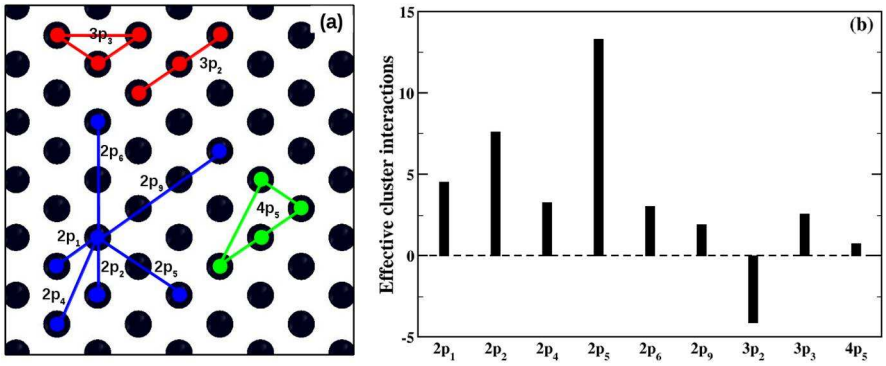

Figure 5.12: *Optimal cluster set for the formation energy for deposited monolayers with the corresponding effective cluster interactions: (a) We have shown here nine clusters which are required to get converged results to predict the formation energies of the DM phases. (b) The bar chart shows effective cluster interactions (in meV/atom) for each of the clusters shown in (a).*

for the DM systems is the fifth longest two-body interaction ($2P_5$), which is followed by the next-NN pair interaction.

5.5.1 Search for the Ground State Structures

One of the advantages of the cluster expansion technique is that it can be used to calculate the energies of very large structures with much less computational effort as compared to complete DFT calculations, as explained in Chapter 2. So after obtaining solutions for the cluster expansion of formation energies, we have considered a large number of alloy configurations for which we calculate formation energies using the optimized CE solution. This will enable us to find the ground state structures, if present, which are not included in our DFT database because of their large size. We have used the enumeration code developed by G. Hart, *et al.* [168] to generate a large structural database. This code uses an algorithm (based on a group theory approach) to determine all distinct superlattice structures and then to generate

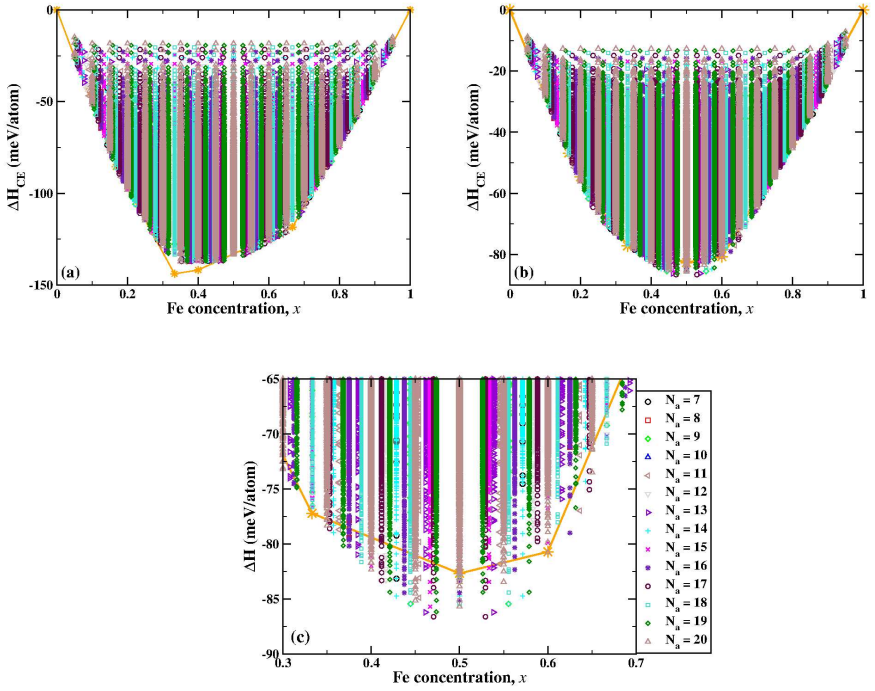

Figure 5.13: *Ground state search using CE calculated formation energies for (a) FSM and (b) DM: The formation energy ΔH_{CE} as a function of x is plotted for all the alloy configurations containing up to 20 atoms per unit cell. For comparison, we have also shown here the DFT calculated convex hulls for both the systems with orange stars. In panel (c), we have shown a zoomed-in region near $x = 0.50$ to panel (b), to clearly compare the DFT convex hull with the lowest lying configurations obtained from CE.*

all possible atomic configurations on each superlattice; the symmetry operations of the lattice are used to exclude symmetry-equivalent structures [168]. For the ground state search, we have included all the distinct configurations up to $N_a = 20$, and thus the total number of structures considered for the ground state search is more than a million.

In Fig. 5.13, we have plotted the formation energy calculated using the CE Hamiltonian for all larger structures – not included in the original DFT database – for both (a) free-standing and (b) deposited monolayers. On each

plot, we have also plotted the respective convex hull for FSM and DM, as obtained by the DFT calculations, for comparison. For both kinds of systems, we note that all the configurations have negative ΔH values, implying that mixing is favored at all x. For FSM phases, around $x = 0.33$ and 0.4, the lowest energy structures are the same as were obtained by *ab initio* methods, and at the remaining x values, there are a large number of structures which appear to have energies either lower or very near to those structures lying on the convex hull. The CE-calculated values have an error bar of about 5 meV/atom, and thus it is difficult to exactly define the convex hull using the ΔH_{CE} values. Note that at the two concentrations where we have obtained clearly defined ground states, we have also observed a one-to-one correlation between the highest magnetic moment and the greatest stability (see Fig. 5.6).

For DM phases, at each x, there are many structures which appear below or near the convex hull calculated with the DFT database; this can be clearly seen in panel (c) where we have shown a zoomed-in region for the DM data. Many of the low-lying structures have comparable values which lie within the error bars for ΔH_{CE}, and thus it is difficult to define the ground state structures. The convex hull for the DM phases is a continuous smooth curve implying only short range order is possible. We note that many of the structures near the convex hull have striped structures, with the stripes aligned along the $[\bar{1}10]$ direction. At any x, there are several low energy structures which have very small energy differences, and hence the system has many competing structures. These observations are consistent with the previous experimental result [163] where the authors have reported the formation of

an Fe-Au alloy, but an absence of ordering.

5.6 Summary and Conclusions

In summary, we have studied the structural and magnetic properties of a large number of ordered alloy configurations of an FeAu monolayer deposited on the Mo(110) surface. We have shown that the alloy phases are favored over the phase segregated phases for all the configurations of a Fe-Au monolayer, whether or not it is supported. This confirms the conclusion that the mixing is largely affected by the dimensionality. The magnetic moments are enhanced as compared to the bulk Fe moments for these surface alloys. We have also calculated the surface stress for each configuration. In general, we do not find any correlation between the greatest stability and the highest magnetic moments or the lowest surface stress.

In our study, we have found that deposited monolayers prefer to have striped structures with stripes along the $[\bar{1}10]$ direction. This is in contrast to the experimental studies on Fe-Ag/Mo(110) [83] in which stripes along the [001] direction of the surface were observed. This may arise from different chemical interactions for Ag and Au alloys with Fe, which lead to different mixing properties on the Ru(0001) surface, as described in Chapter 3.

Using the DFT results, we have cluster expanded the formation energy of alloys for both types of systems and found the effective cluster interactions required to calculate the formation energy of the larger unit cells. We have compared the direct DFT results (done for two to six atoms per unit cell) with those obtained from the CE Hamiltonian; the two results match within

error bars. We have then calculated the formation energy for all the alloy configurations containing seven to 20 atoms per unit cell to extend the ground state search. For the FSM phases, around $x = 0.33$ and 0.4, the lowest energy structures are the same as those calculated using DFT, but at all other concentrations, there are a large number of structures which fall below the DFT convex hull and are nearly degenerate in energy. Similarly, for the DM phases, at all concentrations under study, we have observed that a number of configurations lie below the DFT convex hull, and at a given x, many of these configurations have energies within the error bars of the CE calculation. This implies that the configurations on the smaller unit cell DFT "convex hulls" are not the "real ground states". Because of the presence of a huge number of competing phases, defining the exact ground states is very difficult, but this observation accords with the experimental observation of atomic-level mixing of Fe and Au in nanostripes on Mo(110) [163], but the absence of long-range order.

Chapter 6

Frenkel-Kontorova model for heteroepitaxial systems: O/Ru(0001)

6.1 Introduction

In the last three chapters, we have considered surface alloy systems in which mixing between two metals on a third metal was studied in detail. However, recall that we have always assumed that an overlayer (whether a single-component or an alloy) is pseudomorphic with the substrate, which in actual experimental conditions need not be true. In this chapter, we have studied whether single-component overlayers (O = Fe, Co, Pt, Ag, Au, and Pb) on the Ru(0001) surface would reconstruct or not, using the Frenkel-Kontorova model. This study is complementary to our work on $M_xN_{(1-x)}$/Ru(0001), and would enable us to check whether our assumption of pseudomorphic

layers is valid. In that study, we had considered that the reduction of the surface stress occurs by mixing, and neglected other possibilities such as surface reconstruction and dislocation formation [169]. Note that we have not considered here the Cd/Ru(0001) system, because the known toxicity of Cd made it not a good choice from the application point of view.

Surface reconstruction is a change in the positions of the atoms in the topmost layers such that the surface unit cell is no longer the same as that of the ideal-bulk truncated surface. A famous example is the herringbone reconstruction of the Au(111) surface [170–172]. Often, the main driving force for the reconstruction is the surface stress, which is usually compressive for homoepitaxial systems. For heteroepitaxial systems, the atomic-size mismatch between the substrate and the overlayer atoms can lead to either compressive or tensile stress, which can result in reconstruction of the overlayer. Depending on the sign of the stress, the reconstructed overlayer will have either increased or reduced density of overlayer atoms as compared to the substrate. Different types of reconstructions have been observed such as stripes, triangles and rotated domains [173].

In many systems, the reconstructed surface has a long-range order which provides a periodic potential for the growth of nanoislands [4], molecular assemblies [5], etc. In some cases, the small mismatch between the overlayer and the substrate leads to either incommensuration or large-period commensuration. This leads to very large system sizes, and hence these systems cannot be handled by DFT. The Frenkel-Kontorova (FK) model [174] is a simple classical model which can be used to study the surface structure and various interactions at the surface. It has been extensively used to study

the surface reconstruction in homoepitaxial systems [126, 127, 175–178] as well as for some heteroepitaxial systems [128, 129]. The model is discussed in detail in Section 6.2.

6.2 Frenkel-Kontorova Model

The model Hamiltonian can be written as,

$$H = \sum_i V_{OO}(l_i) + \sum_j V_{OS}(\mathbf{r}_j) + \sum_j \Gamma, \tag{6.1}$$

where the first term denotes the interaction between the overlayer atoms and the sum is over all the nearest neighbor bonds of length l_i; the second term is the substrate potential experienced by overlayer atoms and the sum is taken over all overlayer atoms at positions $\mathbf{r}_j$; and the third term accounts for the extra energy required to change the number of atoms in the overlayer. Γ is usually referred as the "chemical potential", however it consists of two terms – one is the energy cost for adding (removing) atoms to (from) the overlayer, and the second is the energy required to form (break) new bonds when extra atoms are added to (removed from) the surface [175]. It is actually related to the negative of the chemical potential; however, in papers in this field, it has been conventional to refer to it as the chemical potential, and in this chapter we will maintain this convention. Here, the addition of an atom leads to compressive reconstruction, and the removal of an atom leads to expansive reconstruction. Therefore, this simple model can take into account different competing mechanisms which result in surface reconstruction. There are two

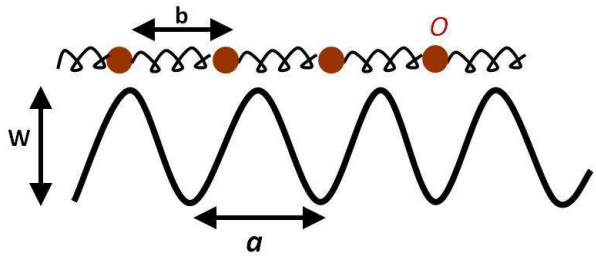

Figure 6.1: *Schematic diagram showing various surface interactions considered in the Frenkel-Kontorova model: The substrate potential is modeled by a sinusoidal potential with a period of a and depth of W, and the overlayer atoms O shown by brown spheres are connected by harmonic springs with an equilibrium length of b and a spring constant μ.*

approaches used for obtaining solutions for any system – first, consideration of a simple parameter obtained by mapping a two-dimensional (2D) surface on to a one-dimensional (1D) chain, and second, complete quenched molecular dynamics (QMD) simulations for a 2D Hamiltonian. The first approach has primarily been used for homoepitaxial systems, whereas QMD simulations can be performed for both homoepitaxial and heteroepitaxial systems. I will describe and compare both these approaches in the following sections.

6.2.1 One-dimensional Frenkel-Kontorova Model

In its simple 1D form, the model considers a chain of atoms sitting in a periodic potential. The schematic figure depicting the different interactions present in the 1D model is shown in Fig. 6.1. The 1D chain consists of overlayer atoms O which are connected by harmonic springs with equilibrium bond length b and spring constant μ. A periodic potential describing the substrate is modeled by a sinusoidal potential having period a and amplitude W. As $a \neq b$ in general, the model can take into account two competing

periodicities present at the surface. Depending on the relative strengths of the depth of the substrate potential and the stiffness of the springs, solutions of the system can vary from pseudomorphic (in which overlayer atoms sit exactly in the valleys of the substrate potential) to having dislocation lines which are periodically spaced. The latter solution corresponds to stable surface reconstructions. Note that real surfaces are 2D and so such an approach may not work for all systems.

Mansfield and Needs [175] mapped the fcc(111) surface onto such a 1D model, and derived an expression for a simple dimensionless parameter R, which is given by,

$$R = \frac{\sqrt{3}\pi a(\gamma - \frac{4}{3}\sigma)}{8\sqrt{\mu W}}, \tag{6.2}$$

where σ and γ denote the surface stress and the surface energy of the substrate. Depending on the value of R, one can estimate whether the given system will reconstruct or not, and its sign will tell whether the overlayer would compress or stretch. If $|R| < 1$, then the system prefers pseudomorphic positions over the reconstruction. If $R <$ -1, then there will be a compressive reconstruction, that is, the average distance between overlayer atoms will be reduced, so as to have a larger density than that of the topmost substrate layer; and if $R > 1$, the system will have an expansive reconstruction, that is, the density of overlayer atoms will be smaller than those of atoms in the topmost substrate layer. This simple indicator is shown to work well for the fcc(111) surfaces [126, 178], for which mapping to the 1D chain is shown in Fig. 6.2. The mapping is done along a zig-zag path that connects low-energy sites on the surface. All the different physical quantities required to compute

R can be calculated using DFT.

Till now, the R parameter has only been applied to homoepitaxial systems. We generalize it for heteroepitaxial cases by replacing the surface energy γ by an interface energy γ_i. The interface energy is the energy required to deposit a single pseudomorphic layer of O on the substrate, defined by:

$$\gamma_i = \frac{E_{slab} - N^O E^O_{bulk} - N^S E^S_{bulk}}{2A}, \tag{6.3}$$

where E_{slab} is the total energy of the slab containing N atoms and having surface area A, the overlayer is deposited on both sides of the slab. N_O and N_S are, respectively the total number of overlayer and substrate atoms in the slab, and E^O_{bulk} and E^S_{bulk} are the total energies per atom of the overlayer and the substrate in their bulk phases respectively. The interface energy consists of two contributions, one coming from having overlayer atoms forming the surface, and the second from stretching or compressing this "surface" to the substrate lattice constant. In this work, we have examined whether this extension can reliably predict the presence or absence of surface reconstruction.

6.2.2 Two-dimensional Frenkel-Kontorova Model

We have simulated a complete two-dimensional form of the FK model by considering realistic forms of the substrate potential and the interatomic potential between overlayer atoms. The first term in Eq. (6.1), that is, the interaction between overlayer atoms, V_{OO}, is described by a Morse potential of the form:

$$V_{ij}(r_{ij}) = A^{ij}_0 (1 - e^{-A^{ij}_1 (r - b^{ij})})^2, \tag{6.4}$$

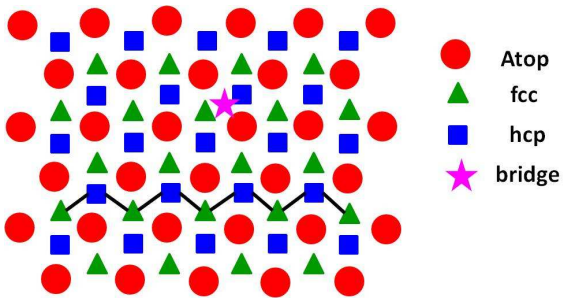

Figure 6.2: *Schematic diagram showing different stacking sites possible for the hcp(0001) surface: a top view of the hcp(0001) surface where red circles represent atoms in the first layer, and blue squares in the second layer. Red circles show atop sites, green triangles show fcc sites, blue squares show hcp sites, and only one of the bridge sites is shown with a star. The black zig-zag line connecting the fcc sites to the hcp sites via bridge positions shows the line considered for 1D mapping of the closed-packed surface.*

where r_{ij} is the distance between the NN atoms i and j, b^{ij} is the equilibrium bond length, and A_0^{ij} and A_1^{ij} are the parameters associated with the depth and width of the potential well respectively. To get the Morse parameters, we have followed the same procedure as was described in Chapter 3 with a few slight changes described later in this chapter.

The second term in Eq. (6.1), the substrate potential V_{OS} at any point (x, y) on the surface, can be obtained by Fourier interpolation between the values of different stacking site energies. An hcp(0001) surface has a triangular lattice. Four of the different stacking sites possible for a triangular lattice are fcc, hcp, atop and bridge sites; these are shown schematically in Fig. 6.2.

The substrate potential is given by:

$$
\begin{aligned}
V_{OS}(x,y) = \frac{V_B + 3V_P}{4} &+ \left(\frac{2V_B - V_A - V_C}{9}\right) \times \\
&\left\{\cos\left[\frac{2\pi}{a}\left(x - \frac{y}{\sqrt{3}}\right)\right] + \cos\left[\frac{4\pi}{\sqrt{3}a}y\right] + \cos\left[\frac{2\pi}{a}\left(x + \frac{y}{\sqrt{3}}\right)\right]\right\} \\
&- \left(\frac{V_C - V_A}{3\sqrt{3}}\right) \times \\
&\left\{\sin\left[\frac{2\pi}{a}\left(x - \frac{y}{\sqrt{3}}\right)\right] + \sin\left[\frac{4\pi}{\sqrt{3}a}y\right] - \sin\left[\frac{2\pi}{a}\left(x + \frac{y}{\sqrt{3}}\right)\right]\right\} \\
&+ \left(\frac{V_B - 9V_P + 4V_A + 4V_C}{36}\right) \times \\
&\left\{\cos\left[\frac{4\pi}{a}x\right] + \cos\left[\frac{2\pi}{a}\left(x + \sqrt{3}y\right)\right] + \cos\left[\frac{2\pi}{a}\left(-x + \sqrt{3}y\right)\right]\right\}.
\end{aligned}
\tag{6.5}
$$

In this equation, V_C, V_A, V_B and V_P denote the stacking site energies for fcc, hcp, atop and bridge sites, respectively.

The third term in Eq. (6.1), referred as the "chemical potential", is more difficult to define for heteroepitaxial systems. While mapping to the 1D model, it was assumed that the extra atoms needed to increase the density of overlayer atoms (for a compressive reconstruction) come from the bulk phase. This may not be true in actual experimental conditions, where extra atoms can be obtained from adatoms or step-edges with smaller energy cost. In the case of heteroepitaxial systems, there is no accessible "bulk" phase for overlayer atoms. In the case of expansive reconstructions, the source would be replaced by a sink for the atoms removed from the overlayer.

In previous studies done on heteroepitaxial systems, there have been a number of different approaches used. A few such choices are to set Γ to a

value such that the model results match known results [176] or to take Γ to be equal to the cohesive energy per atom in the monolayer with bulk lattice spacing [128], or the energy cost to take a single adatom at equilibrium on the surface [179], or set it to zero [180]. To study surface alloying of two elements on a third one, the formation energy has been used in the place of Γ [181], which ignores the origin of atomic reservoirs. For the Pt(111) surface, it has been shown that depending on whether the extra atoms come from the bulk or the adatoms, the tendency towards reconstruction alters [126]. Therefore in this work, we have have considered two different cases – (i) consider that the extra atoms originate from the bulk phase, that is, the same assumption used for the 1D model, and (ii) consider Γ to be a free parameter and see its effect on each system. The previous case would be useful for the direct comparison between results from the 1D and the 2D models, and the latter would be useful to tune the periodicity of reconstruction.

We will also examine whether it is possible to control the formation of the reconstruction by tuning the chemical potential. There have been some theoretical and experimental studies which show that varying physical conditions can affect the surface structure [182–185]. In this study, we have assumed that the overlayer reconstructs by densifying or rarefying along only one direction. This is a generally observed structure for reconstructions of a single monolayer of overlayer atoms. We would expect qualitatively similar behavior for other types of reconstructions such as isotropic triangular patterns.

6.3 Computational Details

We have used the PWscf code of the Quantum-ESPRESSO package [29] to perform density functional theory calculations to compute the various parameters required to solve the Frenkel-Kontorova model. For magnetic overlayer systems, that is, for Fe or Co on Ru(0001), we have performed spin polarized calculations. We have used a plane-wave basis set along with ultrasoft pseudopotentials [18]. We have used a generalized gradient approximation of the Perdew-Burke-Ernzerhof form [11] for the exchange-correlation functional. The plane-wave cutoff energies for wavefunctions and charge densities are equal to 20 Ry and 160 Ry respectively.

A supercell approach is used to model the surface within periodic boundary conditions. The calculations to get energetics of different stacking possibilities were performed using an asymmetric slab containing six Ru layers, one pseudomorphic O overlayer, and vacuum spacing of around 17.4 Å. The surface normal (the z-direction) is along the [0001] crystallographic direction. We have allowed the overlayer and three adjacent Ru layers to relax using Hellmann-Feynman forces, while the three bottom layers are kept fixed. The calculations done to determine the Morse parameters were done using a symmetric slab with an overlayer deposited on both sides of a six-layer Ru slab. For these calculations, only the overlayer is allowed to relax, and all the Ru layers are fixed at the bulk distance. We have used an (8×8) Monkhorst-Pack k-mesh [19] in the surface Brillouin zone. For better convergence, we have used the Methfessel-Paxton smearing technique [22], with the smearing width equal to 0.05 Ry.

We have performed quenched molecular dynamics simulations to solve the 2D Hamiltonian given in Eq. (6.1). Based on atomic-size mismatch between the overlayer atoms and the substrate, we have modeled compressive reconstruction for the Fe and Co overlayers, and expansive reconstruction for the Pt, Ag, Au and Pb overlayers.

6.4 Results and Discussion

6.4.1 One-dimensional Frenkel-Kontorova Model

The value of the period of the substrate potential, a, is equal to the NN distance of Ru. The calculated value of a is equal to 2.74 Å, as was reported in Chapter 3. Next, we have calculated the stacking fault energies for four different stacking sites (see Fig. 6.2). Note that to calculate the bridge site energies, relaxation of overlayer atoms in the surface plane is not permitted, so as to ensure that the system does not relax to a minimum energy position rather than the needed saddle point configuration. The energies are tabulated in Table 6.1; the values are given relative to the most stable site for that overlayer system, so for Fe, Co, and Pt with respect to the hcp site, and for Ag, Au, and Pb with respect to the fcc site. The atop sites are the least favored, whereas hollow sites (fcc or hcp) are the most favored sites. The amplitude of the substrate potential along the zig-zag line connecting hcp and fcc sites (see Fig. 6.2), is given by the energy difference between the energy of the bridge site and the most favored site, V_{min}, that is, $W = |V_P - V_{min}|$. The values are tabulated in Table 6.2.

Overlayer element O	Stacking fault energies (meV)				Morse potential parameters		
	V_A hcp	V_B atop	V_C fcc	V_P bridge	A_0 (eV)	A_1 (Å^{-1})	b (Å)
Fe	0.0	541.5	55.9	79.8	1.4111	0.997	2.65
Co	0.0	563.5	88.1	217.6	1.0608	1.450	2.52
Pt	0.0	178.3	3.8	112.7	1.1061	1.656	2.78
Ag	4.9	268.6	0.0	58.3	0.5449	1.588	2.89
Au	7.3	195.9	0.0	54.1	0.7165	1.684	2.86
Pb	1.8	202.0	0.0	36.7	0.6706	1.336	3.26

Table 6.1: *The calculated stacking fault energies for four different stacking sites and the fitted Morse parameters, for overlayer O atoms on the Ru(0001) surface are tabulated. The stacking site energies are given relative to the lowest energy site for that particular system.*

To determine the interactions between overlayer atoms V_{OO} for the 2D model and the spring constant μ for the 1D model, we have assumed that the NN bond has a Morse potential form. We have calculated the corresponding Morse parameters using the same procedure which has been described in Chapter 3, that is, to fit a plot of the surface stress versus the in-plane lattice constant to a derivative of a Morse form. There is a slight variation in the procedure to calculate the stress – in the previous chapter, we allowed the interlayer distance between the overlayer and the substrate to relax as we varied the in-plane distance, while here we have kept it fixed at the value corresponding to the substrate lattice constant. (In reality, we are interested in the surface stress when only the overlayer is stretched or compressed, and not the complete slab. In this case, the interplanar distance between the overlayer and the substrate would have an intermediate value between the value it has at the substrate lattice constant and the one when the complete slab is stretched or compressed pseudomorphically. Therefore, these two

O	γ_i	σ	μ	W	R
Fe	0.196	0.139	2.801	0.080	0.04
Co	0.181	0.396	4.464	0.218	-0.66
Pt	0.100	-0.138	6.068	0.113	0.64
Ag	0.146	-0.371	2.748	0.058	2.99
Au	0.120	-0.424	4.064	0.054	2.73
Pb	0.380	-2.212	2.394	0.037	21.0

Table 6.2: *Calculated quantities required to evaluate the reconstruction parameter R and the corresponding values of R: The interface energy γ_i, the surface stress σ, and the spring constant μ are in $eV/\AA^2$ and the amplitude of the substrate potential W is given in eV. The R-parameter is a dimensionless quantity.*

approaches may be considered as two limiting cases for the actual value we need to compute. One might then expect that the actual values of the stiffness and equilibrium bond length of the intraplanar overlayer bonds also will have intermediate values between the two limiting cases.) The calculated values of A_0, A_1 and b are tabulated in Table 6.1, and the calculated surface stress at the Ru bulk NN spacing and the values of spring constant μ ($= 2A_0A_1^2$) are given in Table 6.2. Note that the values of the surface stress are the same as those shown in Fig. 3.15. However, in that chapter we had used the convention that positive (negative) sign denotes compressive (tensile) stress, while in the derivation of R [175], the opposite sign convention has been used. Therefore to be consistent with the derivation, we have considered here a positive (negative) sign for the tensile (compressive) stress.

Now the only remaining quantity required to compute R is the interface energy which is defined by Eq. (6.3). These calculations were done using a symmetric slab, and the values are tabulated in Table 6.2.

After computing all the different quantities required, we have calculated the R-parameter for all the systems. The values are given in the last column

of Table 6.2. For the monolayers of Fe, Co and Pt on the Ru(0001) surface, we find that $|R| < 1$, which implies that there is no reconstruction for these systems, whereas for the monolayers of Ag, Au and Pb on Ru(0001), we obtain $|R| > 1$, which means that these overlayers would reconstruct. These results match with experimental results whenever available (see Table 6.4). Note here that just examining the various parameters in columns 2-5 of Table 6.2 will not be sufficient to give us an idea about reconstructions. For example, for Co/Ru(0001), the surface stress and the spring stiffness are higher than those for Ag/Ru(0001) which would suggest that the Co overlayer would reconstruct, but Ag would not. However, this is opposite to what is observed. This is because in the case of Co/Ru(0001), the substrate potential is much deeper than that for Ag/Ru(0001), which compensates for the other two effects.

Based on the atomic-size mismatch between O and Ru, one expects Fe and Co to have negative R values, but Pt, Ag, Au and Pb to have positive R values. Except for Fe/Ru(0001), this is true for all the systems studied. Note that for Fe/Ru(0001), the values of V_C and V_P are very close to each other as compared to other systems. This breaks the assumption of sinusoidal potential which is valid if $V_P - V_A >> |V_C - V_A|$. This may lead to the slight discrepancy from expectations, observed for this particular system. For the Pb/Ru(0001) system, the value of R is very large which indicates a strong tendency towards reconstruction. This corresponds with the very large atomic-size mismatch between the Pb and Ru atoms.

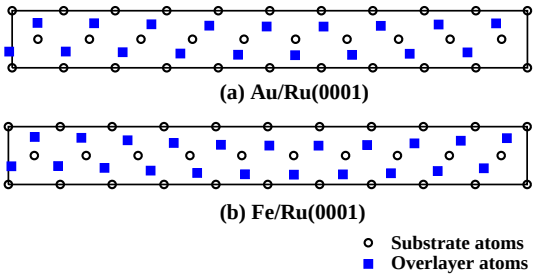

Figure 6.3: *Examples of surface unit cells used for simulation of the 2D FK model: show top views of an* $(n \times \sqrt{3})$ *surface unit cell with* $n = 10$*. The black circles denote underlying substrate atoms. The blue squares represent the optimized final positions for overlayer elements – (a) Au/Ru(0001) having* $n - 1 = 9$ *atoms in a row (expansive reconstruction), and (b) Fe/Ru(0001) having* $n+1 = 11$ *atoms in a row (compressive reconstruction).*

6.4.2 Two-dimensional Frenkel-Kontorova Model

Next we will simulate the complete 2D FK model for all the systems considered above. For these simulations, we have considered an $(n \times \sqrt{3})$ unit cell (an example is shown in Fig. 6.3) which contains $2n$ atoms for the pseudomorphic overlayer configuration. For compressive (expansive) reconstruction, there is an increase (decrease) in the density of overlayer atoms, that is, the unit cell would contain $(2n + 2)$ [or$(2n - 2)$] atoms; an example of each type of reconstructed unit cell is shown in Fig. 6.3. We start with various initial positions for these $(2n \pm 2)$ atoms, and then these positions are optimized using a conjugate gradient algorithm to obtain the minimum energy configuration. To ensure that we have indeed reached a global minimum, we start with a few different initial atomic positions.

Before we start our study, we need to define the chemical potential. As

O	Γ_b (eV)	E_c (eV)	E_{ad} (eV/atom)	Γ_{ad} (eV)
Fe	1.24	5.28	-4.02	-0.03
Co	0.94	5.54	-4.42	-0.18
Pt	0.64	5.72	-3.75	-1.33
Ag	0.83	2.51	-1.39	-0.29
Au	0.67	2.98	-1.43	-0.88
Pb	0.50	2.93	-	-

Table 6.3: *The ab initio values of cohesive energies E_c , the adsorption energies E_{ad} for adatoms on the heteroepitaxial systems, and values of chemical potential obtained from the bulk Γ_b and the adatoms Γ_{ad}, are tabulated here.*

mentioned before, we have first considered the bulk phase as the source or sink for "extra" atoms. We need to find the chemical potential associated with the bulk phase of overlayer atoms. Note that the interface energy γ_i for the unreconstructed overlayer can be calculated in two ways – (i) from *ab initio* calculations as was done using Eq. (6.3), and (ii) from the FK model Hamiltonian which gives us,

$$\gamma_i = \frac{3E_0 + \Gamma_b}{\frac{\sqrt{3}}{2}a^2}, \tag{6.6}$$

where E_0 is the elastic energy for the NN bond of an atom in the unreconstructed overlayer which is given by $E_0 = A_0\{1 - e^{-A_1(a-b)}\}^2$, and Γ_b is the "bulk" chemical potential. Therefore, we can compute the "bulk" chemical potential:

$$\Gamma_b = \frac{\sqrt{3}a^2\gamma_i}{2} - 3E_0, \tag{6.7}$$

using the *ab initio* calculated interface energies. The computed values of Γ_b are tabulated in Table 6.3.

After defining the chemical potential, we compare the energies of the

reconstructed overlayer with that of the unreconstructed overlayer, to see whether the reconstruction is favored or not. We define the quantity:

$$\Delta\gamma(n) = \frac{E_{rec}(n) - E_{unrecon}(n)}{\sqrt{3}na^2}, \tag{6.8}$$

where $E_{rec}(n)$ is the energy of a reconstructed overlayer [having overlayer density $(n+1)/n$ for compressive reconstruction and $(n-1)/n$ for expansive reconstruction], while $E_{unrec}(n)$ is the energy of an unreconstructed surface [with density $= n/n = 1$]. The energies are minimized for an $(n \times \sqrt{3})$ unit cell, with area $= \sqrt{3}na^2$.

In Fig. 6.4, we have shown our results for $\Delta\gamma$, taking chemical potential Γ equal to Γ_b, as a function of the change in the density of the overlayer atoms relative to the substrate. We have plotted using $\Delta\rho = \pm\frac{1}{n}$ as the abscissas rather than n. Note that $\Delta\rho$ is positive for compressive reconstruction and negative for expansive reconstruction. If $\Delta\gamma(n)$ is negative, then reconstruction is favored over the pseudomorphic structure, and a minimum at a finite value of $n = n^*$ gives the periodicity of reconstruction for the reconstructed surface. We observe that Au, Ag, and Pb overlayers prefer to reconstruct, whereas Pt, Co, and Fe overlayers do not reconstruct. For Au/Ru(0001), the energy cost to reconstruct is minimum when $\Delta\rho_{min} \sim$ -8.33%, which corresponds to $n = 12$, i.e., 11 Au atoms on 12 Ru atoms. Similarly, for Ag/Ru(0001), the energy cost to reconstruct is minimum when 7 Ag atoms sit on 8 Ru atoms, that is, $\Delta\rho_{min} =$ -12.5%. For Pb/Ru(0001), a minimum is obtained for 2 Pb atoms on 3 Ru atoms which corresponds to $\Delta\rho_{min} =$ -33%.

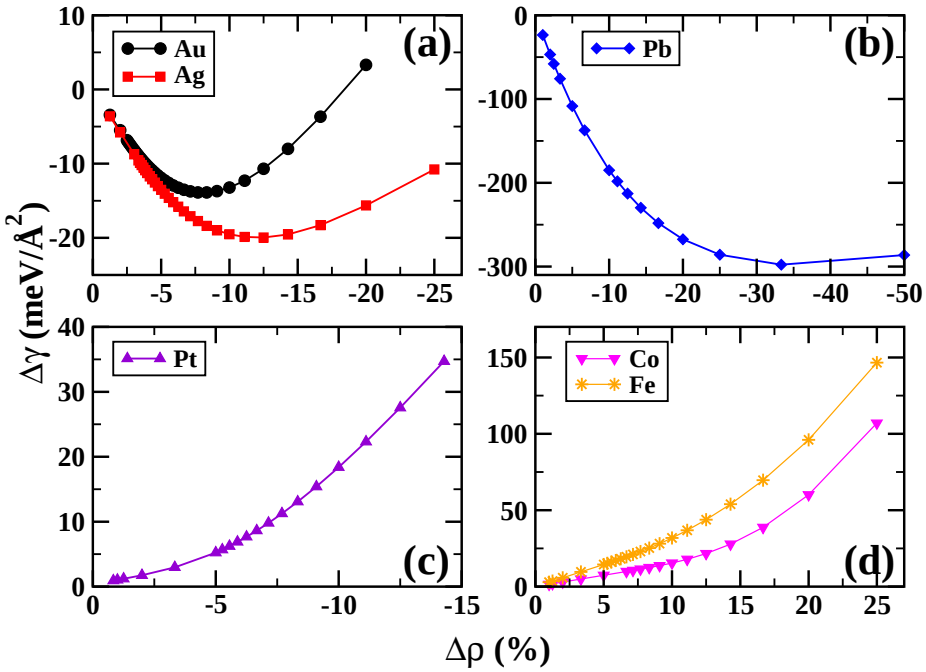

Figure 6.4: *The difference in surface energy per unit area of the reconstructed and the unreconstructed surface, $\Delta\gamma$, as a function of the change in the density of overlayer atoms, $\Delta\rho$, calculated using the 2D Frenkel-Kontorova model: these were obtained by taking $\Gamma = \Gamma_b$. We have shown results for (a) Ag and Au, (b) Pb, (c) Pt, and (d) Fe and Co. Note that the y-axis scale is different for each panel.*

Note that the gain in energy upon reconstruction is much larger for this system as compared to the Ag or Au overlayers, this is because of the very large tensile stress present in the pseudomorphic Pb/Ru(0001). We observe that there is a monotonic relationship between the value of $|R|$ obtained using the 1D FK model and $|\Delta\rho_{min}|$ obtained from the 2D FK model, since R serves as a measure of the tendency toward reconstruction when $\Gamma = \Gamma_b$.

As we have already explained, for heteroepitaxial systems, the chemical potential from the bulk phases may not be the correct parameter to use. So

we estimate the chemical potential if the source or sink for extra atoms is considered to be adatoms on the O/Ru(0001) system. The values of chemical potential can be estimated using the relation:

$$\Gamma_{ad} = \Gamma_b - E_c - E_{ad}. \tag{6.9}$$

Here, E_c is the cohesive energy which is defined as the difference between the energy per atom in the gas phase (that is, an isolated atom), $E(O_{iso})$, and in the bulk phase, E_{bulk}. The adsorption energy E_{ad} for an adatom on O/Ru(0001) is defined as $E_{ad} = E(O_{ad}/O/\text{Ru}(0001)) - E(O/\text{Ru}(0001)) - E(O_{iso})$, where $E(O_{ad}/O/\text{Ru}(0001))$ is the total energy for an adatom adsorbed on the O/Ru(0001) surface, and $E(O/\text{Ru}(0001))$ is the total energy for the pseudomorphic overlayer of O on the Ru(0001) surface. For the adatom calculation, we have used a (3×3) O/Ru(0001) surface unit cell. The computed values of E_c, E_{ad} and Γ_{ad} are tabulated in Table 6.3, for all the systems except Pb/Ru(0001). For the Pb/Ru(0001) system, when a Pb adatom is adsorbed, we find that the whole system reconstructs, and we were not able to get a stable geometry. The probable reason for this instability is the high compressive stress for Pb/Ru(0001). Note that for all the systems, Γ_b is positive, whereas Γ_{ad} is negative.

Next, we will examine how the reconstruction is affected when the chemical potential Γ is varied. The values of Γ are chosen in the vicinity of Γ_b and Γ_{ad} to ensure that the values are reasonable for experimental conditions. For all the systems under study, we have computed the difference in surface energy between the reconstructed and unreconstructed surface, $\Delta\gamma$, as

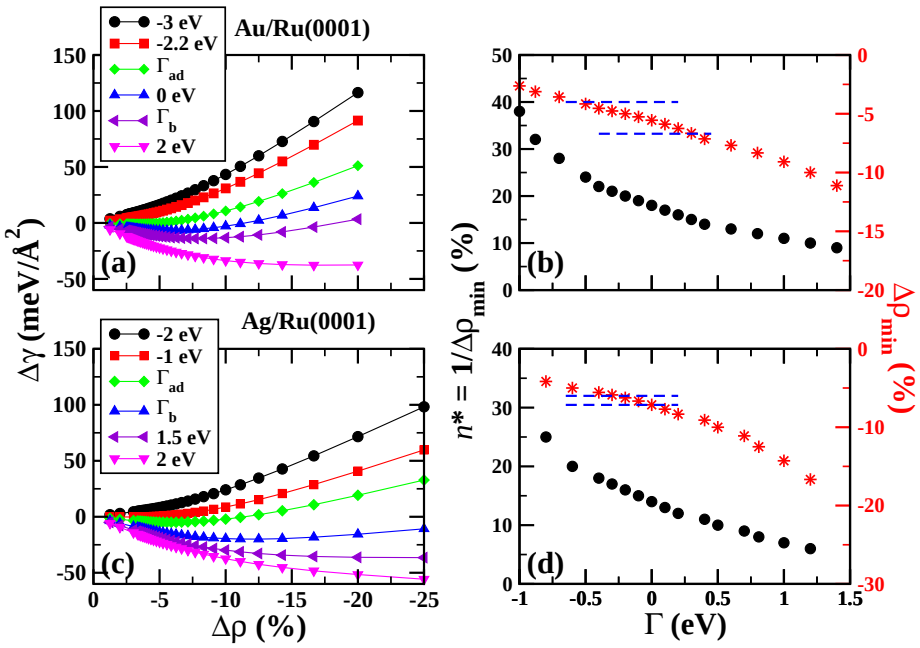

Figure 6.5: *Controlling surface reconstruction by varying the chemical potential for Ag/Ru(0001) and Au/Ru(0001): the difference in the surface energy between the reconstructed and unreconstructed surfaces, as a function of the change in the density of overlayer atoms, for (a) Au/Ru(0001) and (c) Ag/Ru(0001), is plotted for different values of* Γ*. The values of* Γ_b *and* Γ_{ad}*, for both the systems, are given in Table 6.3. In panels (b) and (d), we have plotted the optimal values of the period of reconstruction,* n^* *(black circles), and the decrease in density* $\Delta\rho_{min}$ *(red stars), as a function of* Γ*, for Au and Ag respectively. The blue dashed lines correspond to the experimentally observed range of* $\Delta\rho_{min}$ *values.*

a function of the change in the density of overlayer atoms relative to the substrate, $\Delta\rho$, at different values of Γ. The plots are shown in Figs. 6.5-6.7. We have found that, for all the systems under study, the behavior can smoothly be switched from unreconstructed to reconstructed by changing the chemical potential values. Note that the effect of a change in Γ is opposite for compressive and expansive reconstructions. For compressive reconstructions, a positive value of the chemical potential indicates that an extra atom required

for the overlayer to reconstruct costs higher energy, and thus the compressive reconstruction is less favored. In contrast, for expansive reconstructions, a positive value of Γ would favor reconstruction because it costs less energy to give away an extra atom. Therefore, for Fe/Ru(0001) and Co/Ru(0001), as Γ becomes more positive it is less favorable for the overlayer to reconstruct, and larger n and smaller $|\Delta\rho|$ values are observed. However, for Pt/Ru(0001), Ag/Ru(0001), Au/Ru(0001), and Pb/Ru(0001), as Γ becomes more positive, expansive reconstruction becomes more favorable, and smaller n and larger $|\Delta\rho|$ are favored. In growth experiments for heteroepitaxial systems, one can tune the chemical potential by controlling temperature, the metal deposition flux, or the adatom density in ultra-high vacuum conditions [186, 187], and for chemical growth, by controlling the electrochemical potential, and concentration [188–190].

In Fig. 6.5(a) and Fig. 6.5(c), we have shown the results for Au/Ru(0001) and Ag/Ru(0001) respectively. For both these systems, at very negative values of Γ, $\Delta\gamma$ is positive and does not show a minimum, which implies that the pseudomorphic overlayer is favored. As Γ increases, the reconstruction starts becoming favorable. For both these systems, around $\Gamma = \Gamma_{ad}$ (-0.9 eV for Au and -0.3 eV for Ag), $\Delta\gamma$ becomes negative and the reconstruction is favored. At the Γ_{ad} value, for Au/Ru(0001), a minimum in $\Delta\gamma$ occurs when $\Delta\rho_{min}$ = -3.12%, which corresponds to 31 gold atoms on 32 Ru atoms, and for Ag/Ru(0001), $\Delta\rho_{min}$ = -5.88%, which corresponds to 16 silver atoms on 17 Ru atoms.

There is lot of experimental data available for both these systems, so we will now examine how our results compare with the experimental data. In

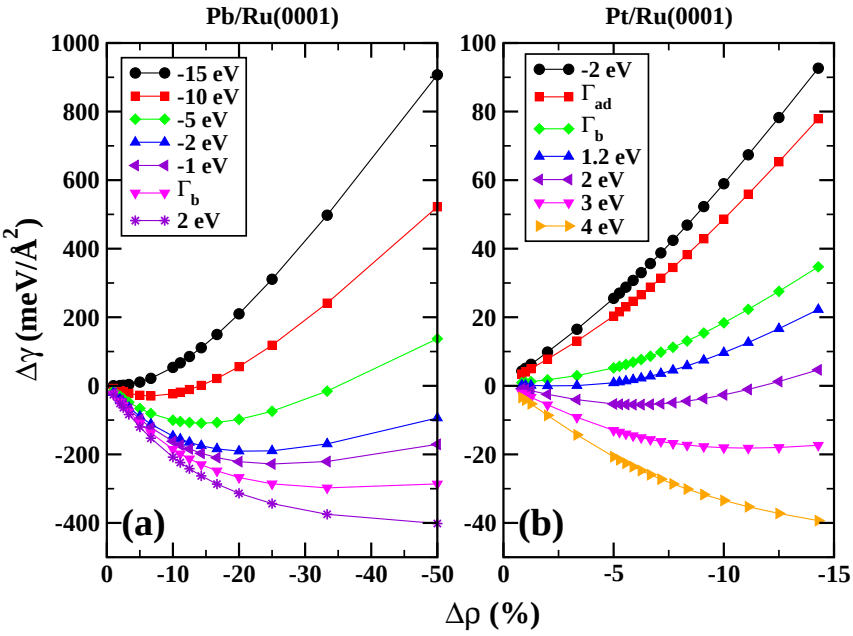

Figure 6.6: *Controlling surface reconstruction by varying the chemical potential for (a) Pb/Ru(0001) and (b) Pt/Ru(0001): change in the surface energy $\Delta\gamma$ as a function of reduced density of overlayer atoms, $\Delta\rho$, is plotted at different values of Γ. The values of Γ_b and Γ_{ad} for both the systems are given in Table 6.3. Note that the y-axis scales in the two panels differ by an order of magnitude.*

Fig. 6.5(b) and Fig. 6.5(d), we have plotted n^* and $\Delta\rho_{min}$ as a function of the chemical potential Γ. We have shown the experimental data with blue dashed lines, which show a range of $\Delta\rho_{min}$ observed in STM experiments – for Au/Ru(0001), the reported periodicity for the stripe width is 6.8 nm [107], corresponding to $\Delta\rho_{min}$ = -4%, while in the group of S. Rousset, *et al.*, they have observed a periodicity of 4 nm, which corresponds to $\Delta\rho_{min}$ = -6.7% [unpublished]. For Ag/Ru(0001), reported periodicities are 3.8 nm [107] and 4.3 nm [108], which correspond to $\Delta\rho_{min}$ values of -7.14% and -6.25% respectively. These values correspond to Γ values of -0.5 to 0.3 eV for Au/Ru(0001)

and -0.20 to 0.01 eV for Ag/Ru(0001). Recall that the values for Γ_b and Γ_{ad} values for Au are equal to 0.67 eV and -0.88 eV respectively, and for Ag, 0.83 eV and -0.29 eV respectively. Therefore, our results using the FK model are comparable with those from experiments.

In Fig. 6.6, we have shown similar results for Pb/Ru(0001) and Pt/Ru(0001). For Pb/Ru(0001), the system prefers to reconstruct until Γ values become very strongly negative. At all physically relevant values of Γ, we have obtained negative $\Delta\gamma$ values with sharp minima. This is expected based on the large surface stress value computed for this system, implying that a pseudomorphic overlayer costs a very high elastic energy. This observation also accords with the large R value obtained from the 1D model. For Pt/Ru(0001), for both $\Gamma = \Gamma_b$ and $\Gamma = \Gamma_{ad}$, the system prefers to remain pseudomorphic. Only at high Γ values (> 1.2 eV), is reconstruction more favored as compared to the pseudomorphic layer.

In Fig. 6.7, we have shown our results for Fe/Ru(0001) and Co/Ru(0001), to see the effect of varying chemical potential. For both these systems, at low negative values of Γ, we get negative $\Delta\gamma$ values, indicating that reconstruction is favored. For Co/Ru(0001), when $\Gamma \gtrsim 0$ eV, there is no reconstruction, and for Fe/Ru(0001), no reconstruction is observed when $\Gamma \gtrsim$ -1 eV.

6.4.3 Comparison with Experiments and our Previous Work

In Table 6.4, we have compared our results from the 1D model and the 2D model with each other, and with experiments. The predictions from the 1D

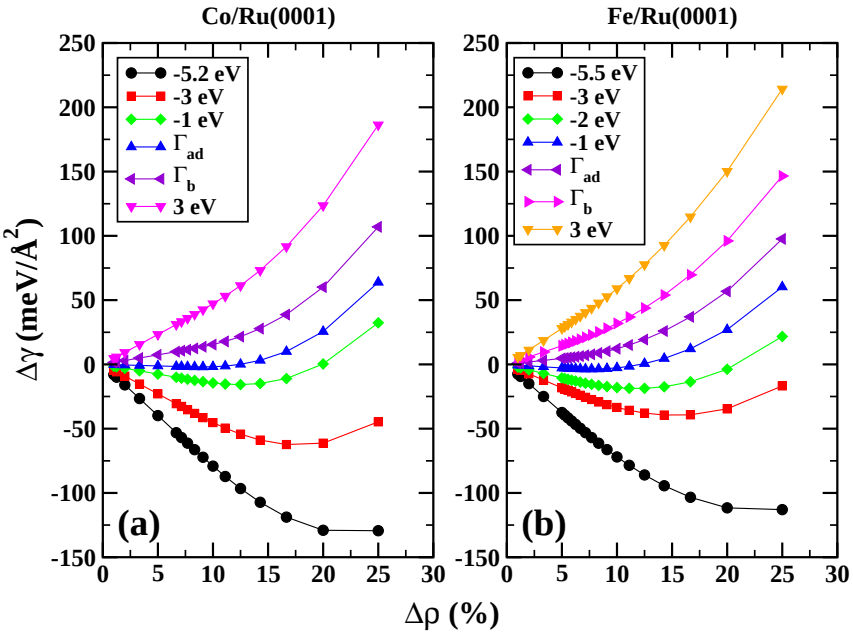

Figure 6.7: *Controlling surface reconstruction by varying the chemical potential: change in the surface energy $\Delta\gamma$, as a function of increased density of overlayer atoms, $\Delta\rho$, for (a) Co/Ru(0001) and (b) Fe/Ru(0001), for varying values of chemical potential Γ. The values of Γ_b and Γ_{ad} for Fe and Co are given in Table 6.3.*

model are based on the value of R, and the predictions from the 2D model are based on simulations done at $\Gamma = \Gamma_b$, which is the appropriate value to compare with the R-parameter. We observe that the results from the two approaches match with each other. In the last column, we have also tabulated whether the overlayer is observed to reconstruct in experiments. For all the systems, our results agree with experimental observations (when data is available). Though we were unable to find experimental reports of whether or not Pb/Ru(0001) reconstructs [191], it is almost certain that it will do so, given the large size mismatch between Pb and Ru, and the results of our attempted *ab initio* calculations of a single adatom on pseudomorphic

O	1D model	2D model	Experimental
Fe	No	No	No [104]
Co	No	No	No [105]
Pt	Yes	Yes	Yes [106]
Ag	Yes	Yes	Yes [78, 107, 108]
Au	Yes	Yes	Yes [107]
Pb	Yes	Yes	-

Table 6.4: *Comparison between the results from the 1D Frenkel-Kontorova model, 2D Frenkel-Kontorova model and experiments: we have tabulated our predictions of whether or not the overlayer O would reconstruct on the Ru(0001) surface. For the 2D model, the predictions are based on the simulations done at* $\Gamma = \Gamma_b$. *The reported experimental data has been taken from previous studies. Note the excellent agreement between all three columns.*

Pb/Ru(0001).

Recall that in Chapter 3, we have considered mixing of pairs of these metals on the Ru(0001) surface with the assumption of pseudomorphic overlayers. Most crucially, the energy of the mixed phase was compared with that of phase segregated pseudomorphic phases. By comparing the energy of reconstruction with the formation energy of alloys, we will get an idea whether our predictions of preferred alloying will be valid, in case one of the phase segregated components reconstructs. For this comparison, we have considered the energies calculated at the bulk chemical potential. Both the magnetic overlayers – Fe and Co, do not reconstruct, while, except for Pt, all the non-magnetic elements (Ag, Au and Pb) reconstruct. Therefore the results for M-Pt alloys will remain unchanged, while in the case of M-Ag alloys (which were already at the boundary of mixing), the reconstruction of the Ag layer implies that the mixing is even less favored. For Pb/Ru(0001), the $\Delta\gamma$ value at the minimum is about -298 meV/Å^2 which when compared

with the lowest formation energy of about -150 meV/Å^2 (see Fig. 3.8), implies that the reconstruction of the Pb layer would be energetically more favored than the mixing. It was for this reason that we did not consider the Pb systems as good candidates to observe surface alloying, despite the large values of $|\Delta H|$ obtained for Pb systems in Chapter 3. However, in the case of Au alloys, the formation energy of alloys is lower as compared to the energy of reconstruction. This is in accordance with the experimental observation (see Chapter 4) that Fe-Au/Ru(0001) forms a surface alloy.

6.5 Summary and Conclusions

In this chapter, we have studied the possibility of reconstruction for a monolayer of O (= Fe, Co, Pt, Ag, Au, and Pb) on the Ru(0001) surface using the Frenkel-Kontorova model. We have used two approaches – the 1D mapping of the model, and quenched molecular dynamics simulations to solve the 2D model. We have generalized the definition of the R-parameter to use in the heteroepitaxial systems, then shown that its predictions match well with experiments. Therefore, this extension allows us a simple way to estimate the possibility of surface reconstruction in heteroepitaxial systems. Our results from the 1D and 2D models match with each other and with the available experimental data. We were also able to show that by varying the value of chemical potential, one can tune the periodicity of reconstruction. The effect of changing Γ is found to be opposite for compressive and expansive reconstructions, that is, a positive value of Γ inclines the system towards expansive

reconstruction, but makes the system energetically less stable towards compressive reconstruction. In future work, it will be interesting to extend this to the case where the overlayer itself consists of more than one component. However, we note that the formation of surface alloys, of the kind studied in Chapters 3 and 4, usually reduces the surface stress, and therefore surface alloy systems are less likely to reconstruct than single-component overlayers.

A part of this work has been published in Ref. [147].

Chapter 7

Spin Polarized Surface States: Fe/Au(111)

7.1 Introduction

In the previous chapters, we have looked at the properties of surface alloys, now in this chapter we will study the properties of interfaces. Here we will look at the effect of an interface on the electronic properties – in particular we have studied the effect of Fe deposition on the Shockley surface state of the clean Au(111) surface.

The presence of the surface gives rise to additional states in the band structure of the solid due to symmetry breaking. These new states, known as surface states, peak near the surface and decay exponentially as one moves away from the surface (see Fig. 7.1). Within the independent electron approximation, there are two different ways in which the theory of surface states can be treated - using the nearly free-electron method, or using localized orbitals,

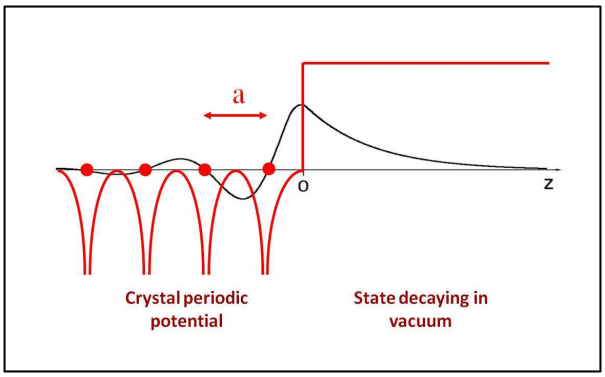

Figure 7.1: *Schematic illustration of the potential near the surface for a one-dimensional lattice and the corresponding surface state: solid circles denote the atomic positions in the lattice, the red line shows schematically the potential near the surface, and the black line shows the corresponding surface state which decays exponentially in the vacuum.*

that is, the tight-binding method [76]. The first approach is mostly used to study the surface states observed on metal surfaces which have free electron like dispersion; these are known as Shockley surface states [192]. The second approach is more suitable for semiconductor surfaces and the corresponding states are known as Tamm states [193]. Surface states of both kinds of systems can be studied using *ab initio* density functional theory. Surface states can be characterized using various experimental techniques such as angle-resolved photoemission spectroscopy, scanning tunneling microscopy (STM) and scanning tunneling spectroscopy (STS). It has been observed that surface states are sensitive to small changes in the surface structure, and hence can be used as a probe to study the presence of defects and adsorbates on the surface.

Many noble metal surfaces, for example, copper, silver, and gold, are known to have a Shockley surface state present in their band structure [194]. There have been a large number of studies on the electronic properties of

these noble metal surfaces [127, 195, 196]. The electronic properties of the Shockley state are shown to be sensitive to deposition of another metal on noble metal surfaces. For example, it has been observed experimentally that for the Au(111) and Cu(111) surfaces, the deposition of a single layer of Ag shifts the surface state band-edge by about 165 and 200 meV respectively [197]; in the same study, it has been observed that the band-edge of the Shockley state varies as a function of the Ag thickness up to about 10 ML. Buried interfaces can be detected using such thickness dependence of the surface states. Rare gas deposition is also known to cause shifts in the surface state [198, 199]. Further, surface defects such as vacancies, adsorbates, nanoislands, atomic steps, etc., can scatter the surface state electrons which then might lead to standing wave patterns [200–204]. The scattering can also induce long-range interactions which could effectively influence the growth mechanism of adsorbates [205–210]. Deposition of organic molecules can form charge-density waves in the surface state electrons, which can cause indirect interaction between adsorbates and lead to self-assembled monolayers [211]. All these different examples illustrate that the study of the electronic properties of surface states is not only important to examine changes in the surface, but can also be utilized to obtain desired properties by altering the surface environment.

Magnetic nanostructures and thin films grown on metal surfaces have shown interesting magnetic properties such as enhanced moments and high magnetic anisotropy. When a magnetic element is deposited on a noble metal surface, the presence of a two-dimensional (2D) free electron gas from the Shockley state influences its magnetic structure. For example, spin polarized

surface states originating from $d_{3z^2-r^2}$ minority and *sp* majority bands have been observed for Co nanoislands on Cu(111), and a shift in the majority state is observed as the Co coverage changes [212]. By controlling nanostructure geometry on the noble metal surfaces, the spin polarization can be tuned; the mechanism responsible for this is a local modulation of surface states and spin polarized quantum confinement [213, 214]. The existence of spin polarized surface states and quantum confinement of the surface state electrons has also been observed for Co nanoislands on the Au(111) surface [215, 216].

The Au(111) surface has been studied extensively and is known for its herringbone reconstruction [170–172]. For this surface, atoms in the surface layer occupy different crystallographic sites – mainly two regions, one with face-centered cubic (fcc) stacking and another with hexagonal closed-packed (hcp) stacking, which are separated by discommensuration lines having the bridge site stacking. Because of the symmetry of the surface, there are three different orientations possible for these striped domains; domains of two of these orientations arrange periodically in a zig-zag fashion resulting in the long-range ordered herringbone reconstruction. At the elbow of two rotated domains, there is a point defect which is known as a kink site. The regular pattern of the kink sites provides a good template for the nucleation of deposited materials, which leads to self-assembled monolayers or regularly organized nanoislands.

Our experimental collaborators – the group of S. Rousset *et al.* – have investigated the electronic properties of Fe nanoislands on Au(111), using STM and STS measurements. Using the free-electron and the tight-binding models, they have demonstrated that features in the local density of states

can be explained in terms of confined Shockley surface states [217]. Here we have studied the electronic properties of a monolayer of Fe on the Au(111) surface, and then we have compared our results with the experimental measurements. We have calculated the spin polarized band structure of the Fe-deposited surface, and have observed a large number of new states appearing in the projected bulk band gap. Only one of the new states is in the majority spin channel, while the others are in the minority spin channel. We have then analyzed our results using charge density plots and the projected density of states, to show that the state in the majority channel originates from the Shockley state on the clean surface and has similar properties to it, whereas the other states, except for one, originate from the Fe *d*-orbitals and are mostly localized on the Fe layer. We have also studied the effect of different stacking possibilities on the band structure. After we had obtained some of our results, a report was published which also studied the electronic properties of the Fe/Au(111) system [218]; we have compared our results with the reported results.

7.2 Experimental Background

Our collaborators – the group of S. Rousset, *et al.* – have performed STM and STS measurements on self-organized Fe nanoislands grown on the Au(111) surface [217]. The measurements were taken in ultra-high vacuum (pressure $\approx 10^{-10}$ mbar) and at low temperatures (5 K). The gold surface was cleaned by performing Ar^+ sputtering and then annealed by heating to temperatures of 750 K; this cycle is repeated several times to achieve a sufficiently clean

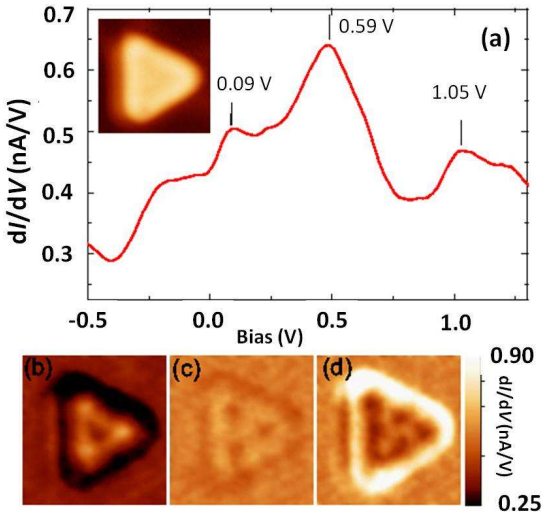

Figure 7.2: *(a) Local dI/dV spectrum measured on a Fe nanoisland on the Au(111) surface: Clear peaks are observed at the energies marked by vertical bars. The inset shows the 5.5 × 5.5 nm^2 STM image (taken at a bias of 1 V and a tip current of 500 pA) of the Fe island for which the spectrum is measured. Panels (b)-(d) show the conductance maps measured at the bias values at which peaks appear in the spectrum, that is, at 0.09 V, 0.59 V, and 1.05 V respectively [217]. The inhomogeneity in the conductance maps corresponds to the standing wave patterns of confined surface state electrons.*

surface. Iron deposition was carried out by sublimation of a Fe rod at room temperature and under ultra-high vacuum conditions. An electrochemically etched tungsten tip was used for the measurements. At low coverages, there is a formation of Fe nanoislands which nucleate at the kink sites. The islands are monatomic in height and grow pseudomorphically on the surface, in agreement with previous results [219, 220]. Most of the islands are observed to have a triangular shape or a truncated triangular shape, e.g., an STM image of a typical nanoisland is shown in the inset of Fig. 7.2(a).

The local electronic properties of the system are studied by STS measurements on several islands; one example of such a spectrum is shown in Fig. 7.2(a). The spectrum shows a number of peaks; the peak positions shift as a function of the size of the nanoisland. The conductance maps measured near these peak energies (shown in Fig. 7.2(b)-(d)) show spatial inhomogeneity in the local density of states. Using the free-electron and the tight-binding models to analyze the experimental data, it was shown that the measured spectrum can be explained in terms of the confinement of the Shockley-like surface state electrons in nanoislands. By fitting the experimental data with the parameters calculated from the free electron model [217], one can obtain the dispersion of the surface state, which is shown in Fig. 7.4(d) and discussed further below. The band-edge of the measured surface state for the Fe-deposited gold surface is shifted up by about 100 meV relative to the clean surface, and the effective mass has increased. To understand these experimental observations, we have studied the electronic properties of the Fe/Au(111) surface. However for the ease of calculations, we have considered a single layer of Fe instead of nanoislands, which enables us to see how the Shockley state on the Au(111) surface is affected by the deposition.

7.3 Computational Details

We have used spin polarized density functional theory calculations as implemented in the PWscf code of the Quantum-ESPRESSO package [29]. We have used a plane wave basis set with an energy cut-off 20 Ry for the wave

functions and a charge density cut-off equal to 180 Ry. We have used ultrasoft pseudopotentials [18], and the local density approximation (LDA) of the Perdew-Zunger form [10]. for the exchange-correlation functional. We have used a $(15 \times 15 \times 1)$ Monkhorst-Pack [19] k-point mesh for Brillouin zone sampling; and the Methfessel-Paxton smearing technique [22] with the smearing width kept equal to 0.01 Ry. We have performed convergence tests to obtain an optimum energy cut-off and k-point grid.

We have used a supercell geometry to model the surface within periodic boundary conditions. The supercell is constructed in such a way that the surface normal, i.e., the [111] direction, is along the z-axis, and the x and y-axes are along the $[\bar{1}10]$ and $[\bar{1}\bar{1}2]$ directions respectively. Since we are interested in studying the effect of Fe deposition on the Shockley surface state of the clean Au(111), it is necessary to ensure that there is no splitting of the surface state due to an interaction between the top and bottom surfaces of the constructed slab. It has been reported previously that structural relaxations are described well by much thinner slabs than that required to avoid surface state splitting, e.g., Takeuchi, *et al.* [127], have used a seven-layer slab to find the surface structure and a 15-layer slab for its electronic properties, and in another study, Nicolay, *et al.* [196], have reported that a 23-layer slab is required to avoid splitting. Therefore we have performed detailed convergence tests with respect to the number of atomic layers (n_a), which are described in Section 7.4. Based on these tests, the supercell chosen for the clean surface consists of 39 atomic layers separated by about 18.7 Å vacuum; and for the Fe-deposited surface, we have deposited a pseudomorphic Fe layer on both sides of the slab. We have allowed relaxation of the topmost Fe layer

along with the three adjacent Au layers on both sides of the slab.

7.4 Results and Discussion

We have first calculated the nearest neighbor (NN) distance for bulk Au which is equal to 2.86 Å; this matches quite well with the experimental value (= 2.89 Å) [103] with an error of about 1%. The value is slightly underestimated as opposed to those calculated in the earlier work in this thesis, where we had used the generalized gradient approximation. It is well known that the LDA functional generally overbinds. Note that the error in the calculated lattice constant is smaller for the LDA than the GGA. For bulk Fe in the body-centered cubic structure, the calculated NN distance is equal to 2.38 Å, which compared with the experimental value (= 2.48 Å) [103] gives an error of about 4%. The error is slightly larger than those found with GGA functionals in the earlier chapters. However, here we will be studying a pseudomorphic Fe layer on the Au surface which is better described by the LDA, so we have used LDA exchange-correlation for this study. The calculated magnetic moment for bulk Fe is equal to 2.09 μ_B per atom, as compared to the experimental value of 2.22 μ_B per atom [109].

As described in Section 7.3, we have done extensive convergence tests with respect to the number of atomic layers, so as to avoid splitting of the surface states resulting from even slight interaction between the two surfaces. We have calculated the band structure for the clean gold surface for different numbers of atomic layers n_a. We found a splitting of 7 meV when n_a is equal to 21, which reduces to 1 meV when n_a is increased to 33, and vanishes only

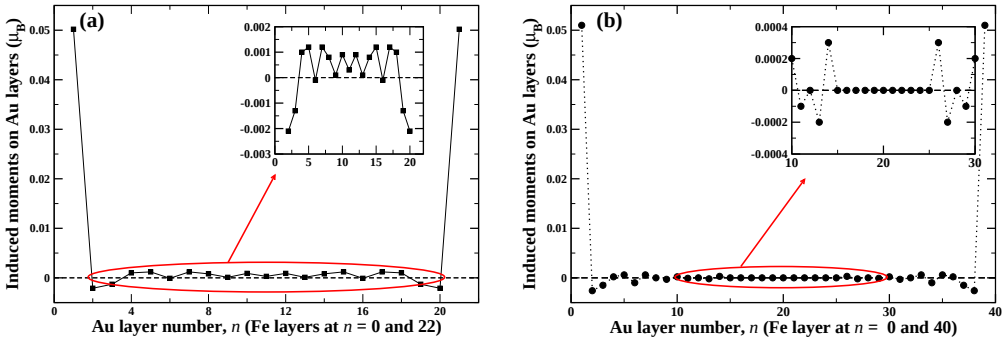

Figure 7.3: *Induced magnetic moments on Au atoms when Fe layers are deposited on both sides of (a) a 21-layer and (b) a 39-layer gold slab: an oscillatory pattern commonly observed for the RKKY-type of interaction is observed, which extends up to the middle layers of the slab for a 21-layer slab, but not for a 39-layer slab which can be clearly seen in the insets of each panel showing a central part of the slab.*

when $n_a = 39$; this is contrary to previous reports where it was claimed that convergence was achieved with thinner slabs [127, 196, 218].

For the deposited Fe layer, we find that the magnetic moment is equal to 3.0 μ_B per Fe atom, which is enhanced as compared to the bulk Fe moment, as has been reported earlier [218, 221]. This value is more or less insensitive to the number of Au layers in the slab. Due to the presence of Fe layers on both sides, there is an additional interaction present – the Ruderman-Kittel-Kasuya-Yosida (RKKY) interaction through the Au slab. This interaction will decrease as the thickness of the slab increases. The presence of the interaction can be seen by the induced moments on the Au layers extending even to the center of the slab; this was found to be the case for, e.g., $n_a = 21$, as shown in Fig. 7.3(a). However, when we increase the number of gold layers in the slab to 39 layers, then the induced moments on the Au atoms

at the center of the slab go to zero as can be seen in Fig. 7.3(b). Therefore we have used a (39+2)-layer slab for further calculations to ensure that the RKKY interaction between the two Fe layers is absent.

As we have discussed in the introduction, the top layer of the Au(111) surface is reconstructed and various atoms in the top layer have different stacking. The deposited Fe atoms can also occupy different stacking sites on the surface. These different stacking possibilities may conceivably lead to different electronic properties. Therefore, we have calculated the energetics of various possible stacking sites for the clean and the Fe-deposited surfaces. For the clean surface, we have considered two possibilities – the topmost layer occupying either fcc or hcp stacking sites. Note that here we have not considered atop or bridge sites because it is known that these two sites are much higher in energy [127]. We find that the fcc stacking site is lower in energy than the hcp site by about 14.4 meV per surface atom, which agrees with previous results [127]. For the Fe/Au(111) system, we have considered four possibilities, in which both Fe and the top Au layer occupy either fcc or hcp stacking sites; these possible stacking sequences are tabulated in Table 7.1 along with their relative energies. We find that the first case in which the Fe layer and the top Au layer occupy fcc sites (labelled as Fe-f/Au-f) is the most stable configuration, followed by the case in which the Fe layer is at the fcc site, and the top Au layer is at the hcp site; these two cases differ in energy by about 3 meV per surface atom. The remaining two cases are higher in energy by more than 25 meV per surface atom, therefore we have considered only the first two cases for further calculations.

Next we have calculated the electronic band structure for the clean Au(111)

Case number and name	(1) Fe-f/Au-f	(2) Fe-f/Au-h	(3) Fe-h/Au-f	(4) Fe-h/Au-h
Fe	A	C	B	B
Au1	C	A	C	A
Au2	B	B	B	B
Au3	A	A	A	A
Au4	C	C	C	C
Au5	B	B	B	B
Au6	A	A	A	A
δE	0.00	2.95	29.4	26.8

Table 7.1: *Various stacking possibilities for the Fe/Au(111) system and their relative energies: δE is the relative energy of each case with respect to the most stable configuration, given in meV per surface atom.*

surface, which is shown in Fig. 7.4(a), along two high symmetry directions $\bar{\Gamma}$-$\bar{K}$ and $\bar{\Gamma}$-$\bar{M}$ in the surface Brillouin zone (SBZ); here it is shown for the fcc-stacked top Au layer. The SBZ for this surface is shown in Fig. 7.5. On the same plot, we have also shown the projected band structure for bulk Au, so as to see the effect of the surface clearly. We observe a single band appearing in the projected band gap of the bulk just below the Fermi energy E_f, with the band-edge at $E - E_f \approx$ -0.47 eV, and having effective mass m^* equal to 0.20 m_e, where m_e is the mass of a free electron. This state is consistent with the experimentally observed Shockley state on the Au surface. The values of the band-edge and the effective mass agree well with previous results [196, 222, 223]. In Fig. 7.4(b), we have compared the dispersion of this surface state (labelled as C) with the experimental dispersion of the clean Au(111) surface state (shown with orange dashed line and taken from Ref. [222]), and we see good agreement between our results and the experimental results. On the same plot, we have also shown the band dispersion of the surface state for the configuration in which the topmost Au layer occupies

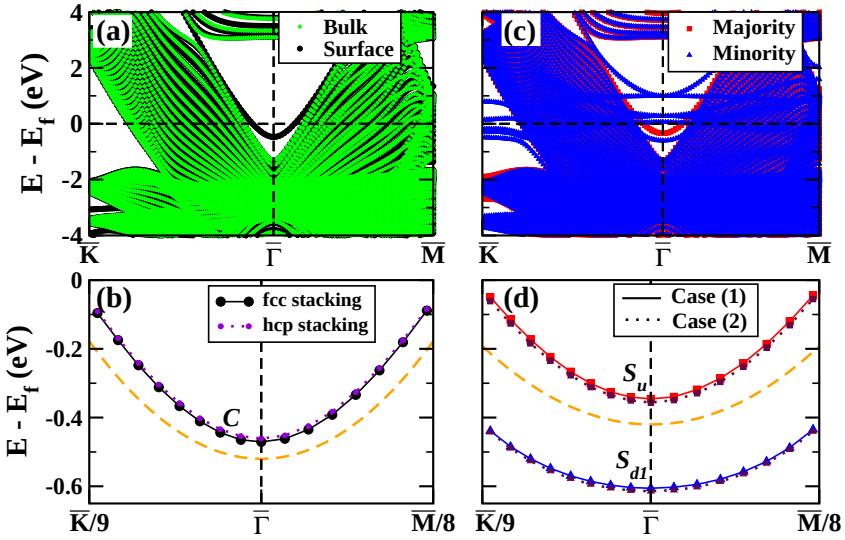

Figure 7.4: *The band structure for (a) the clean Au(111) surface and (c) the Fe/Au(111) surface plotted along two high symmetry directions* $\bar{\Gamma}$-$\bar{K}$ *and* $\bar{\Gamma}$-$\bar{M}$ *in the surface Brillouin zone. In panel (a), we have also plotted the projected band structure for bulk gold (green diamonds) for comparison. In panel (c), red squares (blue triangles) denote bands in the majority (minority) spin channel. In panels (b) and (d), we have shown the dispersion of the surface states appearing below the Fermi energy* E_f *for different stacking possibilities for the clean and Fe-deposited surface respectively along with the experimental dispersion curves (dashed orange line). In the lower panels, for clarity, we have only shown regions near* E_f *and areas of the SBZ for small* k*.*

instead the hcp stacking site (dotted line). We do not observe any significant effect of the stacking on the Shockley surface state (see Table 7.2).

We have then calculated the spin polarized band structure for the Fe/Au(111) surface, shown in Fig. 7.4(c) for case (1), in which both the Fe layer and the topmost Au layer occupy fcc stacking sites. We observe the appearance of a single state in the majority spin channel, and a large number of states in the minority spin channel in the bulk band gap. The state in the majority

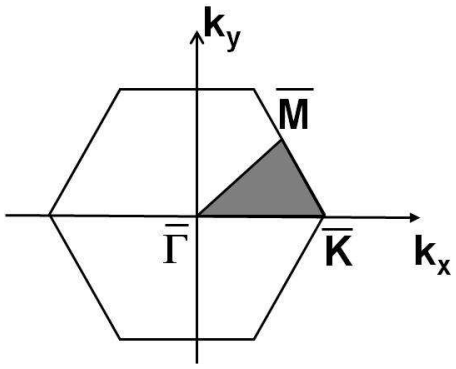

Figure 7.5: *2D Brillouin zone for the fcc(111) surface: two high symmetry directions are shown from the zone center* $\bar{\Gamma} = (0,0)$ *to* $\bar{K} = \frac{2\pi}{a}(\frac{2}{3},0)$ *and to* $\bar{M} = \frac{2\pi}{a}(\frac{1}{2},\frac{1}{2\sqrt{3}})$*. The shaded area shows the irreducible SBZ.*

Case		Au-f	(1) Fe-f/Au-f			Au-h	(2) Fe-f/Au-h		
State label		C	S_u	S_{d1}	S_{d2}	C	S_u	S_{d1}	S_{d2}
Band-edge (eV)		-0.47	-0.35	-0.61	0.06	-0.46	-0.36	-0.61	0.06
m^*/m_e	$\bar{\Gamma}$-$\bar{K}$	0.20	0.26	0.55	-2.73	0.20	0.26	0.54	-3.06
	$\bar{\Gamma}$-$\bar{M}$	0.21	0.27	0.55	-2.62	0.21	0.27	0.53	-2.62

Table 7.2: *The position of the band-edge, and the effective mass* m^**, of the dispersive surface state electrons, along high symmetry directions, are tabulated for two different stacking possibilities. Here* m_e *is the mass of a free electron, and the band-edge position is the energy of the band at* $\bar{\Gamma}$ *with respect to the Fermi energy. The slope of the band along the two symmetry directions can be slightly different, and therefore we have calculated the effective mass for both directions separately.*

channel, which we call S_u, is shifted upward in energy as compared to the state C; it has the band-edge at $E - E_f \approx$ -0.35 eV, and its effective mass is equal to 0.26 m_e. Only one of the surface states, called S_{d1}, in the minority channel, appears below the Fermi energy. This state is shifted downward in energy relative to the state C, and has the band-edge at $E - E_f \approx$ -0.61 eV, and effective mass equal to 0.55 m_e. The effective mass has increased on Fe deposition, as was observed in the experiments, as explained in Section 7.2, however the increase is more for the minority surface state than that for the

majority surface state. In Fig. 7.4(d), we have compared the band dispersions of these two bands, for two different configurations – case (1) and case (2); we have plotted only in the region of interest, that is, in the vicinity of E_f. As was the case for the clean surface, we see only a slight effect of stacking on the band dispersion; we have tabulated the band-edge and the effective mass values in Table 7.2 for both the cases. In the same plot, we have also shown the experimental band dispersion (dashed orange line), we observe that the state S_u shows a shift similar to that seen in the experimental results. We will discuss this point further below. The remaining states in the minority channel, which appear in the bulk band gap, lie above E_f. At $E - E_f \approx 0.06$ eV, there is a single state labelled as S_{d2} with a very flat dispersion; its effective mass is given in Table 7.2. At the energies $E - E_f \approx 0.27$ eV and 0.99 eV, there are states which are doubly degenerate near Γ, which we have labelled as S_{d3} and S_{d4} respectively. For most of these states appearing above the Fermi level, the dispersion is very flat indicating a high effective mass.

Now we analyze the electronic properties further using the projected density of states (PDOS), local density of states (LDOS) and charge density profiles, to understand the origin and the nature of the new states which appear in the bulk band gap on Fe deposition. For this detailed analysis, we have considered only the most stable stacking configurations, that is, for the clean surface the topmost Au layer is fcc stacked, and case (1) for the Fe-deposited system, because as seen from the band structure plots, the effect of different stacking is not significant on the electronic properties.

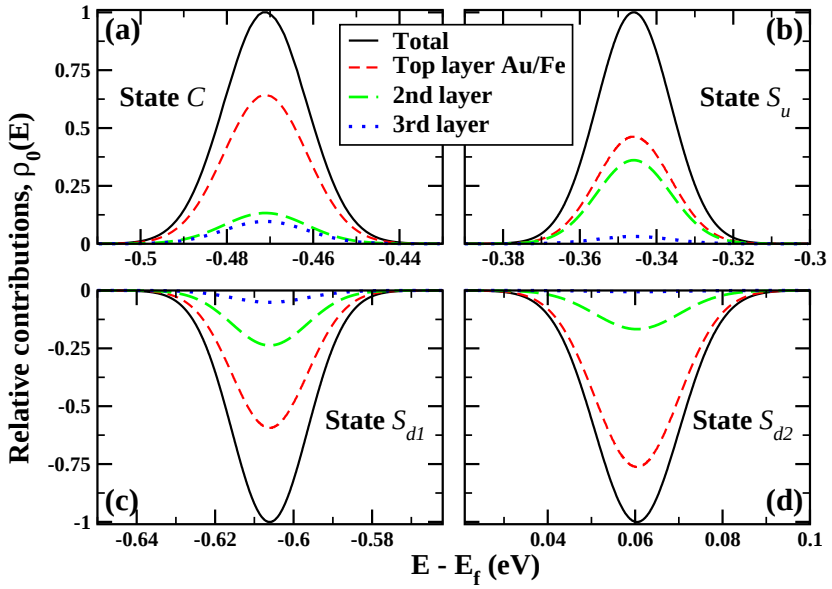

Figure 7.6: *Projected density of states for the surface states, obtained by performing calculations restricted to the $\bar{\Gamma}$-point: We have plotted relative contributions from different layers to the total DOS for the surface states (a) C, (b) S_u, (c) S_{d1}, and (d) S_{d2}; we have decomposed into contributions only from the top three surface layers. In (a), the topmost layer is Au, whereas for (b), (c), and (d), it is Fe.*

To calculate the density of states, we have restricted ourselves to contributions coming from $\mathbf{k} = 0$, which results in δ-function peaks in the bulk band gap, at the energies corresponding to the surface states. By projecting onto atomic orbitals, these can be decomposed to calculate contributions from different layers and different atomic orbitals. These PDOS plots calculated for the states C, S_u, S_{d1} and S_{d2} are shown in Fig. 7.6, where the δ-functions have been modeled by Gaussians, $\rho_0(E)$, of width 0.001 Ry. Note that for the state C, the main contribution is from the topmost Au layer, as is expected for the Shockley surface state. Further, we have observed that the s and p

orbitals of Au mainly contribute to this state. For the Fe-deposited surface, the state S_u has almost equal contributions from the Fe layer and the topmost Au layer, whereas for the states S_{d1} and S_{d2}, the main contribution is from the Fe layer, and only a small contribution from the Au layers. Further analysis of atomic orbital contributions shows that the state S_u has main contributions from the s and p orbitals of Au and the s orbital of Fe, and the state S_{d1} mainly originates from the d_{z^2}-orbitals of Fe; whereas the state S_{d2} originates mainly from the s and d_{z^2}-orbitals of Fe. The surface states S_{d3} and S_{d4} (not shown here) arise purely from the remaining d-orbitals of the Fe atoms – the $d_{x^2-y^2}$ and d_{xy} orbitals of Fe contribute to the state S_{d3} and the d_{zx} and d_{yz} orbitals to the state S_{d4}.

Next, we have calculated the charge density profiles for the surface states, again by restricting ourselves to the $\bar{\Gamma}$-point. These are shown in Fig. 7.7 for the states C, S_u, S_{d1} and S_{d2}; for plotting, we have selected a yz-plane perpendicular to the slab. By calculating the planar average of these charge densities in different xy planes as a function of z, we can calculate the decay lengths for the surface states in the vacuum. The decay length of any state is a measure of the spread of that state in the vacuum, and only states which have significant charge density at distances of $\gtrsim$ 5 Å (a typical distance between the STM tip and the surface) can be detected by STM. For the state C, shown in Fig. 7.7(a), we observe that the charge density is mainly spread near the uppermost surface layer and decays as one moves away from the surface, either towards the vacuum or towards the bulk. When we look at the planar average of the charge density corresponding to this state (see Fig. 7.8(a)), we observe a large peak in the charge density just above the

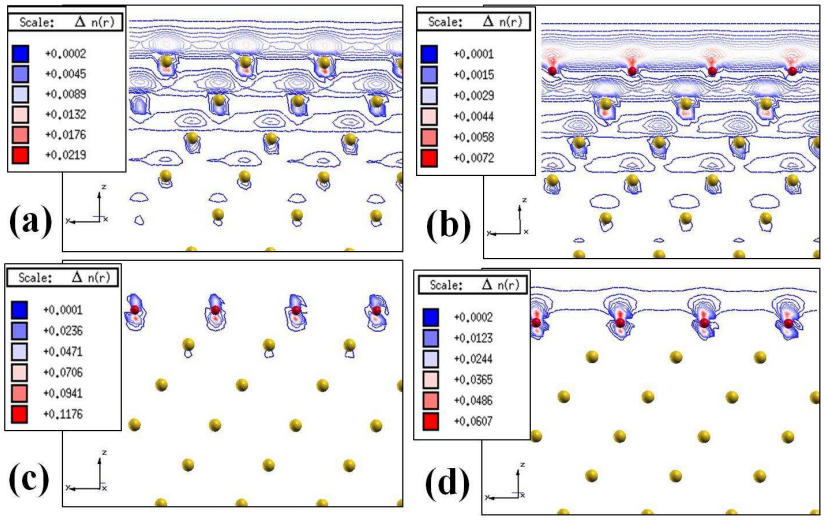

Figure 7.7: *Charge density profiles corresponding to the surface states: we have shown here the charge density profiles for (a) state C on the clean Au(111) surface, and states (b) S_u, (c) S_{d1}, and (d) S_{d2} on the Fe/Au(111) surface. The spheres denote atomic positions – red (yellow) for the Fe (Au) atoms. The contours show the charge density values (in electrons/Å^3) with the scale shown for each panel separately.*

topmost Au layer, which decays exponentially in the vacuum; the decay length is equal to 0.45 Å. Within the bulk, the charge density decays slowly with small peaks appearing between atomic planes, and decreases to almost zero beyond the fourth layer.

Now we consider the charge density profiles for the surface states on the Fe-deposited surface. In Fig. 7.7(b), we have shown the charge density for the state S_u, which we find to be very similar to that for the Shockley state of the clean surface. As can be seen from the planar average of the charge density for this state, shown in Fig. 7.8(b), (green solid line), it has a peak just above the Fe layer with an exponential decay into the vacuum, and it decays slowly into the bulk, having smaller peaks in between atomic planes. The decay length for this state in the vacuum is equal to 0.51 Å. This is in

accordance with the PDOS analysis showing that this state arises from both the Shockley state of Au as well as the Fe s orbital. The states S_{d1} and S_{d2} are more localized on the Fe layer, as can be seen from Fig. 7.7(c) and (d), however for S_{d2}, there is a small spread in the vacuum. When their respective planar averages of charge densities are examined (see the red dashed and blue long-dashed lines in Fig. 7.8(b)), we clearly see that the state S_{d1} is localized only on the Fe layer, whereas the state S_{d2} extends into the vacuum, similar to the state S_u, and has a comparable decay length of 0.54 Å. However, unlike S_u, the S_{d2} state decays very quickly into the bulk. This also is in accordance with our PDOS analysis. From this analysis, it may be expected that the state S_{d2} will lead to a peak just above the Fermi level in the experimental STS spectrum. However, as shown in Fig. 7.2(a), the confined S_u state also leads to a peak close to the Fermi level. Thus it would be difficult to separate out these two contributions in the experimental spectrum.

Finally, we have calculated the local density of states (LDOS) as a function of energy, by integrating over the complete surface Brillouin zone at various distances d from the surface plane. The plots for the LDOS, calculated for three different d values, are shown in Fig. 7.9. Note that there is a sharp peak at the Fermi level in the minority spin channel (blue dashed line). A similar feature was also observed by Donati, *et al.*, [218] in the LDOS, however with a slight shift in the peak position, which can be attributed to the small difference in the lattice constant of Au in our study and theirs. As d increases, the LDOS values decay rapidly (note that the y-axis scale on each panel in Fig. 7.9 is different), however the reduction is slower for the peak at E_f which can be seen prominently even at 4 Å above the surface.

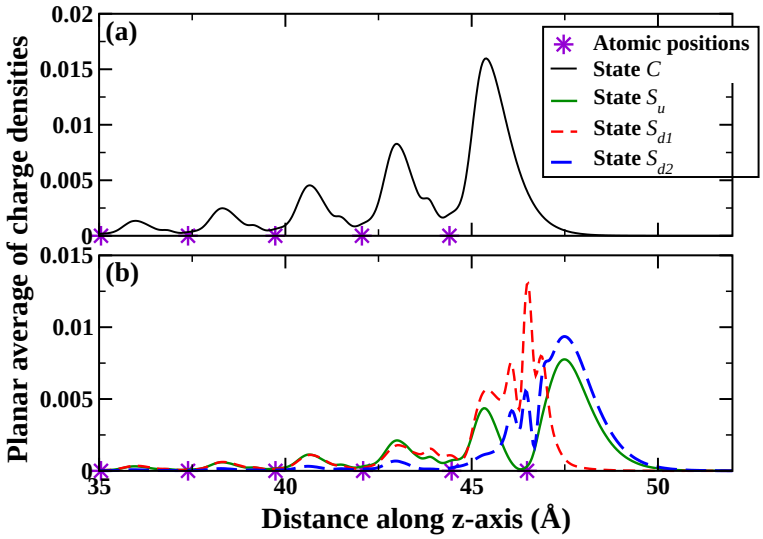

Figure 7.8: *Planar average of the charge densities corresponding to the charge density profiles shown in Fig. 7.7: They are plotted as a function of distance along the z-direction for (a) the clean surface and (b) the Fe/Au(111) surface. The states C, S_u and S_{d2} have a large spread in the vacuum, while the state S_{d1} is localized on the Fe layer.*

The state S_{d2} is responsible for this peak, which has a large decay length in the vacuum, and its flat dispersion gives rise to the sharpness of the peak. This will not be the case for the electrons in the S_u state which has a free electron-like dispersion.

In the STS measurement shown in Fig. 7.2(a), there are multiple peaks observed, in contrast to a single peak in the calculated LDOS. Recall that the experiments were done for nanoislands, whereas our calculations are done for a complete monolayer, therefore we cannot directly compare the LDOS plotted in Fig. 7.9 with the spectrum in Fig. 7.2(a). The presence of nanoislands

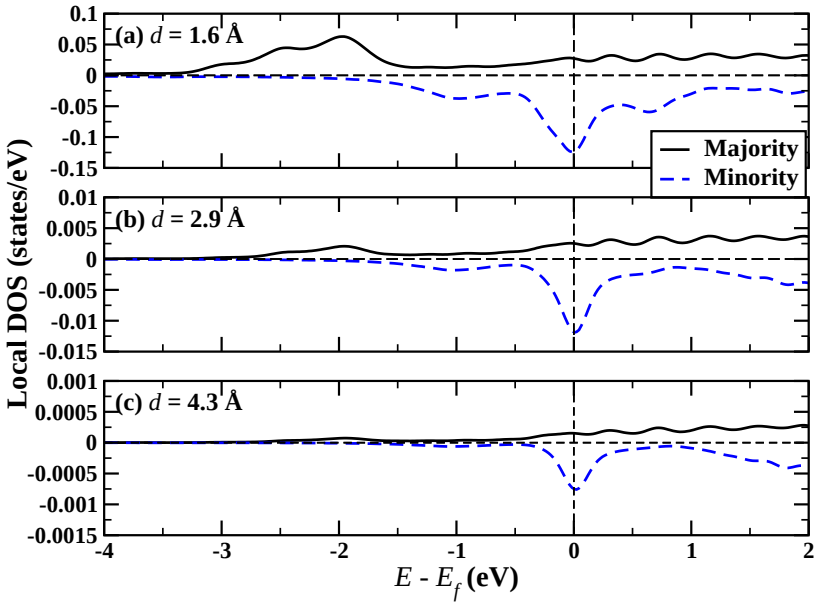

Figure 7.9: *Local density of states as a function of energy, at distances d above the surface, equal to (a) 1.6 Å, (b) 2.9 Å, and (c) 4.3 Å These results were obtained for a gold slab containing 21 layers with the Fe layer deposited on each side of the slab. Each panel has a different y-axis scale because by increasing d by ∼ 1 Å, the LDOS values decrease by an order of magnitude. The solid black and dashed blue curves are for the majority and minority spins respectively.*

can lead to the scattering of the surface state electrons. The scattering is possible only in the case of the S_u state, which has free-electron like dispersion, and not for the electrons in the S_{d2} state having flat dispersion. The peaks observed in the measured STS spectra arise mainly due to the confinement of the S_u state electrons, in contrast to the calculated LDOS. In accordance with this observation, the properties of the surface state observed in the experiments match well with the calculated S_u state in the majority channel,

because the measured dispersion was derived from the confined Shockley-state on the Fe/Au(111) system.

7.5 Summary and Conclusions

We have studied here the effect of deposition of a single pseudomorphic Fe layer on the Shockley surface state of the Au(111) surface, and compared our results with experiments. The magnetic moments on the deposited Fe atoms are enhanced as compared to those on bulk Fe atoms. We have calculated the band structure for the system, and observe that a large number of states appear in the projected bulk band gap; out of these states, only one appears in the majority spin channel and others are present in the minority spin channel. For most of these states, the effective mass of electrons is higher than that for the clean gold surface state electrons. The detailed analysis, using the projected density of states and the local density of states, shows that only the states S_u and S_{d2} have a large extent in the vacuum, however only the state S_u, in the majority spin channel, behaves in a very similar manner to the Au Shockley surface state. Thus we conclude that the Shockley surface state gets spin polarized on Fe deposition. The remaining states appearing in the bulk band gap originate from Fe d states and therefore are not "true" surface states. Because of their large extent in the vacuum, only the states S_u and S_{d2} are likely to be detected in experimental STS measurements. However, only the state S_u can be scattered at the nanoisland edges and hence lead to the standing wave patterns observed in the STS spectrum. We have also shown that the effect of different stacking (of the Fe overlayer and

the topmost Au layer) is very small on the band-edge values and the effective masses of the surface state electrons.

Some of the work presented here has been published in Ref. [224].

Chapter 8

Summary and Conclusions

In this chapter, I will summarize the main findings and highlights of this thesis. We had set out to study various aspects of the surface, such as the structural properties of magnetic surface alloys, the effect of various interactions on the miscibility of such alloys, the possibility of surface reconstruction in heteroepitaxial systems, and the electronic properties of an interface. We have primarily used density functional theory calculations for these studies, along with the cluster expansion method and the Frenkel-Kontorova model wherever necessary.

One of the main highlights of our work was to show that it is possible to design a surface alloy using first principles methods. This reduces the time and cost otherwise required to examine various possibilities with experimental techniques. We have shown that the mixing of a pair of bulk-immiscible metals is possible when restricted on the Ru(0001) surface . By studying a large number of such pairs of metals, we have shown that both elastic and chemical interactions are important to determine the miscibility. We

have shown that one should not expect to find any size-dependent rules for mixing, unlike in the bulk alloys. Based on our analysis, we were able to suggest the best possible candidates for the experimental observation of alloy formation from bulk-immiscible components. One of these candidates – Fe-Au/Ru(0001) – was experimentally investigated by our collaborators, and was indeed observed to form an atomically mixed surface alloy, and to also have long-range order. By performing further calculations on this system, we were able to show that the configurations which have the highest magnetic moments are always preferred, rather than the configurations with the lowest surface stress. Also, the magnitude of the enthalpy of mixing is significantly lowered when spin polarization is suppressed. These two findings imply that the main driving force for alloy formation in this system is magnetism, and not surface stress reduction as was believed previously. Recall that Fe and Au are completely bulk-immiscible, however we have shown that they do form a long-range ordered alloy on the Ru(0001) surface.

We have then proceeded to check whether the formation of thin film Fe-Au alloys is dependent on the nature of the substrate by replacing the Ru(0001) surface by the Mo(110) surface. For this study, we have used a combined study with density functional theory and cluster expansion methods, which allowed us to study very large unit cells. We have shown that the mixing properties are largely affected by changing the substrate. For Fe-Au/Mo(110), we have observed a smooth convex hull which would lead to many competing structures and therefore we would not expect long-range order as was observed on Ru(0001). This agrees with previous experiments done on Fe-Au nanostructures on Mo(110), in which atomic-level

mixing was observed, but without any long-range order. We have also shown that magnetism is not the dominant driving force for mixing, unlike for Fe-Au/Ru(0001). We speculate that this difference might arise from anisotropy of the Mo(110) surface, but this issue needs further exploration.

Mixing of overlayer metals need not be the only mechanism which reduces the surface stress, the single-component and/or alloy overlayer may reconstruct to reduce the stress. Thus we have studied the possibility of reconstruction for the single-component overlayers on the Ru(0001) surface. We have not considered alloy overlayers for this study because we have shown that mixing reduces the surface stress, and therefore, we believe that reconstruction is more unlikely for these. We have used the Frenkel-Kontorova model for this study, because the system sizes are large, making DFT studies computationally expensive. One of two approaches have previously been used to solve the FK model for similar systems – first, mapping it to a one-dimensional chain of atoms, and second, a complete solution of the two-dimensional Frenkel-Kontorova Hamiltonian using quenched molecular dynamics simulations. In the first approach, one can find a dimensionless parameter R which can estimate the possibility of reconstruction, but this was previously only applicable for homoepitaxial systems. We have extended the definition of R to heteroepitaxial systems, and shown that this extension works well, by comparing our results with those obtained by numerically solving the complete 2D Frenkel-Kontorova Hamiltonian, and also with experimental results. This extension simplifies the estimation of the possibility of reconstruction. We were also able to show that by tuning the chemical potential (required to add or remove an atom leading to reconstruction), we

can control the periodicity of reconstruction. This is useful from the point of view of possible applications, where the reconstructed surface is used as a template of self-organized nanostructures.

We have also studied the electronic properties of Fe/Au(111). We have shown that the deposition of a single layer of Fe layer results in spin polarization of the Shockley surface state on the clean Au(111) surface. We have calculated the band-edge and the effective mass for the surface state electrons. By further local density of states and projected density of states analysis, we were able to examine the nature and origin of various new states observed in the projected bulk band gap of Fe/Au(111). Scanning tunneling spectroscopy measurements performed on Fe nanoislands on the Au(111) surface have observed a number of peaks in the spectrum, and spatial inhomogeneity in the local density of states. By comparing these results with our theoretical work, we were able to establish that the standing wave patterns observed for this system, originated from the Shockley state.

In our work, we have seen a great synergy between theory and experiments. Both the experimental and theoretical studies were used to complement results from the other – thus experiments could confirm predictions from the theory and theoretical investigations could shed light on experimental findings by examining the underlying mechanisms. In the case of surface alloys, theory preceded the experimental investigation, and suggested the best candidates for surface alloys. The existence of long-range ordered surface alloys for bulk-immiscible components could be established by experiments. Such parallel work would increase the efficiency of designing materials with required properties. For spin polarized surface states on Fe/Au(111),

the experiments were performed before the calculations, and the observation of some interesting standing wave patterns for Fe nanoislands motivated our calculations. In turn, our theoretical investigation was beneficial to analyze experimental observations.

Outlook

There are many open questions which can be addressed in the future: e.g., temperature dependent properties, such as the temperature-composition phase diagram for two of the surface alloy systems studied in this thesis – Fe-Au/Ru(0001) and Fe-Au/Mo(110) – using the cluster expansion method; and a better understanding of dissimilar properties of Fe-Au overlayers on the two substrates by (i) separating out the elastic and chemical interactions for Fe-Au/Mo(110), and by comparing the relative importance of these interactions with the situation for Fe-Au/Ru(0001), and (ii) computing the magnetic interactions for each system which might involve non-collinear magnetic calculations.

In this thesis, we have only considered collinear magnetism, and further only ferromagnetic alignment of spins was studied. It would be interesting to study the possibility of antiferromagnetic alignment or non-collinear magnetic structures. Especially for surface alloys on the Ru(0001) surface, the triangular lattice can lead to frustrated spin structures, in case antiferromagnetic interactions are favored; this might give rise to novel spin structures such as spin spirals. Also for applications in magnetic storage devices, a high magnetic anisotropy energy is necessary, therefore it would be interesting to

examine magnetic anisotropy properties. This would necessitate the inclusion of spin-orbit interactions in our calculations. Further, alloying may lead to increased reactivity, and these types of surface alloys would be potential candidates as catalysts. To examine whether these systems are good catalysts or not, it would be interesting to study chemical reactions on these surfaces as well as look at other indicators of catalytic activity such as the positions of d-band centers [122, 225].

Appendix A

Derivation of surface stress

In this appendix, we have described our procedure to separate various contributions to the stress in the slab so as to obtain the surface stress as a function of intralayer bond length. This expression is derived for the (0001) surface of a hcp crystal. This surface has a triangular lattice with three-fold symmetry. We have considered a slab with n_a atomic layers with l_{xy} and d as intralayer and interlayer NN bond lengths respectively; the schematic picture is shown in Fig. A.1. For this derivation, we have assumed a symmetric slab with a single layer of "magnetic" element M or "non-magnetic" element N on each side of substrate. To get the surface stress, we need to subtract out the contribution coming from the substrate layers, to the total stress. To be able to do this subtraction, we need to consider all the bonds which contribute to the total stress.

We have considered the area element $L_y L_z$ in the yz-plane passing through the slab and then count all the NN bonds which cut the area and forces coming due to these bonds. There will be n_a intralayer NN bonds and (n_a - 1) interlayer NN bonds. Among these terms, the surface contribution comprises two intralayer terms corresponding to the two overlayers and two interlayer terms corresponding to the bonds between the overlayer and the adjacent substrate layer. The "volume stress" has dimensions of force per unit area, whereas the surface stress has dimensions of force per unit length. The xx-component of the "volume stress" $\sigma_{xx}^{V,slab}$ can then be written in terms of the

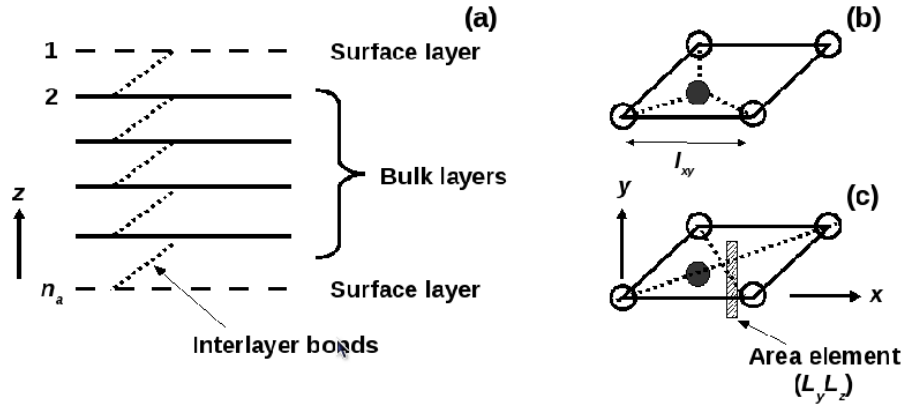

Figure A.1: *(a) Side view of the slab and (b) and (c) top views of the surface unit cell, considered for deriving surface stress as a function of intralayer bond length, are shown. The unfilled and filled circles in the right hand panel show stacking for two adjacent layers. In panel (b), dotted lines show interlayer NN bonds considered to derive Eq.* (A.6)*, and in panel (c) the shaded area shows a projection of an area element* L_yL_z*.*

forces exerted by these various bonds:

$$\begin{aligned}\sigma_{xx}^{V,slab} &= \frac{F_{xx}^{tot,slab}}{L_yL_z} \\ &= \frac{2F_{xx}^{intra,surf} + (n_a-2)F_{xx}^{intra,b} + (n_a-3)F_{xx}^{inter,b} + 2F_{xx}^{inter,surf}}{L_yL_z},\end{aligned} \tag{A.1}$$

where $F_{xx}^{tot,slab}$ is the xx-component of the total force on the slab which is the sum total of all the forces due to intralayer bonds in the two surface layers $F_{xx}^{intra,surf}$; (n_a-2) intralayer terms $F_{xx}^{intra,b}$; (n_a-3) interlayer terms $F_{xx}^{inter,b}$ coming from the substrate layers, and two interlayer bonds between the surface layers and adjacent substrate layers $F_{xx}^{inter,surf}$. The last term in the above expression can be approximately neglected if one allows the surface layers to relax toward or away from the substrate. Then we can write the

xx-component of the "volume stress" as,

$$(\sigma_{xx}^{V,slab})L_z = \frac{2F_{xx}^{intra,surf}}{L_y} + \frac{F_{xx}^{intra,b}}{L_y} + \frac{(n_a-3)F_{xx}^{tot,b}}{L_y}$$
$$= \sigma_{xx}^{surf} + \frac{F_{xx}^{intra,b}}{L_y} + \frac{(n_a-3)F_{xx}^{tot,b}}{L_y}, \tag{A.2}$$

where σ_{xx}^{surf} is the surface stress – the quantity we would like to find, and $F_{xx}^{tot,b} = F_{xx}^{intra,b} + F_{xx}^{inter,b}$. However, among the various terms in the above equation only $\sigma_{xx}^{V,slab}$ is directly obtained from *ab initio* calculations, therefore we would like to express the remaining terms using other quantities directly accessible via DFT calculations. For this purpose, we have considered a bulk unit cell having a unit cell commensurate to that of the slab, and then by stretching or compressing the bulk unit cell in-plane to the same l_{xy}, we can calculate the "volume stress" for the bulk at different in-plane bond lengths.

We know that the xx-component of the "volume stress" for the bulk is given by,

$$\sigma_{xx}^{V,bulk} = \frac{F_{xx}^{tot,b}}{L_y(\frac{c}{2})} \quad \Longrightarrow \quad \frac{F_{xx}^{tot,b}}{L_y} = \frac{c}{2}\sigma_{xx}^{V,bulk}, \tag{A.3}$$

where $c/2$ is the interlayer distance between two adjacent layers of the bulk along the [0001] direction.

Substituting (A.3) in equation (A.2), we get

$$(\sigma_{xx}^{V,slab})L_z = \sigma_{xx}^{surf} + \frac{F_{xx}^{intra,b}}{L_y} + (n_a-3)\sigma_{xx}^{V,bulk}\frac{c}{2}. \tag{A.4}$$

Now, to find the contribution due to one extra intralayer term, we have considered the zz-component of the "volume stress" for the bulk which has contributions only from interlayer bonds, and not from intralayer bonds:

$$\sigma_{zz}^{V,bulk} = \frac{F_{zz}^{tot,b}}{L_x L_y}, \tag{A.5}$$

where $F_{zz}^{tot,b}$ is the total force due to all NN bonds cutting an area element $L_x L_y$. To compute this, we have considered this area element having area equal to the surface unit cell, therefore, $L_x = l_{xy}$ and $L_y = \sqrt{3}l_{xy}/2$.

There are three NN interlayer bonds which cut this area (as can be seen in Fig. A.1b). The force exerted by each of these bonds is equal, therefore we can write,

$$F_{zz}^{tot,b} = 3 \times F^{inter,b}\Big(\frac{c/2}{d}\Big). \tag{A.6}$$

Substituting this in Eq. (A.5), we get

$$\begin{aligned} \sigma_{zz}^{V,bulk} &= 3 \times F^{inter,b}\Big(\frac{c/2}{d}\Big)\frac{1}{\frac{\sqrt{3}}{2}l_{xy}^2} \\ \text{i.e.,} \quad F^{inter,b} &= \sigma_{zz}^{V,bulk}\frac{l_{xy}^2 d}{\sqrt{3}c}. \end{aligned} \tag{A.7}$$

We are interested in the xx-component of the interlayer force $F^{inter,b}$, which we can find by

$$\begin{aligned} F_{xx}^{inter,b} &= F^{inter,b}\Big(\frac{l_{xy}/2}{d}\Big) \\ &= \Big[\sigma_{zz}^{V,bulk}\frac{l_{xy}^2 d}{\sqrt{3}c}\Big]\Big(\frac{l_{xy}/2}{d}\Big). \end{aligned} \tag{A.8}$$

Now substituting Eq. (A.8) in Eq. (A.3), we get

$$\begin{aligned} \sigma_{xx}^{V,bulk}(\frac{c}{2}) &= \frac{F_{xx}^{intra,b}}{L_y} + \frac{F_{xx}^{inter,b}}{L_y} \\ &= \frac{F_{xx}^{intra,b}}{L_y} + \frac{1}{\sqrt{3}l_{xy}/2}\Big[\sigma_{zz}^{V,bulk}\frac{l_{xy}^2 d}{\sqrt{3}c}\Big]\Big(\frac{l_{xy}/2}{d}\Big) \\ \frac{F_{xx}^{intra,b}}{L_y} &= \sigma_{xx}^{V,bulk}(\frac{c}{2}) - \frac{1}{3}\sigma_{zz}^{V,bulk}\Big(\frac{l_{xy}^2}{c}\Big). \end{aligned} \tag{A.9}$$

Substituting this in Eq. (A.4) and rearranging terms, we can write

$$\begin{aligned} \sigma_{xx}^{surf} &= (\sigma_{xx}^{V,slab})L_z - \Big[\sigma_{xx}^{V,bulk}\big(\frac{c}{2}\big) - \frac{1}{3}\sigma_{zz}^{V,bulk}\Big(\frac{l_{xy}^2}{c}\Big)\Big] - (n_a - 3)\sigma_{xx}^{V,bulk}\frac{c}{2} \\ &= (\sigma_{xx}^{V,slab})L_z - (n_a - 2)\sigma_{xx}^{V,bulk}\frac{c}{2} + \sigma_{zz}^{V,bulk}\frac{l_{xy}^2}{3c} \\ \implies \sigma_{xx}^{surf} &= (\sigma_{xx}^{V,slab})L_z - (n_a - 2)\sigma_{xx}^{V,bulk}\frac{c}{2} + \sigma_{zz}^{V,bulk}\frac{l_{xy}^2}{3c}. \end{aligned} \tag{A.10}$$

This expression gives the surface stress in the overlayer as a function of l_{xy}, i.e., the intralayer bond length. Recall that this expression is for the total surface stress coming from two surfaces of the slab, therefore for a symmetric slab one has to divide by a factor of two to get the required value and for an asymmetric slab, one has to subtract the stress coming from the unrelaxed substrate surface.

Appendix B

Formula for generating different unit cells

In this appendix, we have described the formulae used for generating different unit cells. For a two-dimensional lattice, one can obtain a general formula to determine all the distinct unit cells using group theory [148]. Let $\bar{a}_1$ and $\bar{a}_2$ be the basis vectors for the lattice. Then for the unit cell with n_a atoms, the basis vectors for possible unit cells are defined separately for two cases. Consider the first case in which n_a is a prime number, then let $n_a = p$. The total number of possible unit cells is equal to $(p + 1)$ and the unit cells are defined by basis cell vectors –

$$\begin{aligned} &(p\bar{a}_1, \bar{a}_2) \\ &(\bar{a}_1 + 0 \times \bar{a}_2, p\bar{a}_2) \\ &(\bar{a}_1 + 1 \times \bar{a}_2, p\bar{a}_2) \\ &\qquad \vdots \\ &(\bar{a}_1 + (p-1) \times \bar{a}_2, p\bar{a}_2) \end{aligned} \tag{B.1}$$

In the second case, n_a is not a prime number, then the basis vectors for all possible unit cells can be written as –

$$(b\bar{a}_1 + c\bar{a}_2, d\bar{a}_2), \tag{B.2}$$

where $b \times d = n$, $b \geq 1$ and $0 \leq c < d$.

We have used these formulae to obtain all the smallest unit cells ($n_a \leq 6$) for the hexagonal and the centered-rectangular unit cells which are used by us for the DFT calculations of Fe-Au/Ru(0001) and Fe-Au/Mo(110). Further, for a given unit cell, one has to determine various distinct ways to place Fe or Au atoms at each lattice point in the cell to determine all the possible distinct configurations.

Appendix C

List of Configurations for $Fe_xAu_{(1-x)}$/Ru(0001)

In this appendix, we have listed all the configurations considered in our study of $Fe_xAu_{(1-x)}$/Ru(0001). For a triangular lattice, the basis vectors (primitive lattice vectors for the (1×1) cell) are given by $\bar{a}_1 = (a, 0)$ and $\bar{a}_2 = (\frac{-a}{2}, \frac{\sqrt{3}a}{2})$, where a is the NN spacing of the substrate. Using the formulae given in Appendix B, we have found all the possible distinct unit cells for the number of overlayer atoms in the unit cell n_a = 2, 3, 4, 5, and 6; out of these, except for six-atom unit cells, we have considered all possible configurations for our *ab initio* calculations. For the six-atom unit cells, we have only considered some possibilities. After finding all the distinct unit cells, we have also checked for all the possible atomic arrangements in each of these unit cells.

We have shown below the schematic top views for the surface unit cells of Fe-rich configurations ($x \geq 0.50$). In all the figures, red and yellow spheres indicate Fe and Au atoms respectively; and small black dots indicate the positions of Ru atoms in the layer adjacent to Fe-Au overlayer. The corresponding configurations for Au-rich phases can be obtained by interchanging red and yellow spheres.

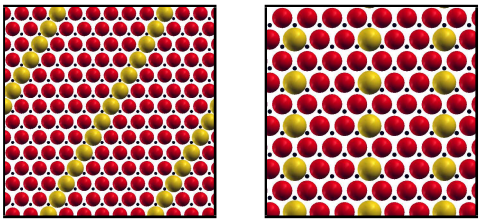

(a) (6×1) unit cell (b) $(2\sqrt{3} \times \sqrt{3})$ unit cell

Figure C.1: *Configurations for $x = 0.833$ (or 0.167) corresponding to Fe_5Au (or $FeAu_5$).*

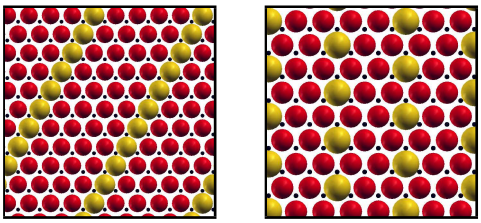

(a) (5×1) unit cell (b) $(\sqrt{7}\times\sqrt{3})$ unit cell

Figure C.2: *Configurations for $x = 0.80$ (or 0.20) corresponding to Fe_4Au (or $FeAu_4$).*

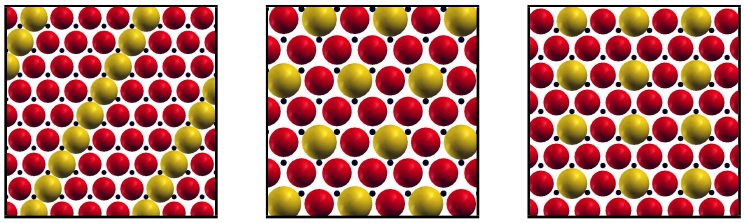

(a) (4×1) unit cell (b) (2×2) unit cell (c) $(2\times\sqrt{3})$ unit cell

Figure C.3: *Configurations for $x = 0.75$ (or 0.25) corresponding to Fe_3Au (or $FeAu_3$).*

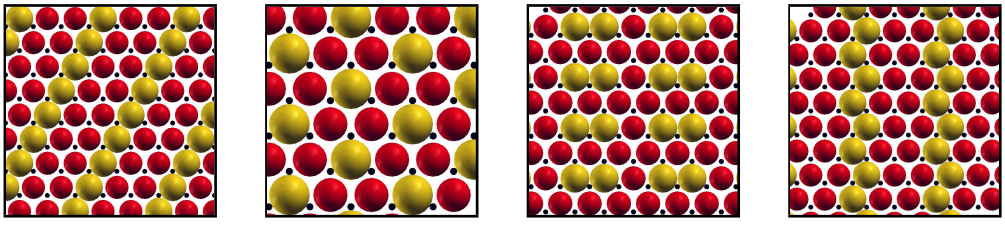

(a) (3×1) unit cell (b) $(\sqrt{3}\times\sqrt{3})$ unit cell (c) $(2\sqrt{3}\times\sqrt{3})$ unit cell - configuration 1 (d) $(2\sqrt{3}\times\sqrt{3})$ unit cell - configuration 2

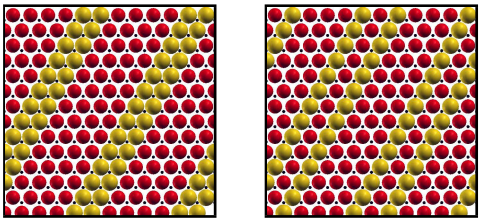

(e) (6×1) unit cell - configuration 1 (f) (6×1) unit cell - configuration 2

Figure C.4: *Configurations for $x = 0.667$ (or 0.333) corresponding to either Fe_2Au (or $FeAu_2$) or Fe_4Au_2 (or Fe_2Au_4).*

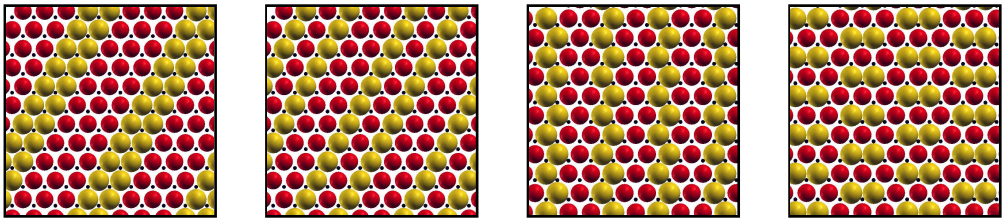

(a) (5×1) unit cell -configuration 1

(b) (5×1) unit cell -configuration 2

(c) $(\sqrt{7}\times\sqrt{3})$ unit cell - configuration 1

(d) $(\sqrt{7}\times\sqrt{3})$ unit cell - configuration 2

Figure C.5: *Configurations for $x = 0.60$ (or 0.40) corresponding to Fe_3Au_2 (or Fe_2Au_3).*

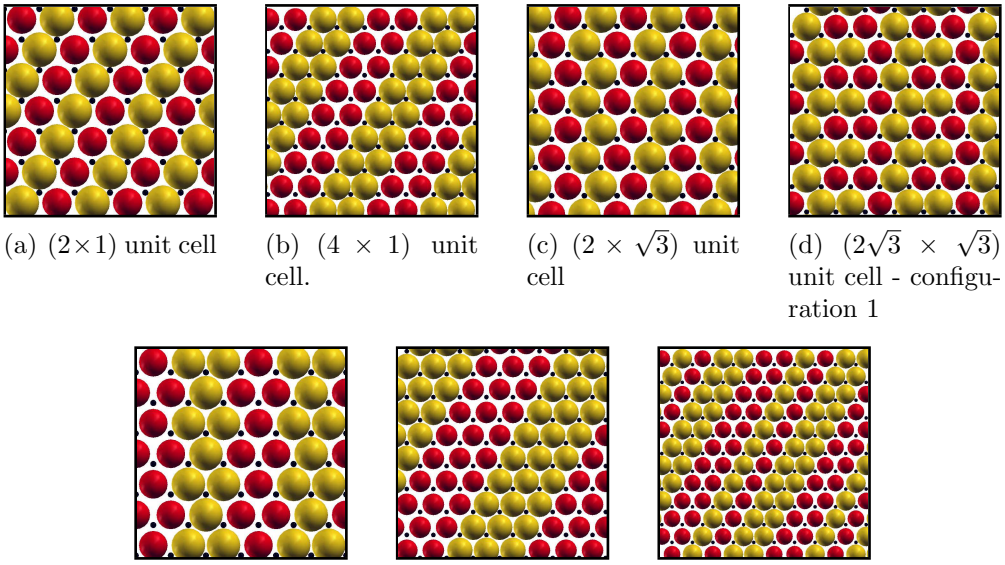

(a) (2×1) unit cell

(b) (4×1) unit cell.

(c) $(2 \times \sqrt{3})$ unit cell

(d) $(2\sqrt{3} \times \sqrt{3})$ unit cell - configuration 1

(e) $(2\sqrt{3} \times \sqrt{3})$ unit cell - configuration 2

(f) (6×1) unit cell - configuration 1

(g) (6×1) unit cell - configuration 2

Figure C.6: *Configurations for $x = 0.50$ corresponding to either $FeAu$ or Fe_2Au_2 or Fe_3Au_3.*

Appendix D

List of Configurations for $Fe_xAu_{(1-x)}$/Mo(110)

In this appendix, we have listed all the configurations used in the *ab initio* calculations in our study of $Fe_xAu_{(1-x)}$/Mo(110). For this study, we have considered all the distinct alloy configurations containing two, three, four, five and six atoms per unit cell, and also two configurations with seven atoms per unit cell. The total number of configurations is more than 100. The distinct unit cells containing n_a number of atoms can be found using the formula described in the Appendix B. For a centered-rectangular unit cell, the basis vectors (primitive lattice vectors for (1×1) cell) are given by $\bar{a}_1 = \alpha(\sqrt{2}, 1)a$ and $\bar{a}_2 = \alpha(-\sqrt{2}, 1)a$, where a is the NN spacing of the substrate and $\alpha = 1/\sqrt{3}$.

Here we have shown the schematic top views of all the configurations for Fe-rich systems, that is, $x \geq 0.50$, where x is the fractional composition of Fe. Fe atoms are shown with red (small) spheres and Au atoms with yellow (large) spheres. One can obtain corresponding Au-rich configurations just by exchanging red and yellow spheres. We have not shown the configurations for the cluster expansion calculations, as these number more than a million.

Number of atoms per unit cell	Corresponding number of distinct unit cells	Number of structures
2	2	2
3	3	6
4	5	14
5	4	24
6	7	56
7	1	2

Table D.1: *Summary of structures considered: For two, three, four, five and six atoms per unit cell, we have considered all the distinct alloy configurations possible. For seven atoms per unit cell, we have considered only two configurations as a test.*

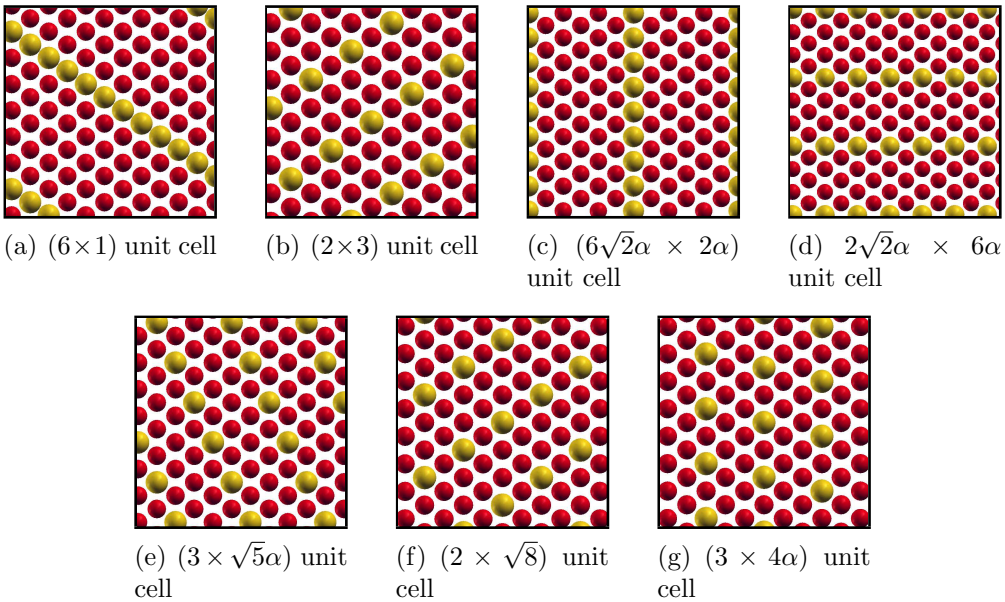

(a) (6×1) unit cell (b) (2×3) unit cell (c) $(6\sqrt{2}\alpha \times 2\alpha)$ unit cell (d) $2\sqrt{2}\alpha \times 6\alpha$ unit cell

(e) $(3\times\sqrt{5}\alpha)$ unit cell (f) $(2 \times \sqrt{8})$ unit cell (g) $(3 \times 4\alpha)$ unit cell

Figure D.1: *Configurations with composition $x = 0.833$ (or 0.167) corresponding to Fe_5Au (or $FeAu_5$).*

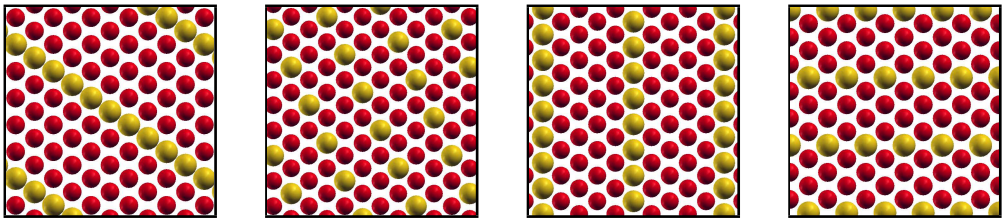

(a) (5×1) unit cell (b) $(\sqrt{8} \times \sqrt{5}\alpha)$ unit cell (c) $(\sqrt{17}\alpha \times 2\alpha)$ unit cell (d) $(2\sqrt{2}\alpha \times 3)$ unit cell

Figure D.2: *Configurations with composition $x = 0.80$ (or 0.20) corresponding to Fe_4Au (or $FeAu_4$).*

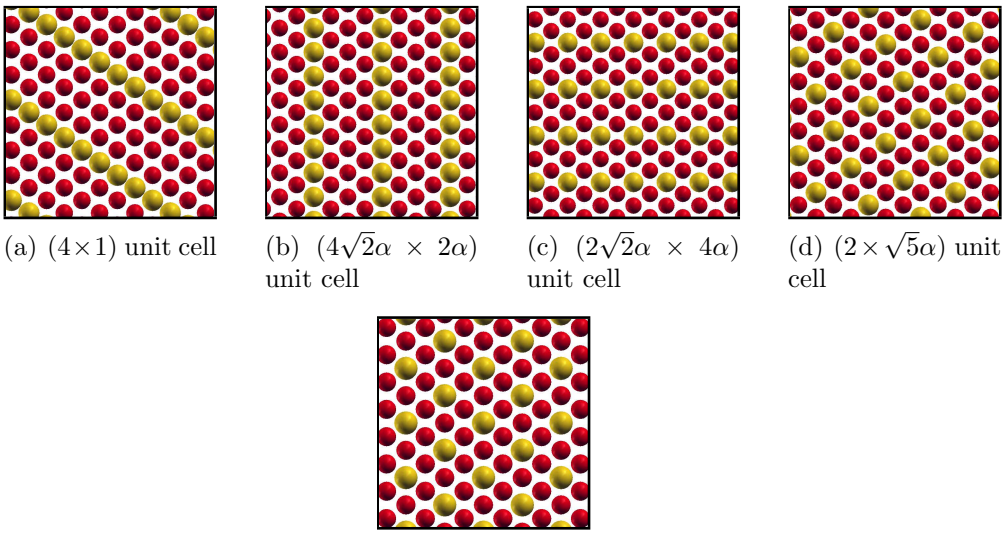

(a) (4×1) unit cell (b) $(4\sqrt{2}\alpha \times 2\alpha)$ unit cell (c) $(2\sqrt{2}\alpha \times 4\alpha)$ unit cell (d) $(2\times\sqrt{5}\alpha)$ unit cell

(e) (2×2) unit cell

Figure D.3: *Configurations with composition $x = 0.75$ (or 0.25) corresponding to Fe_3Au (or $FeAu_3$).*

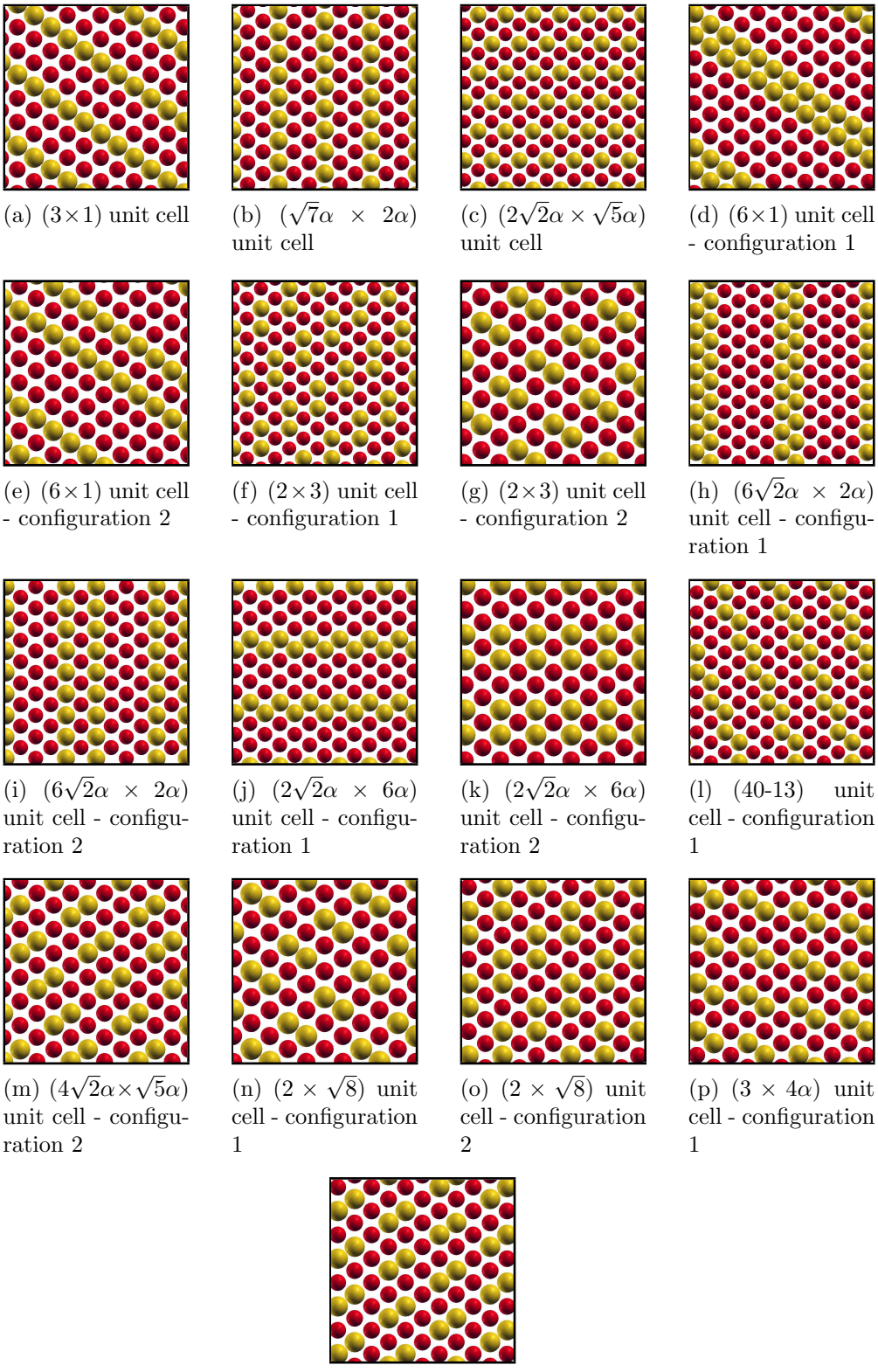

(a) (3×1) unit cell

(b) $(\sqrt{7}\alpha \times 2\alpha)$ unit cell

(c) $(2\sqrt{2}\alpha \times \sqrt{5}\alpha)$ unit cell

(d) (6×1) unit cell - configuration 1

(e) (6×1) unit cell - configuration 2

(f) (2×3) unit cell - configuration 1

(g) (2×3) unit cell - configuration 2

(h) $(6\sqrt{2}\alpha \times 2\alpha)$ unit cell - configuration 1

(i) $(6\sqrt{2}\alpha \times 2\alpha)$ unit cell - configuration 2

(j) $(2\sqrt{2}\alpha \times 6\alpha)$ unit cell - configuration 1

(k) $(2\sqrt{2}\alpha \times 6\alpha)$ unit cell - configuration 2

(l) (40-13) unit cell - configuration 1

(m) $(4\sqrt{2}\alpha\times\sqrt{5}\alpha)$ unit cell - configuration 2

(n) $(2 \times \sqrt{8})$ unit cell - configuration 1

(o) $(2 \times \sqrt{8})$ unit cell - configuration 2

(p) $(3 \times 4\alpha)$ unit cell - configuration 1

(q) Fe_4Au_2 in $(3\times 4\alpha)$ unit cell - configuration 2

Figure D.4: *Configurations with composition $x = 0.667$ (or 0.333) corresponding to either Fe_2Au (or $FeAu_2$) or Fe_4Au_2 (or Fe_2Au_4).*

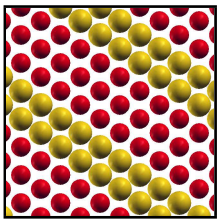

(a) (5×1) unit cell - configuration 1

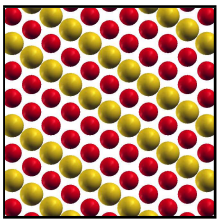

(b) (5×1) unit cell - configuration 2

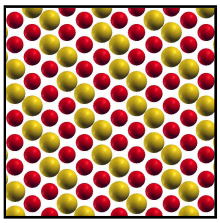

(c) $(\sqrt{7}\alpha \times \sqrt{5}\alpha)$ unit cell - configuration 1

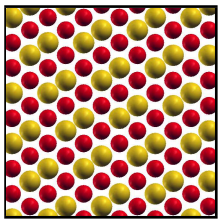

(d) $(\sqrt{7}\alpha \times \sqrt{5}\alpha)$ unit cell - configuration 2

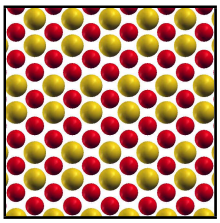

(e) $(2\sqrt{2}\alpha \times 3)$ unit cell - configuration 1

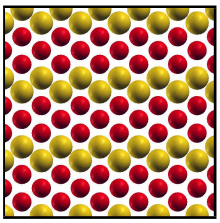

(f) $(2\sqrt{2}\alpha \times 3)$ unit cell - configuration 2

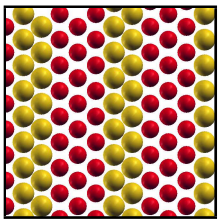

(g) $(\sqrt{17}\alpha \times 2\alpha)$ unit cell - configuration 1

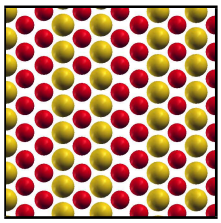

(h) $(\sqrt{17}\alpha \times 2\alpha)$ unit cell - configuration 2

Figure D.5: *Configurations with composition $x = 0.60$ (or 0.40) corresponding to Fe_3Au_2 (or Fe_2Au_3).*

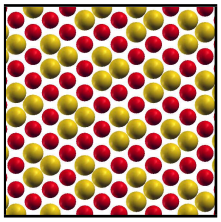

(a) $(\sqrt{7}\alpha \times 3)$ unit cell

Figure D.6: *Configuration with composition $x = 0.571$ (or 0.429) corresponding to Fe_4Au_3 (or Fe_3Au_4): This is the only configuration with seven atoms per unit cell.*

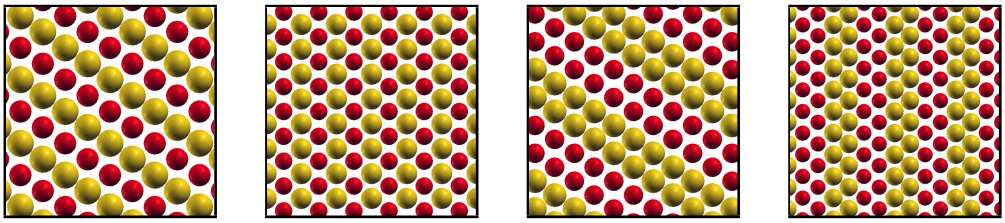

(a) (2×1) unit cell

(b) $(2\sqrt{2}\alpha \times 2\alpha)$ unit cell

(c) (4×1) unit cell

(d) $(4\sqrt{2}\alpha \times 2\alpha)$ unit cell

(e) $(2\sqrt{2}\alpha \times 4\alpha)$ unit cell

(f) $(2\times\sqrt{5}\alpha)$ unit cell

(g) (6×1) unit cell - configuration 1

(h) (6×1) unit cell - configuration 2

(i) (2×3) unit cell - configuration 1

(j) (2×3) unit cell - configuration 2

(k) $(6\sqrt{2}\alpha \times 2\alpha)$ unit cell - configuration 1

(l) $(6\sqrt{2}\alpha \times 2\alpha)$ unit cell - configuration 2

(m) $(2\sqrt{2}\alpha \times 6\alpha)$ unit cell - configuration 1

(n) $(2\sqrt{2}\alpha \times 6\alpha)$ unit cell - configuration 2

(o) $(4\sqrt{2}\alpha \times \sqrt{5}\alpha)$ unit cell - configuration 1

(p) $(4\sqrt{2}\alpha \times \sqrt{5}\alpha)$ unit cell - configuration 2

(q) Fe_3Au_3 in $(2\times\sqrt{8})$ unit cell - configuration 1

(r) Fe_3Au_3 in $(2\times\sqrt{8})$ unit cell - configuration 2

(s) Fe_3Au_3 in $(3\times4\alpha)$ unit cell - configuration 1

(t) Fe_3Au_3 in $(3\times4\alpha)$ unit cell - configuration 2

Figure D.7: *Configurations with composition $x = 0.50$ corresponding to either $FeAu$ or Fe_2Au_2 or Fe_3Au_3.*

Bibliography

[1] F. Besenbacher, I. Chorkendorff, B. S. Clausen, B. Hammer, A. M. Molenbroek, J. K. Nørskov and I. Stensgaard, Science **279**, 1913 (1998).

[2] M. L. Plummer, J. van Ek and D. Weller, The Physics of Ultra-High-Density Magnetic Recording (Springer, New York 2001).

[3] V. R. Stamenkovic, B. S. Mun, M. Arenz, K. J. J. Mayrhofer, C. A. Lucas, G. Wang, P. N. Ross and N. M. Markovic, Nat. Mater. **6**, 241 (2007).

[4] D. D. Chambliss, R. J. Wilson and S. Chiang, Phys. Rev. Lett. **66**, 1721 (1991).

[5] M. Böhringer, K. Morgenstern, W-D. Schneider, R. Berndt, F. Mauri, A. de Vita and R. Car, Phys. Rev. Lett. **83** 324 (1999).

[6] M. Born and J. R. Oppenheimer, Ann. Physik, **84**, 457 (1927).

[7] P. Hohenberg and W. Kohn, Phys. Rev. **136**, B864 (1964).

[8] R. M. Martin, *Electronic Structure Basic Theory and Practical Methods*, Cambridge University Press, Cambridge (2004).

[9] D. M. Ceperley and B. J. Alder, Phys. Rev. Lett. **45**, 566 (1980).

[10] J. P. Perdew and A. Zunger, Phys. Rev. B **23**, 5048 (1981).

[11] J. P. Perdew, K. Burke and M. Ernzerhof, Phys. Rev. Lett. **77**, 3865 (1996).

[12] J. P. Perdew and Y. Wang, Phys. Rev. B **45**, 13244 (1992).

[13] J. C. Phillips, Phys. Rev. **112**, 685 (1958).

[14] M. T. Yin and M. L. Cohen, Phys. Rev. B **25**, 7403 (1982).

[15] D. R. Hamann, M. Schlüter and C. Chiang, Phys. Rev. Lett. **43**, 1494 (1979).

[16] A. Zunger and M. L. Cohen, Phys. Rev. B **20**, 4082 (1979).

[17] G. B. Bachelet, D. R. Hamann and M. Schlüter, Phys. Rev. B **26**, 4199 (1982).

[18] D. Vanderbilt, Phys. Rev. B **41**, 7892 (1990).

[19] H. J. Monkhorst and J. D. Pack, Phys. Rev. B **13**, 5188 (1976).

[20] D. J. Chadi and M. L. Cohen, Phys. Rev. B **8**, 5747 (1973).

[21] C. L. Fu and K. M. Ho, Phys. Rev. B **28** 5480 (1983).

[22] M. Methfessel and A. T. Paxton, Phys. Rev. B **40**, 3616 (1989).

[23] N. Marzari, D. Vanderbilt, A. De Vita and M. C. Payne, Phys. Rev. Lett. **82**, 3296 (1999).

[24] R. P. Feynman, Phys. Rev. **56** 340 (1939).

[25] P. Pulay, Mol. Phys. **17**, 197 (1969).

[26] M. Scheffler, J. P. Vigneron and G. B. Bachelet, Phys. Rev. B **31**, 6541 (1985).

[27] O. H. Nielsen and R. Martin, Phys. Rev. Lett. **50**, 697 (1983).

[28] J. Tersoff and D. R. Hamann, Phys. Rev. B **31**, 805 (1985).

[29] P. Giannozzi, S. Baroni, N. Bonini, M. Calandra, R. Car, C. Cavazzoni, D. Ceresoli, G.L Chiarotti, M. Cococcioni, I.Dabo, A. Dal Corso, S. de Gironcoli, S. Fabris, G. Fratesi, R. Gebauer, U. Gerstmann, C. Gougoussis, A. Kokalj, M. Lazzeri, L. Martin-Samos, N. Marzari, F. Mauri, R. Mazzarello, S. Paolini, A. Pasquarello, L. Paulatto, C. Sbraccia, S. Scandolo, G. Sclauzero, A. P Seitsonen, A. Smogunov, P. Umari and R. M Wentzcovitch, J. Phys. Condens. Matter **21**, 395502 (2009).

[30] F. Cleri and V. Rosato, Phys. Rev. B **48**, 22 (1993).

[31] A. Diaz-Ortiz, F. Aguilera-Granja, K. Michaelian, E. O. Berlanga-Ramírez, J. M. Montejano-Carrizales and A. Vega, Physica B, **370**, 200 (2005).

[32] S. M. Foiles, Phys. Rev. B **32**, 7685 (1985).

[33] P. C. Kelires and J. Tersoff, Phys. Rev. Lett. **63**, 1164 (1989).

[34] J. M. Sanchez, F. Ducastelle and D. Gratias, Physica **128A**, 334 (1984).

[35] J. M. Sanchez, Phys. Rev. B **48**, 14013 (1993).

[36] N. Metropolis, A. W. Rosenbluth, M. N. Rosenbluth, A. H. Teller and E. Teller, J. Chem. Phys. **21**, 1087 (1953).

[37] A. Zunger, in *Statics and Dynamics of Alloy Phase Transformations*, edited by P. E. A. Turchi and A. Gonis (Plenum, New York, 1994), p. 361.

[38] S.-H. Wei, L. G. Ferreira and A. Zunger, Phys. Rev. B **41**, 8240 (1990).

[39] Z. W. Lu, S.-H. Wei, A. Zunger, S. Frota-Pessoa and L. G. Ferreira, Phys. Rev. B **44**, 512 (1991).

[40] R. Magri and A. Zunger, Phys. Rev. B **44**, 8672 (1991).

[41] E. A. Albanesi, W. R. L. Lambrecht and B. Segall, Phys. Rev. B **48**, 17841 (1993).

[42] A. Diaz-Ortiz and H. Dosch, Phys. Rev. B **76**, 012202 (2007).

[43] A. Diaz-Ortiz, H. Dosch and R. Drautz, J. Phys.: Condens. Matter **19**, 406206 (2007).

[44] B. Arnold, A. Diaz-Ortiz, G. L. W. Hart and H. Dosch, Phys. Rev. B **81**, 094116 (2010).

[45] R. Kikuchi, J. M. Sanchez, D. de Fontaine and H. Yamauchi, Acta Metall. **28**, 651 (1980).

[46] C. Sigli and J. M. Sanchez, Acta Metall. **33** 1097 (1985).

[47] J. W. D. Connolly and A. R. Williams, Phys. Rev. B **27**, 5169 (1983).

[48] G. D. Garbulsky and G. Ceder, Phys. Rev. B **51**, 67 (1995).

[49] C. Wolverton and A. Zunger, Phys. Rev. Lett. **75**, 3162 (1995).

[50] A. van der Walle and G. Ceder, J. Phase Equilib. **23**, 348 (2002).

[51] R. Drautz and A. Diaz-Ortiz, Phys. Rev. B **73**, 224207 (2006).

[52] A. Diaz-Ortiz, R. Drautz, M. Fähnle, H. Dosch and J. M. Sanchez, Phys. Rev. B **73**, 224208 (2006).

[53] M. Stone, J. R. Stat. Soc. B Met. **36**, 111 (1974).

[54] W. Hume-Rothery and H. M. Powell, *Z. Krist* **91**, 13 (1935).

[55] F. Heusler, *Verhandl. Deut. Physik. Ges.*, **5**, 219 (1903).

[56] U. Bardi, Rep. Prog. Phys. **57**, 939 (1994).

[57] A. T. Hubbard, *The handbook of surface imaging and visualization* (CRC press, 1995).

[58] E. C. Stoner, Proc. R. Soc. London, Ser. A **169**, 339 (1939).

[59] S. E. Apsel, J. W. Emmert, J. Dung and L. A. Bloomfield, Phys. Rev. Lett. **76**, 1441 (1996).

[60] I. M. L. Billas, A. Châtelain and Walt A. de Heer, Science **265**, 1682 (1994).

[61] F. A. Reuse and S. N. Khanna, Chem. Phys. Lett. **234**, 77 (1995).

[62] V. L. Moruzzi and P. M. Marcus, Phys. Rev. B **39**, 471 (1989).

[63] B. V. Reddy, S. N. Khanna and B. I. Dunlap, Phys. Rev. Lett. **70**, 3323 (1993).

[64] A. J. Cox, J. G. Louderback and L. A. Bloomfield, Phys. Rev. Lett. **71**, 923 (1993).

[65] K. Wildberger, V. S. Stepanyuk, P. Lang, R. Zeller and P. H. Dederichs, Phys. Rev. Lett. **75**, 509 (1995).

[66] B. Piveteau, Desjonquères, A. M. Oleś and D. Spanjaard, Phys. Rev. B **53**, 9251 (1996).

[67] R. Guirado López, D. Spanjaard and M. C. Desjonquères, Phys. Rev. B **57**, 6305 (1998).

[68] V. L. Moruzzi, J. F. Janak and A. R. Williams, Calculated electronic properties of metals, Pergamon, New York (1978).

[69] N. Watari and S. Ohnishi, Phys. Rev. B **58**, 1665 (1998).

[70] X. Liu, H. Dilger, R. A. Eichel, J. Kunstmann and E. Roduner, J. Phys. Chem. B **110**, 2013 (2006).

[71] X. Liu, M. Bauer, H. Bertagnolli, E. Roduner, J. van Slageren and F. Philipp, Phys. Rev. Lett. **97**, 253401 (2006).

[72] P. T. Wouda, M. Schmid, B. E. Nieuwenhuys and P. Verga, Surf. Sci. **417**, 292 (1998).

[73] A. V. Ruban, S. I. Simak, P. A. Korzhavyi and B. Johansson, Phys. Rev. B **75**, 054113 (2007).

[74] J. Tersoff, Phys. Rev. Lett. **74**, 434 (1995).

[75] H. Röder, R. Schuster, H. Brune and K. Kern, Phys. Rev. Lett. **71**, 2086 (1993).

[76] A. Zangwill, *Physics at surfaces*, Cambridge University Press, Cambridge (1988).

[77] L. P. Nielsen, F. Besenbacher, I. Stensgaard, E. Lægsgaard, C. Engdahl, P. Stoltze, K. W. Jacobsen and J. K. Nørskov, Phys. Rev. Lett. **71**, 754 (1993).

[78] J. L. Stevens and R. Q. Hwang, Phys. Rev. Lett. **74**, 2078 (1995).

[79] M. Schick, J. Schäffer, K. Kalki, G. Ceballos, P. Reinhardt, H. Hoffschulz and K. Wandelt, Surf. Sci. **287/288**, 960 (1993).

[80] M. Schick, G. Ceballos, Th. Peizer, J. Schäffer, G. Rangelov, J. Stober and K. Wandelt, J. Vac. Sci. Technol. A **12**, 1795 (1994).

[81] B. Sadigh, M.Asta, V. Ozoliņš, A. K. Schmid, N. C. Bartelt, A. A. Quong and R. Q. Hwang, Phys. Rev. Lett **83**, 1379 (1999).

[82] J. Yuhara, M. Schmid and P. Verga, Phys. Rev. B **67**, 195407 (2003).

[83] E. D. Tober, R. C. F. Farrow, R. F. Marks, G. Witte, K. Kalki and D. D. Chambliss, Phys. Rev. Lett. **81**, 1897 (1998).

[84] B. Yang, T. Muppidi, V. Ozoliņš, M. Asta, Phys. Rev. B **77**, 205408 (2008).

[85] P. W. Palmberg and T. N. Rhodin, J. Chem. Phys. **49**, 134 (1968).

[86] J. G. Tobin, S. W. Robey and D. A. Shirley, Phys. Rev. B **33**, 2270 (1986).

[87] J. G. Tobin, S. W. Robey, L. E. Klebanoff and D. A. Shirley, Phys. Rev. B **35**, 9056 (1987).

[88] J. E. Black, D. L. Mills, W. Daum, C. Stuhlmann and H. Ibach, Surf. Sci. **217**, 529 (1989).

[89] C. Mottet, G. Treglia and B. Legrand, Phys. Rev. B **46**, 16018 (1992).

[90] P. T. Sprunger, E. Lægsgaard and F. Besenbacher, Phys. Rev. B **54**, 8163 (1996).

[91] R. Q. Hwang, Phys. Rev. Lett. **76**, 4757 (1996).

[92] G. E. Thayer, V. Ozoliņš, A. K. Schmid, N. C. Bartelt, M. Asta, J. J. Hoyt, S. Chiang and R. Q. Hwang, Phys. Rev. Lett. **86**, 660 (2001).

[93] V. Ozoliņš, M. Asta and J. J. Hoyt, Phys. Rev. Lett. **88**, 096101 (2002).

[94] G. E. Thayer, N. C. Bartelt, V. Ozoliņš, A. K. Schmid, S. Chiang and R. Q. Hwang, Phys. Rev. Lett. **89**, 036101 (2002).

[95] J. Hunter Dunn, D. Arvanities and N. Martensson, Phys. Rev. B **54**, R11 157 (1996).

[96] J. Henk, A. M. N. Niklasson and B. Johansson, Phys. Rev. B **59**, 9332 (1999).

[97] S. Dennler, J. Hafner, M. Marsman and J. Morillo, Phys. Rev. B **71**, 094433 (2005).

[98] S. Blügel, Apply. Phys. A **63**, 595 (1996).

[99] W. Daum, C. Stuhalmann and H. Ibach, Phys. Rev. Lett. **60**, 2741 (1988).

[100] B. T. Jonker, J. J.Krebs and G. A. Prinz, Phys. Rev. B **39**, 1399 (1989).

[101] M. Wuttig, Y. Gauthier and S. Blügel, Phys. Rev. Lett. **70**, 3619 (1993).

[102] G. Bihlmayer, Ph. Kurz and S. Blügel, Phys. Rev. B **62**, 4726 (2000).

[103] N. W. Ashcroft and N. D. Mermin, *Solid State Physics* (Thomson Asia Pte. Ltd. Bangalore 2004).

[104] J. Kolaczkiewicz and E. Bauer, Surf. Sci. **423**, 292 (1999).

[105] F. el Gabaly, J. M. Puerta, C. Klein, A. Saa, A. K. Schmid, K. F. McCarty, J. I. Cerda and J. de la Figuera, New J. Phys. **9**, 80 (2007).

[106] U. Käsberger and P. Jakob, Surf. Sci. **540**, 76 (2003).

[107] W. L. Ling, J. C. Hamilton, K. Thürmer, G. E. Thayer, J. de la Figuera, R. Q. Hwang, C. B. Carter, N. C. Bartelt and K. F. McCarty, Surf. Sci **600**, 1735 (2006).

[108] R. Q. Hwang, J. C. Hamilton, J. L. Stevens and S. M. Foiles, Phys. Rev. Lett **75**, 4242 (1995).

[109] C. Kittel, *Introduction of Solid State Physics* Seventh Ed. (John Wiley & Sons (ASIA) Pvt. Ltd. 1996).

[110] J. R. Chelikowsky, C. T. Chan and S. G. Louie, Phys. Rev. B **34**, 6656 (1986).

[111] E. G. Moroni, G. Kresse, J. Hafner and J. Furthmüller, Phys. Rev. B **56**, 15629 (1997).

[112] S. Narasimhan and M. Scheffler, Z. Phys. Chem. (Munich) **202**, 253 (1997).

[113] J. Xie, S. de Gironcoli, S. Baroni and M. Scheffler, Phys. Rev. B **59**, 965 (1999).

[114] D. Yu and M. Scheffler, Phys. Rev. B **70**, 155417 (2004).

[115] C. Bercegeay and S. Bernard, Phys. Rev. B **72**, 214101 (2005).

[116] M. Y. Chou and R. Chelikowsky, Phys. Rev. B **35**, 2124 (1987).

[117] L. Vitos, A. V. Ruban, H.L. Skriver and J. Kollar, Surf. Sci. **411**, 186 (1998).

[118] Noriko Watari and Shihei Ohnishi, Phys. Rev. B **58**, 1665 (1998).

[119] M. A. Ruderman and C. Kittel, Phys. Rev. **96**, 99 (1954).

[120] B. Hardrat, A. Al-Zubi, P. Ferriani, S. Blügel, G. Bihlmayer and S. Heinze, Phys. Rev. B **79**, 094411 (2009).

[121] A. R. Williams, R. Zeller, V. L. Moruzzi, C. D. Gelatt Jr. and J. Kubler, J. Appl. Phys. **52**, 2067 (1981).

[122] R. Pushpa, P. Ghosh, S. Narasimhan and S. de Gironcoli, Phys. Rev. B **79**, 165406 (2009).

[123] M. S. Daw and M. I. Baskes, Phys. Rev. Lett.**50**, 1285 (1983).

[124] M. S. Daw, Phys. Rev. B **39**, 7441 (1989).

[125] H. Ibach, Surf. Sci, Rep. **29**, 193 (1997).

[126] R. Pushpa and S. Narasimhan, Phys. Rev. B **67**, 205418 (2003).

[127] N. Takeuchi, C. T. Chan and K. M. Ho, Phys. Rev. B **43**, 13899 (1991).

[128] J. C. Hamilton and S. M. Foiles, Phys. Rev. Lett. **75** 882 (1995).

[129] J. C. Hamilton, R. Stumpf, K. Bromann, M. Giovannini, K. Kern and H. Brune, Phys. Rev. Lett. **82**, 4488 (1999).

[130] M. P. Allen and D. J. Tildesley, *Computer Simulations of liquids* (Oxford Science Publications, New York, 1987).

[131] R. Q. Hwang, C. Günther, J. Schröder, S. Günther, E. Kopatzki and R. J. Behm, J. Vac. Sci. Technol. A **10**, 1970 (1992).

[132] M. Marathe, M. Imam and S. Narasimhan, Appl. Surf. Sci. **256**, 449 (2009).

[133] M. Imam and S. Narasimhan, J. Magn. Magn. Mater. **323**, 1873 (2011).

[134] M. Marathe, M. Imam and S. Narasimhan, Phys. Rev. B **79**, 085413 (2009).

[135] *Binary Alloy Phase Diagrams, vol. 1* edited by T. B. Massalski (ASM international, Ohio, 1998).

[136] M. M. J. Bischoff, T. Yamada, A. J. Quinn, R. G. P. ven der Kraan and H. van Kempen, Phys. Rev. Lett. **87**, 246102 (2001).

[137] M. M. J. Bischoff, T. K. Yamada and H. van Kempen, Phys. Rev. B **67**, 165403 (2003).

[138] S. Andrieu, M. Piecuch and J. F. Bobo, Phys. Rev. B **46**, 4909 (1992).

[139] J. C. Jamieson and A. W. Lawson, J. Appl. Phys. **33**, 776 (1962).

[140] D. N. Pipkorn, C. K. Edge, P. Debrunner, G. de Pasquali, H. G. Drickamer and H. Frauenfelder, Phys. Rev. **135**, A1604 (1964).

[141] G. C. Fletcher and R. P. Addis, J. Phys. F **4**, 1951 (1974).

[142] G. Cort, R. D. Taylor and J. O. Willis, J. Appl. Phys. **53**, 2064 (1982).

[143] C. Liu and S. D. Bader, Phys. Rev. B **41**, 553 (1990).

[144] R. Wu and A. J. Freeman, Phys. Rev. B **44**, 4449 (1991).

[145] S. Mehendale, Ph. D. thesis, *Universite Paris-Diderot (Paris 7)*, France (2010).

[146] S. Mehendale, Y. Girard, V. Repain, C. Chacon, J. Lagoute, S. Rousset, M. Marathe and S. Narasimhan, Phys. Rev. Lett. **105**, 056101 (2010).

[147] S. Mehendale, M. Marathe, Y. Girard, V. Repain, C. Chacon, J. Lagoute, S. Rousset and S. Narasimhan, Phys. Rev. B **84**, 195458 (2011).

[148] J.-P. Serre, *Cours d'Arithmetique*, Presses Universitaires de France, Paris, (1970).

[149] L. M. de la Garza and L. J. Clarke, J. Phys. C: Solid State Phys. **14**, 5391 (1981).

[150] B. Gruzza and E. Gillet, Thin Solid Films, **68**, 345 (1980).

[151] A. Pavlovska, M. Paunov and E. Bauer, Thin Solid Films, **126**, 129 (1985).

[152] E. Gillet and B. Gruzza, Surf. Sci. **97**, 553 (1980).

[153] M. Tikhov and E. Bauer, Surf. Sci. **232**, 73 (1990).

[154] J. Malzbender M. Przybylski, J. Giergiel and J. Kirschner, Surf Sci. **414**, 187 (1998).

[155] S. Murphy, D. Mac Mathúna, G. Mariotto and I. V. Shvets, Phys. Rev. B **66**, 195417 (2002).

[156] X. Qian, F. Wagner, M. Petersen and W. Hübner, J. Magn. Magn. Mater. **213**, 12 (2000).

[157] X. Qian and W. Hübner, Phys. Rev. B **64**, 092402 (2001).

[158] V. Usov, J. Murphy and I. V. Shvets, J. Magn. Magn. Mater. **283**, 357 (2004).

[159] M. Bode, O. Pietzsch, A. Kubetzka and R. Wiesendanger, Phys. Rev. Lett. **92**, 067201 (2004).

[160] J. Prokop, A. Kukunin and H. J. Elmers, Phys. Rev. Lett. **95**, 187202 (2005).

[161] J. Prokop, A. Kukunin and H. J. Elmers, Phys. Rev. B **73**, 014428 (2006).

[162] A. Kukunin, J. Prokop and H. J. Elmers, Acta Phys. Pol. A **109**, 371 (2006).

[163] J. Prokop, A. Kukunin and H. J. Elmers, Phys. Rev. B **75**, 144423 (2007).

[164] W. R. Tyson and W. A. Miller, Surf. Sci. **62**, 267 (1977).

[165] M. Methfessel, D. Hennig and M. Scheffler, Phys. Rev. B **46**, 4816 (1992).

[166] J. H. van der Merwe, E. Bauer, D. L. Tönsing and P. M. Stoop, Phys. Rev. B **49**, 2137 (1994).

[167] J. G. Che, T. G. Chan, W-E. Jian and T. C. Leung, Phys. Rev. B **57**, 1875 (1998).

[168] G. L. W. Hart and R. W. Forcade, Phys. Rev. B **77**, 224115 (2008).

[169] W. Haiss, Rep. Prog. Phys. **64**, 591 (2001).

[170] J. V. Barth, H. Brune, G. Ertl and R. J. Behm, Phys. Rev. B **42**, 9307 (1990).

[171] A. R. Sandy, S. G. J. Mochrie, D. M. Zehner, K. G. Huang and D. Gibbs, Phys. Rev. B **43**, 4667 (1991).

[172] S. Narasimhan and D. Vanderbilt, Phys. Rev. Lett. **69**, 1564 (1992).

[173] C. Günther, J. Vrijmoeth, R. Q. Hwang and R. J. Behm, Phys. Rev. Lett. **74**, 754 (1995).

[174] J. Frenkel and T. Kontorova, Z. Sowjetunion **13**, 1 (1938).

[175] M. Mansfield and R. J. Needs, J. Phys. Condens. Matter **2**, 2361 (1990).

[176] S. C. Erwin, A. A. Baski, L. J. Whitman and R. E. Rudd, Phys. Rev. Lett. **83**, 1818 (1999).

[177] J. C. Hamilton, Phys. Rev. Lett. **88**, 126101 (2002).

[178] Ž. Crljen, P. Lazić, D. Šokčević and R. Brako, Phys. Rev. B **68**, 195411, (2003).

[179] R. Pushpa, J, Rodriguez-Laguna and S. N. Santalla, Phys. Rev. B **79**, 85409 (2009).

[180] K. Thürmer, C. B. Carter, N. C. Bartelt and R. Q. Hwang, Phys. Rev. Lett. **92**, 106101 (2004).

[181] I. Daruka and J. C. Hamilton, J. Phys.: Condens. Matter **15**, 1827 (2003).

[182] A.R. Sandy, S. G. J. Mochrie, D. M. Zehner, G. Grübel, K. G. Huang and D. Gibbs, Phys. Rev. Lett. **68**, 2192 (1992).

[183] M. Bott, M. Hohage, T. Michely and G. Comsa, Phys. Rev. Lett. **70**, 1489 (1993).

[184] C. H. Park and D. J. Chadi, Phys. Rev. B **49**, 16467 (1994).

[185] L. Zhu, K. L. Yao, Z. L. Liu and Y. B. Li, J. Phys.: Condens. Matter **21**, 095001 (2009).

[186] E. Kaxiras, K. C. Pandey, Y. Bar-Yam and J. D. Joannopoulos, Phys. Rev. Lett. **56**, 2819 (1986).

[187] K. Menda, I. Takayasu, T. Minato and M. Kawashima, Jap. J. Appl. Phys. **26**, L1326 (1987).

[188] X. Gao, A. Hamelin and M. J. Weaver, Phys. Rev. B **46**, 7096 (1992).

[189] D. M. Kolb, Prog. Surf. Sci **51**, 109 (1996).

[190] O. Sakata and M. Nakamura, Appl. Surf. Sci. **256**, 1144 (2009).

[191] G. Liu, K. A. Davis, D. C. Meier, P. S. Bagus, D. W. Goodman, and G. W. Zajac, Phys. Rev. B **68**, 035406 (2003).

[192] W. Shockley, Phys. Rev. **56**, 317 (1939).

[193] I. Tamm, Phys. Z. Soviet Union **1**, 733 (1932).

[194] N. Memmel, Surf. Sci. Rep. **32**, 91 (1998).

[195] S. D. Kevan and R. H. Gaylord, Phys. Rev. B **36**, 5809 (1987).

[196] G. Nicolay, F. Reinert, S. Hüfner and P. Blaha, Phys. Rev. B **65** 033407 (2001).

[197] D. Malterre, B. Kierren, Y. Fagot-Revurat, S. Pons, A. Tejeda, C. Didiot, H. Cercellier and A. Bendounan, New J. Phys. **9**, 391 (2007).

[198] F. Forster, G. Nicolay, F. Reinert, D. Ehm, S. Schmidt and S. Hüfner, Surf. Sci. **532**, 160 (2003).

[199] T. Andreev, I. Barke and H. Hövel, Phys. Rev. B **70**, 205426 (2004).

[200] M. F. Crommie, C. P. Lutz and D. M. Eigler, Nature **363**, 524 (1993).

[201] J. Li, W. Schneider, R. Berndt and S. Crampin, Phys. Rev. Lett. **80**, 3332 (1998).

[202] L. Bürgi, O. Jeandupeux, A. Herstein, H. Brune and K. Kern, Phys. Rev. Lett. **81**, 5370 (1998).

[203] F. E. Olsson, M. Persson, A. G. Borisov, J. P. Gauyacq, J. Lagoute and S. Fölsch, Phys. Rev. Lett. **93**, 206803 (2004).

[204] L. Niebergall, G. Rodary, H. F. Ding, D. Sander, V. S. Stepanyuk, P. Bruno and J. Kirschner, Phys. Rev. B **74**, 195436 (2006).

[205] K. H. Lau and W. Kohn, Surf. Sci. **75**, 69 (1978).

[206] E. Wahlström, I. Ekvall, H. Olin and L. Walldén, Appl. Phys. **A66**, S1107 (1998).

[207] J. Repp, F. Moresco, G. Meyer, K. Rieder, P. Hyldgaard and M. Persson, Phys. Rev. Lett. **85**, 2981 (2000).

[208] V. S. Stepanyuk, A. N. Baranov, D. V. Tsivlin, W. Hergert, P. Bruno, N. Knorr, M. A. Schneider and K. Kern, Phys. Rev. B **68**, 205410 (2003).

[209] F. Silly, M. Pivetta, M. Ternes, F. Patthey, J. P. Pelz and W. Schneider, Phys. Rev. Lett. **92**, 16101 (2004).

[210] H. F. Ding, V. S. Stepanyuk, P. A. Ignatiev, N. N. Negulyaev, L. Niebergall, M. Wasniowska, C. L. Gao, P. Bruno and J. Kirschner, Phys. Rev. B **76**, 33409 (2007).

[211] S. Lukas, G. Witte and Ch. Wöll, Phys. Rev. Lett. **88**, 028301 (2002).

[212] L. Diekhöner, M. A. Schneider, A. N. Baranov, V. S. Stepanyuk, P. Bruno and K. Kern, Phys. Rev. Lett. **90**, 266801 (2003).

[213] L. Niebergall, V. S. Stepanyuk, J, Berakdar and P. Bruno, Phys. Rev. Lett. **96**, 127204 (2006).

[214] H. Oka, P. A. Ignatiev, S. Wedekind, G. Rodary, L. Niebergall, V. S. Stepanyuk, D. Sander and J. Kirschner, Science **327**, 843 (2010).

[215] M. V. Rastei, J. P. Bucher, P. A. Ignatiev, V. S. Stepanyuk and P. Bruno, Phys. Rev. B **75**, 045436 (2007).

[216] K. Schouteden, E. Lijnen, E. Janssens, A. Ceulemans, L. F. Chibotaru, P. Lievens and C. van Haesendonck, New J. Phys. **10**, 043016 (2008).

[217] A. Delga, J. Lagoute, V. Repain, C. Chacon, Y. Girard, M. Marathe, S. Narasimhan and S. Rousset, Phys. Rev. B **84**, 35416 (2011).

[218] F. Donati, G. Fratesi, M. Passoni, C. S. Casari, A. Mairov, C. E. Bottani, M. I. Trioni and A. Li Bassi, Phys. Rev. B **83**, 153404 (2011).

[219] J. A. Stroscio, D. T. Pierce, R. A. Dragoset and P. N. First, J. Vac. Sci. Technol. A **10**, 1981 (1992).

[220] H. Bulou, F. Scheurer, P. Ohresser, A. Berbier, S. Stanescu and C. Quirós, Phys. Rev. B **69**, 155413 (2004).

[221] P. Ohresser, N. B. Brookes, S. Padovani, F. Scheurer and H. Bulou, Phys. Rev. B **64**, 104429 (2001).

[222] W.Chen, V. Madhavan, T. Jamneala and M. F. Crommie, Phys. Rev. Lett. **80**, 1469 (1998).

[223] J. Henk, M. Hoesch, J. Osterwalder, A. Ernst and P. Bruno, J. Phys.: Condens. Matter **16**, 7581 (2004).

[224] M. Marathe, J. Lagoute, V. Repain, S. Rousset and S. Narasimhan, Surf. Sci. **606**, 950 (2012).

[225] B. Hammer and J. K. Nørskov, Surf. Sci. **343**, 211 (1995).